Final Report

Metal Foams for impact mitigation of railroad tank-cars

Pipeline and Hazardous Materials Safety Administration (PHMSA) project number
DTPH5616C00001

Date: May 10th, 2020

Prepared by:
Professor Afsaneh Rabiei, Mechanical and Aerospace Engineering (MAE), North Carolina State University (NCSU)

Table of Contents

Section **Page**

List of Figures

Figure **Page**

List of Tables

Table **Page**

1 Executive Summary

This report is focused on evaluating steel-steel composite metal foams (SS-CMF) in simulated pool fire and torch fire testing conditions along with SS-CMF core sandwich panels (SS-CMF-CSP) in quasi static and puncture testing conditions. An overview of the manufacturing of SS-CMF panels as well as their bonding to solid steel face sheets to create sandwich panels is presented first, followed by their properties against quasi-static loading. These analyses were restricted to relatively small-scale laboratory experiments. Full-scale simulations of tank-car punctures are needed before SS-CMF can be introduced to the structure of the next generation tank-cars with puncture and fire resistance. This report includes some of the unpublished work that is currently pending publication.

The mechanical properties of SS-CMF and SS-CMF-CSP were explored through quasi-static tension and compression testing. The base SS-CMF samples had an ultimate tensile strength of 75-85 MPa and a failure strain of 7.5-8%. The normalized tensile strength was approximately 24 MPa/(g/cm^3), more than five times that of any comparable metal foams. The specific energy absorption of SS-CMF is almost an order of magnitude higher than that of other metal foams indicating that one gram of SS-CMF absorbs ten times more energy compared to that of other metal foams. The ultimate tensile strength of the SS-CMF-CSP was more than twice that of the base SS-CMF at 165 MPa with an average failure strain of 23%. The normalized strength of the SS-CMF-CSP was 52% higher than the base SS-CMF. The face sheets effectively supported the SS-CMF core under tension while maintaining relatively stable adhesion along the bond line. The compressive strength of the SS-CMF core sandwich panels was the same as that of the SS-CMF core with only a slight increase in the plateau strength after 30% strain due to the heating cycle of the diffusion bonding process. The face sheets on the SS-CMF-CSP not only improves the performance of the SS-CMF core under tension, but also provides a non-porous surface that can protect against corrosion and can be used in a variety of engineering applications.

Two sets of puncture tests were conducted on steel-steel composite metal foam core sandwich panels with two different thicknesses of stainless steel face sheets. The bonding of the SS-CMF core and face sheets was through adhesive bonding and diffusion bonding. Panels assembled using adhesive bonding were showing debonding of the face sheets from the core upon the impact of the projectile at lower velocities. A close observation of the bonding area after each puncture test indicated that the epoxy adhesive bonding with a stiffer bonding layer did not accommodate the shear and normal stresses upon impact, resulting in debonding of the face sheets from the SS-CMF core at lower impact velocities. The diffusion bonded panels with a cohesive bonding interface showed more flexibility at the interface and better accommodated the stresses, particularly at lower impact energies. Most diffusion bonded panels did not show debonding of face sheets from the SS-CMF core, except for those tested at higher impact energies, indicating that the diffusion bonding can be the preferred process of assembling SS-CMF core sandwich panels. However, additional studies are needed to optimize the

bonding strength between SS-CMF core and face sheets. Various thicknesses of the CMF core and face sheets created a variety of target areal densities from about 6.7 to 11.7 Kg per each tile of 30x30 cm. Targets were impacted using 2.54 and 3.175 cm diameter steel balls fired at velocities ranging from 120 to 470 meters per second, resulting in puncture energies from 488 to 14,500 joules. However, none of the panels, even those with the lowest areal densities, showed complete penetration/puncture through their thickness. This was mostly due to the energy absorption capacity of the SS-CMF core in compression, while the face sheets strengthened the CMF core to better handle tensile stresses. Sandwich panels with thicker face sheets showed less effectiveness and a thin face sheet seemed to be sufficient to support the SS-CMF core for absorbing such puncture energies. Even though this study shows extraordinary puncture resistance of SS-CMF core sandwich panels, a full-scale puncture test is required to evaluate the survivability of SS-CMF and SS-CMF core sandwich panels for application in tank-car-head and tank-car-side puncture-resistance systems.

A scaled down version of the simulated torch fire experiments and a full-scale simulated pool fire testing specified in 49 CFR Part 179, Appendix B was conducted on 15.9 mm (5/8") SS-CMF in order to evaluate the thermal protection and fire resistance of the material. Based on the experimental and modeling results, as well as the uncertainty studies, the 5/8" thick steel-steel composite metal foam panels tested as novel insulation system met the acceptance criteria for both the simulated pool fire and the scaled down torch fire tests specified in 49 CFR 179 Appendix B by a large margin and are expected to pass with near certainty if the test were to be reproduced in a different laboratory. Furthermore, the successful performance of SS-CMF in the simulated pool fire test (described in 49 CFR Part 179) and torch fire tests can be attributed to the presence of air bubbles inside, along with its low surface emissivity. To complete the full test requirements of CFR Part 179 App. B, the material will need to be tested in a full-scale torch-fire exposure condition in duplicate.

As such, a full-scale torch fire test along with a full-scale puncture test can bring composite metal foams and its sandwich panels closer to their application in the structure of next generation tank-cars with improved safety and more efficiency.

2 Introduction

According to the US Department of Transportation (USDOT), railroads are the safest means to transport hazardous materials (HAZMAT) (1). Although the number of rail HAZMAT accidents has dropped by 66% since 2000, major accidents continue to occur (1). Some of these accidents result in a large number of casualties, for example, on July 6, 2013, a runaway train travelling at 104 km/h and carrying 7.7 million liters of petroleum crude oil burst into flames after crashing into the town of Lac-Mégantic, Quebec, Canada (2). The crude oil that spilled from the damaged rail cars caused multiple fires and explosions that destroyed most of the downtown area and caused 47 fatalities (2).

The Lac-Mégantic accident led to the development of the Department of Transportation (DOT)-117 tank-car (3). In May 2015, the DOT established the “DOT-117” specifications, which set stronger regulations on tank-cars carrying HAZMAT—such as crude oil (1, 4). The new standards are known as DOT-117 specifications. The DOT 117R set standards for the thermal protection system of tank-cars (5). According to these specifications, the tank-car must have sufficient thermal resistance so that there will be no release of any lading within the tank-car, except release through the pressure release device, when subjected to a pool fire for 100 minutes, and a torch fire for 30 minutes (6). Furthermore, a non-jacketed tank-car must have a thermal protection blanket with at least ½ inch thick, and the entire thermal protection system must be covered with a metal jacket of a thickness no less than 11 gauge A1011 steel or equivalent and flashed around all openings so as to be weather tight (3). The exterior surface of a carbon steel tank and the inside surface of a carbon steel jacket must be given a protective coating as well

The DOT-117 Specifications were deemed not strict enough in some areas, and this led to the Fixing America’s Surface Transportation (FAST) Act (1). Specifically, the FAST Act required increased thermal blanket protection for tank-cars, a risk-based approach to phasing out tank-cars carrying flammable liquids starting with crude oil tank-cars first, followed by tank-cars carrying ethanol, then followed by tank-cars carrying other flammable liquids and required top fittings protection on tank-car retrofits (1). These enhancements will help mitigate the consequences of rail accidents should they occur (1).

To improve the safety of tank-cars carrying hazardous materials, some have suggested a speed limit reduction, but examples such as the Seabrook, Texas derailment in January 2005, which occurred at only 5 mph show that even at lower speeds, puncture could occur and followed by the spilled diesel fuel catching on fire (7). To prevent future accidents, the Federal Railroad Administration (FRA) has shifted its research focus from tank-car safety under normal loading conditions to safety under accident conditions (8). This has resulted in new standards for tank-car survivability during impacts (8). As of the 2019-2020 National Transportation Safety Board Most Wanted List for safety recommendations, only 16 percent of tank-cars carrying flammable liquids meet their improved safety specifications for the DOT-117 and DOT-117R tank-cars (9). The improved requirements include a thicker shell of 1.4 cm (9/16 of an inch) and require thermal protection (10). Thermal resistance is important for keeping a hazardous material breach from spreading, as flammable liquids often ignite after being spilled which put surrounding tank-cars in further risk. Therefore, there is an immediate need for a novel material with superior puncture resistance, impact energy absorption capability and fire insulation properties to improve the safety of tank-cars carrying HAZMAT.

Metal foams are known for their high strength to density ratio, high specific stiffness, and greatly improved energy absorption and superior thermal characteristics (11,12,13). However, regular metal foams are not strong enough when considering huge tank-car impact energies. Composite metal foam (CMF) is a unique novel material based on a combination of properties of metal matrix composites and metal foams. CMF can be made out of 100% stainless steel and be as light as aluminum while offering close to two orders of magnitude higher energy absorption in compression compared to its parent material (13,14,15). The term composite metal foam refers to a class of metal foam made with hollow metal spheres surrounded by a metallic matrix (13,14,15). CMF has many physical and mechanical properties that make it suitable for a variety of applications including the structural material for tank-cars carrying HAZMAT.

Due to the regularity of its structure, uniform deformation under compression, and the presence of a matrix between the pores, CMF is able to maintain a relatively uniform plateau stress over large amounts of strain when loaded under compression, which offers large strength under both quasi-static and cyclic loading compared to other metal foams (13,14,15,16,17,18,19,20,21). Further studies of composite metal foams showed an increase in energy absorption performance under higher loading rates (22,23), which makes CMF more suitable for protection not only against the high speed impact of tank-cars, but also against various types of ballistic (24) and blast threats (25). Composite metal foams made from heavy metals such as iron, tungsten, and vanadium can offer reliable radiation shielding against a variety of sources from X-Rays (26), to neutron (27), and Gamma rays (28), but with the advantage of low density and great mechanical properties.

In order to further improve the tensile properties and corrosion resistance of metal foams, solid face sheets are normally added to the metal foam core to create sandwich panels. Metal foam core sandwich panels can be made using a variety of techniques depending on the material makeup of both the core and face. This includes bonding the face sheets to the foam core using adhesive bonding or traditional metal joining techniques such as welding, brazing, or solid state diffusion bonding (29,30,31,32,33,34). Each method has its own benefits and drawbacks such as the environmental limitations of the adhesive layer, localized heat affected zones within the weldment, and low shear strength of the brazing bond layer. Welding of the metal foams will also reduce the material porosity and, in turn, negate the benefits of using a metal foam core. This has made it difficult to find a consistent bonding method for manufacturing metal foam core sandwich panels. Diffusion bonding, however, can be easily modified for use on metal foams. Until recently, most metal foam core sandwich panels have used aluminum foam cores. However, both the performance and the bond strength between the core and the face sheets can be improved by using a high strength foam core, such as composite metal foam.

Testing of metal foams has shown that their strength in tension is much lower compared to that in compression (35,36,37,38,39). The network that makes up the foam surrounding the porosities is full of stress concentrations that allow for easy crack formation and propagation (35,36,37). CMF has one of the highest compressive and tensile strengths than any other metal foam (13,15). CMF's strength to weight ratio, unique impact energy absorption capabilities, and passive thermal insulating properties make CMF a leading candidate for sandwich panel structures. The metallic matrix between the hollow spheres creates a larger surface area to adhere face sheets to CMF's surface compared to other metal foams. The face sheets can help support CMF under tensile forces and improve the material's corrosion resistance in a variety of engineering and structural applications.

This study reports the manufacturing of SS-CMF and SS-CMF core sandwich panels and their testing under tension, compression and puncture conditions. The results of this study confirm and validate the potentials of SS-CMF material for application in the next generation of safer and more efficient puncture resistant tank-cars for transportation of HAZMAT. A full-scale puncture test will complete the evaluation of potentials that SS-CMF can offer for such applications.

On the other hand, metal foams have been known to make efficient and effective heat sinks due to their large surface area resulting from the presence of pores (13,40,41). As such, stainless steel composite metal foam is expected to be able to offer a reduction in heat transfer compared to bulk stainless steel due to the presence of air trapped within its spheres and porosities (13,40). These pockets of air within the composite metal foam help disrupt flow of heat through the material that can be seen in bulk stainless steel samples (13,40).

This study also reports the performance of steel Composite Metal Foam (SS-CMF) panels under full-scale Simulated Pool Fire Testing conditions in accordance with the 49 Code of Federal Regulations (CFR) Part 179, Specifications for Tank-car, Appendix B Procedures through both experimental and numerical approaches as well as a scaled-down simulated torch fire testing. The results validated the idea that steel composite metal foams can be a safer structural material for next generation rail tank-cars with improved puncture and fire resistance.

3 Manufacturing Methods

3.1 Manufacturing of Steel Composite Metal foam Panels

Steel-steel composite metal foam (SS-CMF) panels were manufactured using a powder metallurgy technique (22,14 ,42). Hollow stainless steel spheres are shaken into a random-loose packing arrangement within a steel mold and surrounded with a 316L stainless steel matrix powder. The word steel-steel composite metal foam refers to a type of CMF in which both the hollow metal spheres and the matrix are made of steel. The mold was then heated within a vacuum hot press and allowed to passively cool under high vacuum. The powder metallurgy manufacturing process can be found in greater detail in prior works (22, 16, 17, 14 ,42). Stainless steel spheres used for processing the SS-CMF panel were manufactured by Hollomet GmbH located in Dresden, Germany and had an average outer diameter of 2 mm with a wall thickness of 100 µm. The spheres were surrounded with 316L stainless steel powder from North American Höganas with an average particle size of 44 µm. Panels for various testing were manufactured in 30 x 30 cm and 25 x 25 cm sizes with a variety of thicknesses up to 2.5 cm. The resulting SS-CMF samples had a density of approximately 2.3 to 3.3 g/cm^3. Each sample panel was manufactured slightly over-sized and ground flat before any post processing treatment. In order to manufacture the SS-CMF core sandwich panels (SS-CMF-CSP), the SS-CMF core was attached to 3 mm or 6 mm thick 316 stainless steel face sheets either through adhesive or diffusion bonding. The elemental composition of the SS-CMF matrix, spheres, and face sheets are presented in Table 1.

Table 1.Chemical composition (wt%) of the material components that make up the SS-CMF and SS-CMF-Core Sandwich Panels.

	Chemical composition (wt%)						
Material	**Fe**	**C**	**Mn**	**Si**	**Cr**	**Ni**	**Mo**
2 mm Steel Balls	Balance	0.68	0.13	0.82	16.11	11.53	2.34
316L Steel Matrix Powder	Balance	0.03	2.00	1.00	16.00-18.00	10.00-14.00	2.00-3.00
316 Steel Face Sheet	Balance	0.08	2.00	0.75	16.00-18.00	10.00-14.00	2.00-3.00

3.2 Manufacturing of Steel Composite Metal Foam Core Sandwich Panels

After processing, each SS-CMF panel was cleaned and surface ground using a 35 x 150 cm Gallmeyer & Livingston Co. "Grand Rapids" grinding machine to create a flat surface across the entire front and back of each SS-CMF panel. Figure 1-a and -b show a 30 x 30 cm SS-CMF core panel and one of its related face sheets after grinding, respectively. The ground SS-CMF panels were then bonded to stainless steel face sheets of various thicknesses of 0.3175 cm (0.125 inch) or 0.635 cm (0.25 inch) on each side to create SS-CMF core sandwich panels. Note that the thinner face sheets did not need additional grinding due to their perfect flatness. But, the thicker face sheets needed slight additional grinding to achieve a flat surface that can be in close contact with the SS-CMF core creating strong bonding in between. The SS-CMF core has been bonded to face sheets through either diffusion bonding in a vacuum furnace or adhesive bonding.

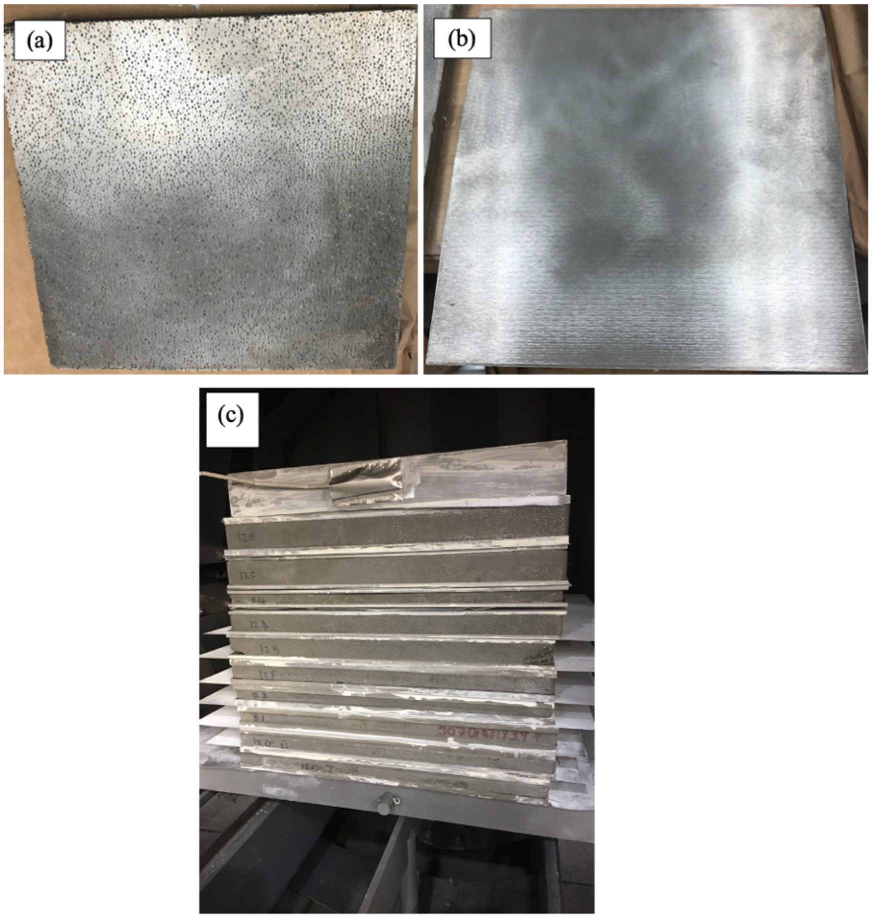

Figure 1. Digital images of (a) the top surface of a SS-CMF panel after grinding (b) the top surface of a steel face sheet after grinding, (c) a stack of 10 SS-CMF panels and 20 steel face sheets under a weight with a thermocouple attached to it inside of a vacuum furnace, ready for diffusion bonding to SS-CMF core sandwich panels.

The adhesive bonding of face sheets was conducted using a two-part aerospace epoxy (grade HYSOL EA 9330.3). The epoxy was thixotropic once mixed, making a consistent bond line thickness easier to achieve once the face sheets were affixed. The layered sandwich panels were assembled using a vacuum bagging technique and a 0.5 mm layer of epoxy between each component and cured at room temperature. A small filler with 0.5 mm thickness was placed in between the adhesively bonding surfaces (in each corner) as a space holder to make sure that the thickness of the adhesive layer was maintained at 0.5 mm on all samples. The required amount of adhesive bonding material was pre-calculated based on the thickness of the adhesive and its density along with the dimensions of the panels. The epoxy was then weighed with a small overage (+20%) and used for each panel. Any extra epoxy was pushed out during the vacuum bagging providing a uniform thickness across the entire surface of all panels.

The diffusion bonded S-S CMF-CSP were manufactured by sandwiching the ground SS-CMF panel between two steel face sheets in a vacuum furnace. The samples were stacked on top of each other with layers of molybdenum sheets coated with BN release agent placed between each set of sandwich panels to allow for easy removal following the run. Weighted plates were placed on top of the piled-up panels to promote diffusion of the sandwich panel face sheets and SS-CMF core. Figure 1-C shows the piled-up samples inside the furnace right before the diffusion bonding cycle started. A vacuum pressure of at least 1.3×10^{-3} Pa was achieved prior to turning on the heating elements. The SS-CMF cores were diffusion bonded to the face sheets with a heating cycle of 10ºC / min up to 850 ºC followed by a 30 minutes hold time at 850 ºC continued by 5 ºC/ min to 1200 ºC and a final hold at that temperature for 45 minutes. Upon the completion of the heat cycle in the vacuum furnace, the chamber was allowed to passively cool overnight until it reached a temperature below 100ºC, before the vacuum was released and the panels were removed.

A section from the diffusion bonded SS-CMF core sandwich panel went through additional preparation for imaging and analysis of the interface between the face sheets and the SS-CMF core. The sections were prepared using a Buehler Automet grinder/polisher using a progression of 320, 600, 800, 1200, and 2400 grit silicon carbide sandpaper. The samples were then electropolished with an ESMA E299-CC at a constant current of 10.5 Amps followed by etching using Adler's reagent to expose the grain boundaries and additional microstructural features. The microstructure of the samples was analyzed using a Hitachi SU3500 scanning electron microscope (SEM).

4 Microstructural Evaluations

A digital image of the top surface and cross-section of a base SS-CMF is shown in Figure 2(a), and a digital image of the cross-section of a SS-CMF core sandwich panel is shown in Figure 2(b). The top and bottom of each SS-CMF plate was machined or ground flat to create smooth parallel faces on either side for better bonding to the face sheets. The surface of the SS-CMF sample shown here has no open porosities as it was manufactured with added powder on the top and bottom of the panel for post-process machining in order to ensure flat and smooth surfaces to better bond to the face sheets at the top and bottom as shown in Figure 2(a). In some cases, porosities were opened up to the surface upon machining the SS-CMF core and those porosities were left open after diffusion bonding the SS-S-S CMF to the face sheets. Some of such these interfacial porosities are shown by red arrows in Figure 2(b). The effect of such porosities will be discussed in upcoming sections.

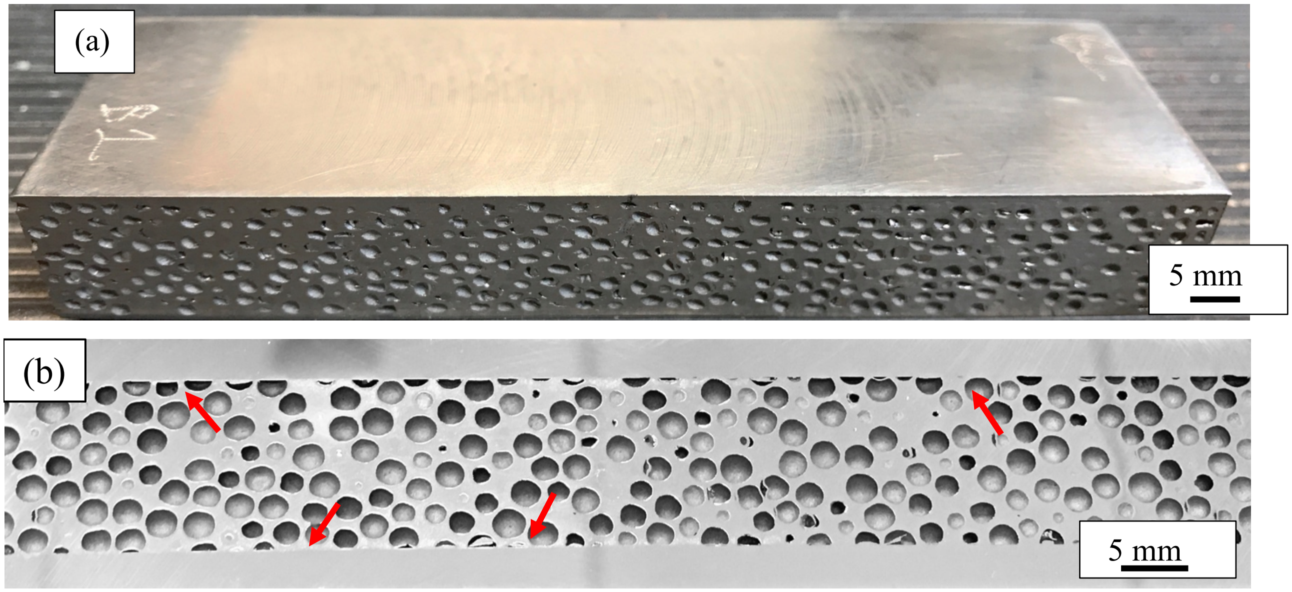

Figure 2. Digital images of (a) cross section and top surface of a SS-CMF panel after cutting and machining with no porosities open to the surface and (b) SS-CMF-sandwich panel with 3.175 mm steel face sheets and 12.5 mm SS-CMF core manufactured using diffusion bonding with some open porosities of SS-CMF at the interface between the core and face sheet (some shown by arrows)

Scanning Electron Microscopy (SEM) images of the base SS-CMF and the SS-CMF-CSP are presented in Figure 3(a, b, c) and (d , e, f) respectively. The general microstructure of SS-CMF is shown in Figure 3(a) with multiple spheres at each side of the image and the sintered matrix between them. Figure 3(a) shows the macro-porosities that are formed by the hollow metal spheres, and the micro-porosities that exist within the matrix, marked by white arrows. The metal matrix that fills the area between the spheres has micro-porosities that form during the powder metallurgy manufacturing process. The spheres are also manufactured using a powder metallurgy technique and contain micro-porosities in their sphere wall. In some areas, a small gap can be seen between the sphere wall and the matrix shown by a thin black arrow in Figure 3(a), while other areas show complete bonding between the spheres and matrix, marked by the thicker black arrow in Figure 3(a). Random gaps between the spheres and the matrix could have been caused by cutting, machining, and grinding the samples prior to SEM imaging. Continuous bonding is seen between the sphere walls and matrix surrounding most of the spheres. Various types of porosities can be seen in the higher magnification image in Figure 3(b) and are highlighted by the white arrows. The exposure of spheres to high temperatures associated with SS-CMF manufacturing causes sphere wall grain growth, as reported in our previous studies (14).

Figure 3(d) shows the consistent bond line between the core (marked as CMF) and the stainless steel face sheet (marked as SS FS). The bond line is hard to discern but is pointed to by the white arrows at the center of the figure. Figure 3(e) shows a separate region of the bonding at the sandwich panel interface between the SS-CMF matrix and the steel face sheet. The bond, marked by white arrows, is semi-continuous along the exposed surface, showing a slight gap between the core and the face sheet in some areas. The gaps most likely appeared during secondary treatment (cutting/grinding) of the sandwich panels for SEM imaging, indicating a lower bonding strength in that region. The gap was measured to be approximately 20 µm at its widest point. The gap varies along the surface and completely disappears further along the sample length, giving the face sheet enough strength to remain bonded. Higher magnification of the grains in the sphere wall of the SS-CMF-CSP is shown in Figure 3(f). The grains of the sphere wall in the SS-CMF-CSP are much larger than those in the base SS-CMF samples shown in Figure 3(c). This is due to the additional heat cycle experienced by the hollow spheres during diffusion bonding. The heat cycle is also expected to increase carbide formations along the grain boundaries, as has been reported in previous studies of SS-CMF, due to the higher carbon content of the spheres (14,21,22). Previous works have found that the carbide formations within the sphere wall are made up of Cr rich $M_{23}C_6$ carbides known to form in 316 stainless steels (14,15,43).

The spheres themselves are created using a powder metallurgy process and go through an additional heating cycle during the manufacturing of the SS-CMF panel. This leads to additional grain growth in the sphere wall when compared to the matrix as reported in our previous studies (14, 15, 22). It has been reported that carbide precipitations are mostly formed at the grain boundaries of the sphere walls due to both the effects of the additional heat cycle during the manufacturing of the SS-CMF as well as the higher starting carbon content of the spheres (15).

Multiple images were taken at a constant magnification of the base SS-CMF and SS-CMF-CSP and were analyzed using ImageJ to obtain an average of over 100 grain size measurement for the matrix and sphere wall. The average grain size of the matrix and sphere walls for the SS-CMF and SS-CMF-CSP are listed in Table 2. Following the additional heat cycle of manufacturing the diffusion bonded sandwich panels, the average matrix grain size increases from 32 µm to 45µm and the average sphere wall grain size increases from 39 µm to 49 µm. The grain growth can be seen by comparing Figure 3(c) and (f).

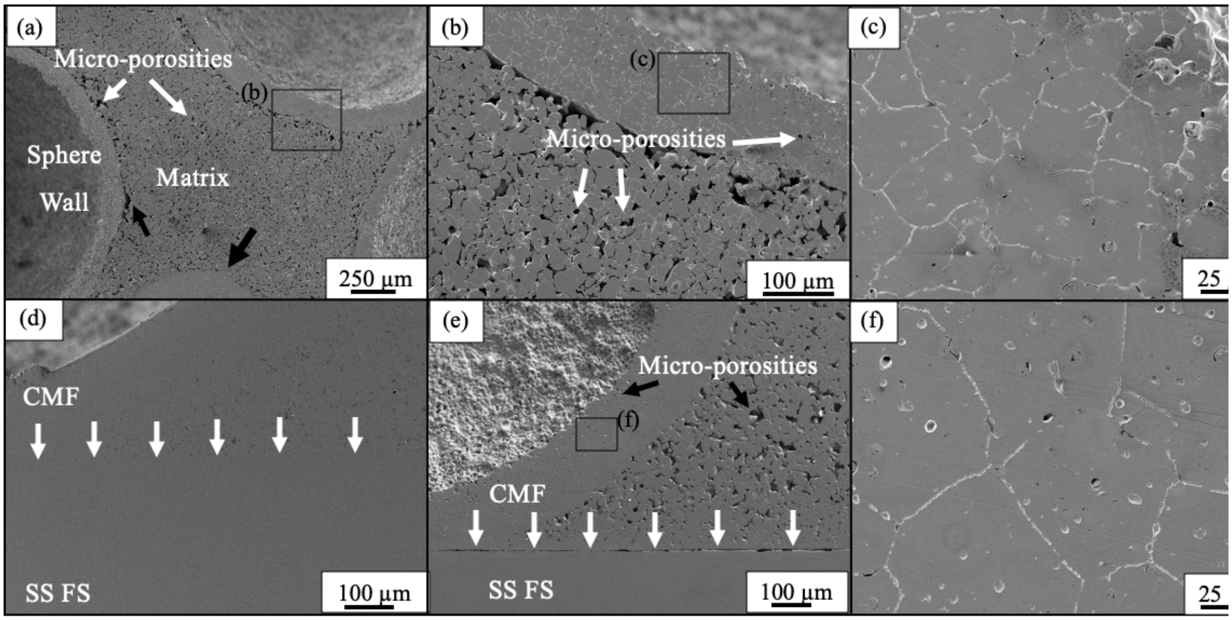

Figure 3. SEM images of the (a)-(c) base SS-CMF microstructure and the (d)-(f) SS-CMF-CSP. The micro-porosities and the solid bond between the sphere wall and the matrix are highlighted in (a) and (b) by arrow. White arrows in (d) and (e) are used to show the bond line of the SS-CMF core and the small gap that exists in some areas. The grain size in the sphere wall is compared between the base SS-CMF and the SS-CMF-CSP in (c) and (f) respectively.

Table 2. Measured grain size of the matrix and sphere wall for the base SS-CMF and diffusion bonded SS-CMF-CSP.

	Matrix Grain Size (µm)	**Sphere Wall Grain Size (µm)**
Base SS-CMF	32	39
Diffusion SS-CMF-CSP	45	49

5 Compressive Properties of Composite Metal Foam and Composite Metal Foam Core Sandwich Panels

5.1 Abstract

Stainless steel composite metal foam core sandwich panels (SS-CMF-CSP) were manufactured in large-scale panels and tested under quasi-static compression. Stainless steel face sheets were attached to the SS-CMF core using two methods: diffusion and adhesive bonding. The face sheets were found to not greatly affect the deformation of the SS-CMF core under compression. However, the diffusion bonded SS-CMF-CSP yielded a slightly stronger product primarily due to the diffusion of carbon from the sphere walls into the surrounding matrix that led to the formation of carbides in those areas. The diffusion bonded SS-CMF-CSP had a plateau stress and densification stress of 17% and 10% higher than its baseline SS-CMF, respectively. The large-scale manufacturing was optimized, and additional samples were tested with a yield and plateau strength higher than the initial SS-CMF samples. The optimized diffusion bonded SS-CMF-CSP showed similar strengthening, with a plateau stress 16% higher than its base SS-CMF. Finite element analysis was completed using IMPETUS Afea that advances the current modeling of SS-CMF and was found to be in good with the experimental findings.

5.2 Testing Setup

A panel of 25 x 25 cm size with a thickness of 2.5 cm was manufactured for compressive testing purposes. The panel was manufactured slightly over-sized and ground flat before any post treatment or bonding process. Three sample sets were cut from the panel: the first was used to test the properties of the base SS-CMF core, the second for adhesive bonding, and the third for diffusion bonding. The resulting SS-CMF samples had a density of approximately 2.85 g/cm^3. In order to manufacture the SS-CMF-CSP, the SS-CMF core was attached to 3 mm thick 316 stainless steel face sheets either through adhesive or diffusion bonding. The elemental composition of the SS-CMF matrix, spheres, and face sheet are presented in Table 1.

Quasi-static compressive tests were conducted on an MTS 810 servo-hydraulic universal testing machine equipped with a 980kN load cell using displacement control at a rate of 1.27 mm/min. A digital camera was used to image each sample during loading. Lubrication in the form of polytetrafluoroethylene (PTFE) sheets and vacuum grease were placed at the interface between the sample and the planets in order to reduce friction and barreling effects during compression testing. The displacement and load data were recorded using an attached computer and were used to calculate the appropriate stress-strain curves for each sample. All samples were tested under the same loading conditions to be able to easily compare the generated data between various tests.

5.3 Modeling Setup

IMPETUS Afea Solver was chosen to model the performance of SS-CMF under compression due to its high order element technology. The computational time of IMPETUS is reduced by implementing central processing unit (CPU) (NVIDIA CUDA) technology, which allows a graphics processing unit (GPU) accelerator to assist the CPU in solving large deformations and fracture models (42).

In this study a quasi-static compression model of CMF is created using IMPETUS Afea software. This software has effectively been used to model CMF panels under blast and fragment impact (25). The prior model was made using a bulk mesh to represent the CMF layer, and disregarded the sphere geometry that makes up CMF's unique structure. In this work, efforts are made to model the CMF using a porous geometry and determine the necessary variables to obtain reliable yielding under quasi-static compression. The model is created by reflecting and expanding of a 1/8 unit cell containing a section of the sphere and matrix shown in Figure 4(a). The model uses a random-loose packing structure between cubic and body centered cubic (BCC). The final sizing of the spheres inside the SS-CMF is a modified BCC structure of hollow metal spheres with a small spacing placed between porosities to create a packing density of approximately 59%, consistent with what is seen in manufacturing of CMF (14). The sphere walls are considered part of the matrix material as to not create an additional interface between the two bodies. This model uses a baseline construction of the CMF geometry and does not incorporate the effects of the air within the spheres into the calculations but does expand upon previous works by including the porous geometry of the CMF structure. IMPETUS Afea is suited for future studies involving high rates of deformation and the effects of air inside the spheres using discrete particle-based modeling (17, 16).

The model was meshed using tetrahedral elements with a length of 0.6 mm, as can be seen in the unit cell in Figure 4(a). The sphere wall is shown meshed separately with a smaller element length of 0.3 mm. The smaller elemental size improves the resolution of the results and avoids compiling errors during deformation of the spherical pores under compression. The two bodies, the sphere and matrix, are modeled with the same material properties and assumed to be in contact during loading. The unit cell is reflected within the body to create the compression sample. The model is run in quarter symmetry, as can be seen by the input in Figure 4(b), with a taller sample size than what was tested experimentally and attains reliable results. The entire mesh of the compression sample is presented in Figure 4(c).

Modeling materials under quasi-static compression is relatively simplistic, however the porosities within composite metal foam make the finite element analysis more complex. Metal foams show three distinct loading regions: (i) initial elastic region, (ii) plateau region, and (iii) densification region. There have been a variety of methods used to model metal foams under compression which work to balance the perfectly plastic realm presented by the plateau stress, and the innate hardening of the material as it approaches densification in order to effectively predict the materials energy absorption

(44,45). In this work, two constitutive models are paired with the geometric meshing of the sample in order to best approximate the loading of SS-CMF under compression. The CMF is modeled as an elastic- perfectly plastic material that assumes a constant stiffness following yield. The material parameters used for the SS-CMF are taken from prior works with a density of 2.9g/cm^3, a modulus of 13.2 GPa, and a Poisson ratio of 0.1 (24, 46).

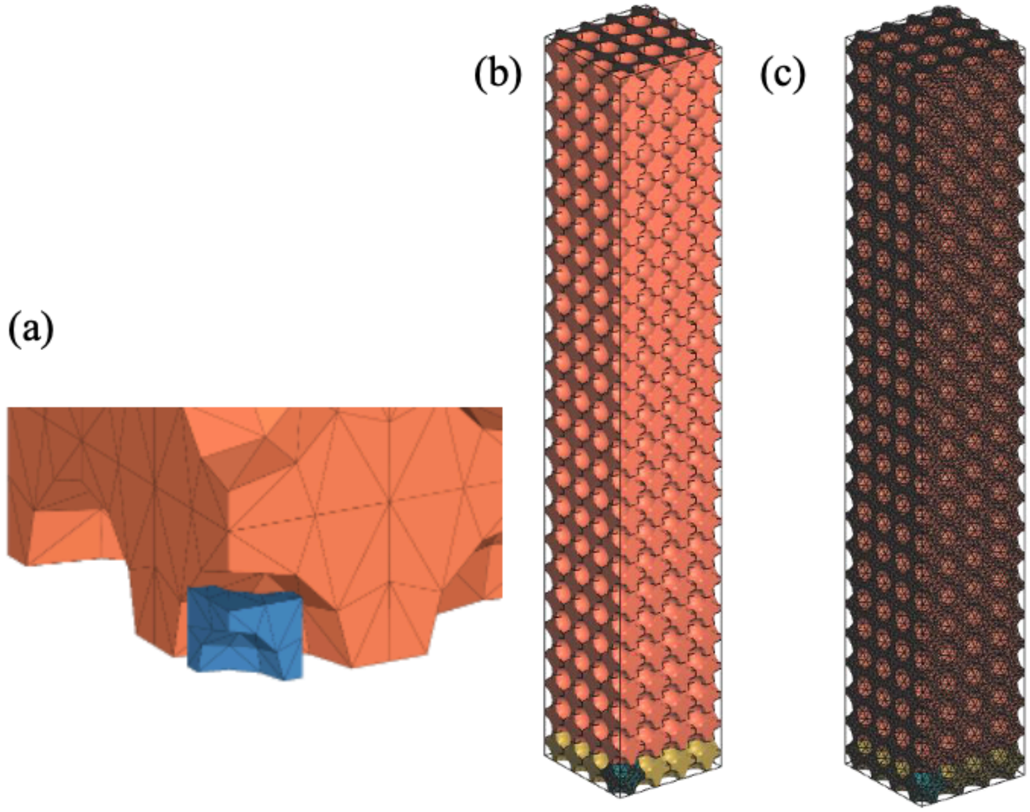

Figure 4. (a) Image of the 1/8 unit cell arrangement with meshing used to create CMF model (b) the quarter symmetry compression model used for simulating CMF and (c) the fully meshed quarter symmetry sample used for testing.

5.4 Results and Discussion

Structural Properties

Digital images of the compression test samples cut from the base SS-CMF and the SS-CMF-CSP are shown in Figure 5. Figure 5(a) shows the base SS-CMF with the sphere openings being exposed following sample cutting. The openings have a varying diameter and depth as the cuts are not at the true center of each sphere. The spheres are sitting in various positions vertically along the sample wall given the inherent packing arrangement obtained during manufacturing of SS-CMF.

The adhesive bonded SS-CMF-CSP can be seen in Figure 5(b). The bond line is relatively constant across the top and bottom of the sample. The adhesive is able to infiltrate the open sphere porosities at the top and bottom surface of the sample, creating a stiff bond between the core and face sheets. Previous works on SS-CMF have shown a high infiltration percentage of 88% epoxy infusion into SS-CMF under vacuum curing (47). These samples were cured under atmospheric pressure but aided by additional clamping force to ensure continuous contact between the core and face sheets. This helps to promote filling of the contact surface open spheres but does not necessarily infiltrate the micro-porosities within the matrix. The epoxy layer creates a stiff bond against the core and face sheets, but it is important to note that its strength can be affected by both heat and moisture while in service, degrading its adhesive properties. On the other hand, the diffusion bonding (Figure 5(c)) will only occur along the surface of the SS-CMF and does not penetrate the open porosities. This means that inherent gaps may exist along the surface where the hollow core of the spheres lie open to the face sheet. The diffusion bonding does have benefits over the adhesive bond as it does not dramatically alter the properties of the SS-CMF core. The diffusion bond has similar limitations to the base metal and does not further restrict the application of the sandwich panel under extreme heat, fire and moisture exposure conditions, unlike adhesive bonds.

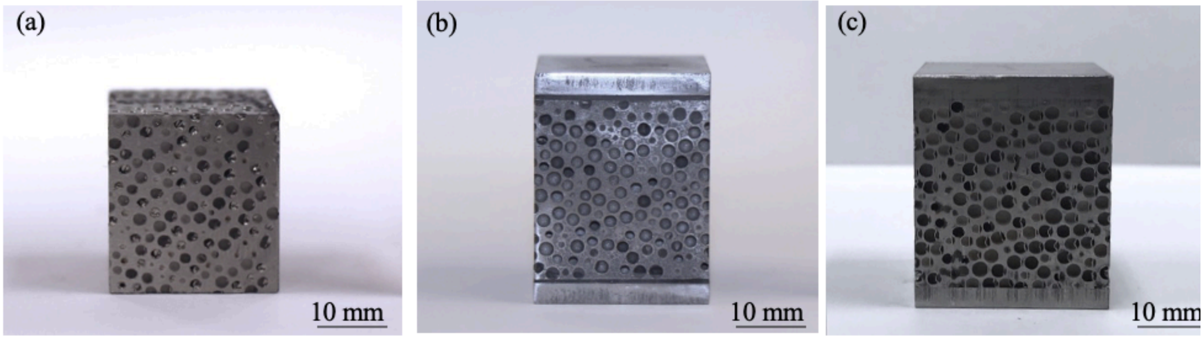

Figure 5. Digital images of the (a) base SS-CMF, (b) adhesively bonded SS-CMF-CSP, and (c) diffusion bonded SS-CMF-CSP compression samples prior to testing.

Mechanical Properties and Compressive Strength

The engineering stress-strain curves for the as-processed SS-CMF and SS-CMF-CSP under compression are shown in Figure 6. The plot includes three tests for each sample type compiled together. The strain was calculated using the dimensions of the SS-CMF core, (25 x 25 x 25 mm), as the face sheets were found to not greatly influence the deformation of the core under compression. The plot of the base SS-CMF is represented by the solid lines. The shape of the curve is representative of SS-CMF under compression. The SS-CMF undergoes an initial yield followed by a plateau stress where the hollow metal spheres deform at a relatively constant stress until densification is reached at about 60-65% strain and the sample stiffens (21, 42).

The base SS-CMF sample's curve is overlapped with the adhesive bonded samples shown by the dashed lines in Figure 6. The two sets have a very similar stress-strain curve as the face sheets do not have a noticeable effect on the mechanical strength of the SS-CMF-CSP structure under compression. The adhesion bonded samples experience multiple drops in stress at various strain levels during compression. This is attributed to the lateral expansion of the core under compression causing its shifting at the interface of the adhesive bond during the compression and a momentary lapse in the readout registered by the load cell. The drops occur at strains following the initial yield, signifying that it may be due to core motion against the adhesive bond during deformation of the sample. During compression, the porosities within the SS-CMF core naturally collapse, but the layers in contact with the epoxy layer are held stiff, impeding uniform deformation in the core. This causes momentary shifting of material as additional layers begin to deform and the stress-strain curve returns to its normal path.

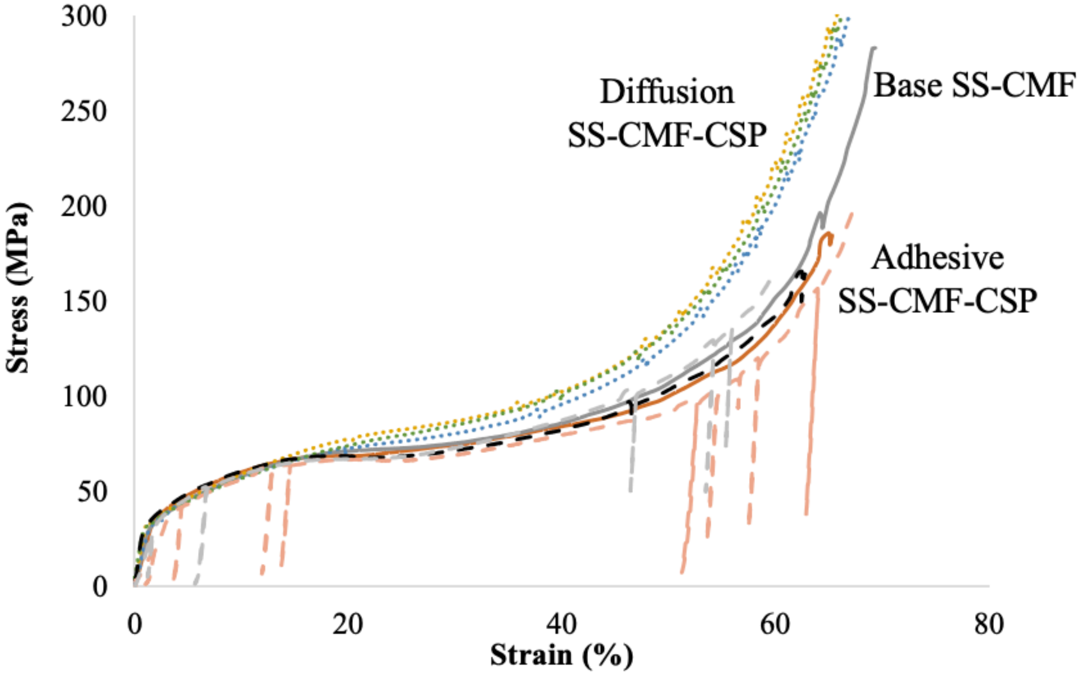

Figure 6. Compressive stress-strain curves of scaled SS-CMF and SS-CMF-CSP (unoptimized).

The diffusion bonded SS-CMF-CSP samples are shown by dotted lines in Figure 6 and were slightly stronger than both the as-processed SS-CMF and adhesion bonded sandwich panels. The strengthening is not necessarily caused by the addition of the face sheets, as the adhesive bonded samples have shown no strengthening effect, but is likely caused by the additional heat cycle during diffusion bonding. Generally, the larger grain size in both the matrix and sphere wall of SS-CMF core sandwich panels, discussed in previous section, is expected to increase the ductility of the material and decrease its hardness. However, a slight strengthening effect can be seen at strains above 17% of all sandwich panels. The yield and early plateau stress are not affected, meaning the strengthening is occurring during the deformation and collapse of the hollow metal spheres and its surrounding matrix. The magnitude of the strengthening is not drastically high but is consistent across all three diffusion bonded SS-CMF-CSP samples. It is expected that the additional heat cycle during diffusion bonding promotes diffusion of carbon from within the sphere walls to the surrounding matrix. The increased carbide formation in the matrix and around the sphere walls stiffen the material under compression. The carbides are most likely isolated to around or within the sphere walls which results in a steeper slope between 16 – 50% strain. The carbides resist dislocation motion during compression of the spheres which do not begin to collapse until after yield, explaining why there is no difference in the samples' yield strength. The stress-strain curve of the diffusion bonded SS-CMF-CSP also shows a step like shape at strains above 50%. This is thought to occur for a similar reason attributed to the epoxy bonded samples, but to a lesser effect, as the diffusion bond has a lower mechanical impedance than the epoxy interface. The lateral expansion of the core at high strains and subsequent interaction at the bond line causes a rise and fall in the stress measured by the load cell during the densification phase, creating the step like pattern.

Images of the compression samples at 0% strain and 60% strain are shown in Figure 7. The base SS-CMF in Figure 7-a and Figure 7 -b undergoes uniform deformation up to 60 % strain. The adhesive bonded SS-CMF-CSP in Figure 7-c and in Figure 7-d does show some asymmetric behavior and slight shearing occurring within the core. This is due to the formation of a large dead zone at the top and bottom of the sample. The larger dead zone is created by the stiff interface of the adhesive bond and limits the lateral expansion and resulted motion of the core, causing an asymmetric yielding behavior at high strains. The diffusion bonded samples in Figure 7-e and Figure 7-f did not experience such limitations and had uniform deformation through densification, similar to the base SS-CMF. The diffusion bonded SS-CMF-CSP were able to uniformly compress up to 70% strain without the core cracking or failing. It can be seen that the SS-CMF core bulges out of the width of the face sheets, yet it does not separate from either of the face sheets. The top and bottom faces are still in contact with the edges of the face sheets. The bond layer created during the diffusion process allows enough motion between the face sheets and the core to accommodate the sample's lateral expansion during compression without separating at the bond interface.

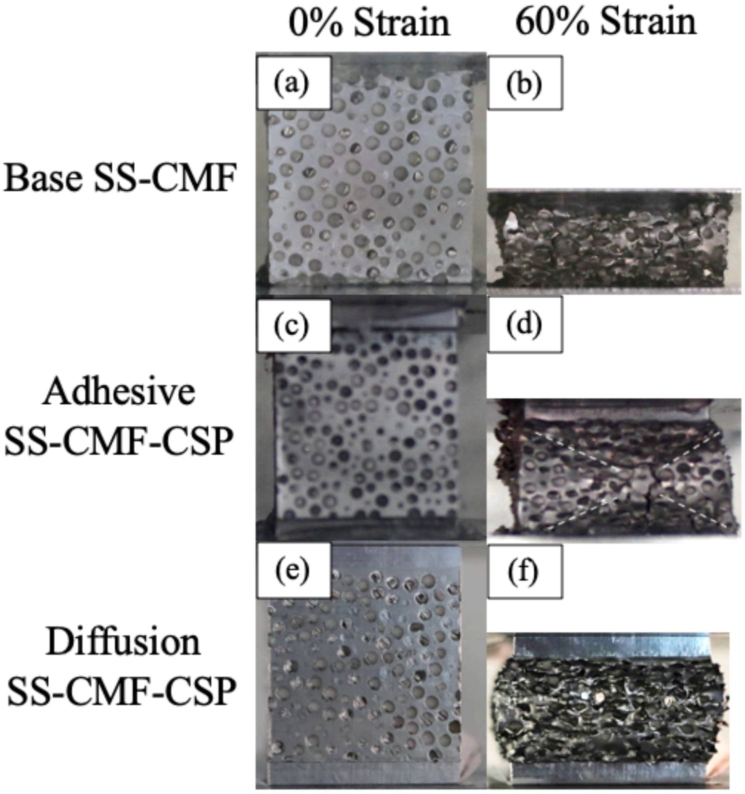

Figure 7. Images at 0% strain, left, and 60% strain, right, of the (a-b)SS-CMF base, (c-d) adhesive bonded SS-CMF-CSP, and (e-f) diffusion bonded SS-CMF-CSP.

The initial samples manufactured using the large-scale process have a lower strength than what has previously been established for SS-CMF tested on smaller scale samples (42,15,14,16). As such the processing parameters were optimized for the large scale manufacturing and the stress-strain curves of the initial SS-CMF and SS-CMF-CSP compared to the optimized samples are plotted in Figure 8. The curves plotted are an average of three tests with the base SS-CMF plotted in a solid red line, the adhesive SS-CMF-CSP in a black dashed line, and the diffusion bonded SS-CMF-CSP in a dotted green line. It can be seen that the optimized sample set are performing better than the initial tests. The improvement in mechanical strength is credited to a superior sintering process that creates a more cohesive matrix and a stronger bond between the matrix and sphere walls. Figure 8 shows a similar strengthening behavior in diffusion bonded optimized samples (shown in dotted green line) at strain levels between 17-60%. Similar to the prior discussion on un-optimized samples, this strengthening can be attributed to the carbide formation within the sphere walls and their immediate surrounding matrix during the heat cycle of manufacturing sandwich panels. This explains why the yield strength and early plateau of the material is not greatly affected as those properties are mostly controlled by the matrix deformation, but rather, this phenomenon occurs at higher strains during the deformation and collapse of the sphere walls. The strengthening continues up through densification to approximately 60% strain, where it begins to converge with the base SS-CMF stress-strain curve.

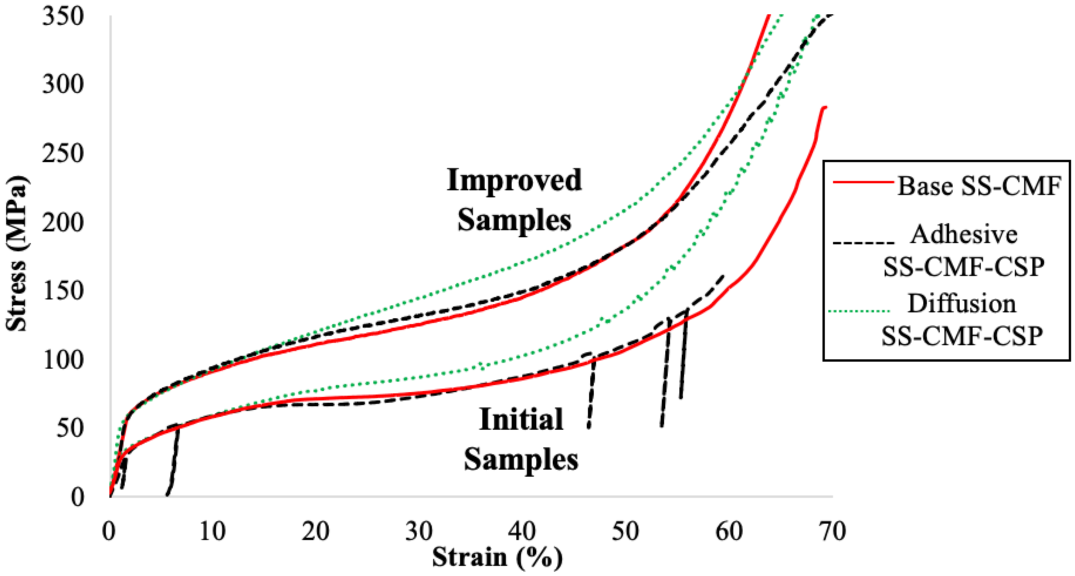

Figure 8. Compressive stress-strain curves of scaled SS-CMF and SS-CMF-CSP compared to the improved/ optimized scaled samples.

The mechanical properties of the initial scaled and optimized scaled SS-CMF and SS-CMF-CSP are presented in Table 3 alongside the compressive properties previously established for small-scale manufactured SS-CMF. The diffusion bonding increases both the plateau stress, measured at 30% strain, and the densification stress of the SS-CMF material under compression for both sample sets. The initial diffusion bonded samples see a 17% increase in plateau stress and 10% increase in densification stress over the base SS-CMF. The optimized SS-CMF-CSP set shows a similar increase with a 16% improvement in plateau stress and a 9% rise in densification stress. Meanwhile, both the base SS-CMF and adhesively bonded SS-CMF have similar values for both sets of tests. The energy absorption of the SS-CMF samples can be approximated in MJ/m^3 by calculating the area under the stress-strain curve. The energy absorbed by each sample is also listed in Table 3. It was found that the energy absorbed by the diffusion bonded SS-CMF-CSP increases for both the initial and optimized scaled sample sets by approximately 5-7% when compared to their respective base SS-CMF. The improved/ optimized SS-CMF sample absorbs 35% more energy than the unoptimized samples and is in good agreement with the small scale SS-CMF samples from prior works (14). This data shows good adaptation of SS-CMF processing to large-scale manufacturing. Future mechanical testing of SS-CMF sandwich panels will use the optimized manufacturing process with a higher strength than originally achieved scaled manufacturing. The compression results helped to improve the final manufacturing settings for large-scale SS-CMF panel processing as well as investigate the effects of microstructural changes on the final strength of the samples.

Table 3. Mechanical properties of the scaled base SS-CMF and SS-CMF-CSP under compression compared to prior small-scale SS-CMF and the improved/ optimized scaled samples.

	Yield strain (mm/mm)	**Yield Strength (MPa)**	**Plateau Strength at 30% (MPa)**	**Densification Strain (mm/mm)**	**Densification Stress (MPa)**	**Specific Energy Absorption (MJ/m^3)**
Base SS-CMF	1.36	30.51	73.17	61.50	156.44	48.8
CMF-CSP Adhesion bond	1.68	33.10	73.13	58.06	134.21	42.2
CMF-CSP Diffusion bond	1.25	31.29	85.13	55.45	170.06	51.2
SS-CMF(Prior Work (7))	1.06	43	127	54	217	67.8
Optimized Scaled Samples						
Optimized Base SS-CMF	1.64	54.94	125.71	55.32	217.12	66.5
Optimized SS-CMF-CSP Adhesion bond	1.63	47.73	132.94	55.84	218.61	68.5
Optimized SS-CMF-CSP Diffusion bond	1.51	56.70	145.63	54.53	237.66	71.0

Modeling Results

The stress-strain curve of the SS-CMF model under quasi-static compression is shown alongside the experimental results in Figure 9(a). The elastic- perfectly plastic material model paired with the porous geometry was found to be in good agreement with the experimental results. The model used a multilinear stress-strain relationship up to 15% yield for the initial onset of the plateau stress. After this point, the model assumed a constant stiffness and allowed the geometry of the SS-CMF to dictate the hardening behavior through the plateau region towards densification. The early plateau region is slightly lower than the experimental values between 12-30%, but the model does correct itself relatively quickly as it continues to deform.

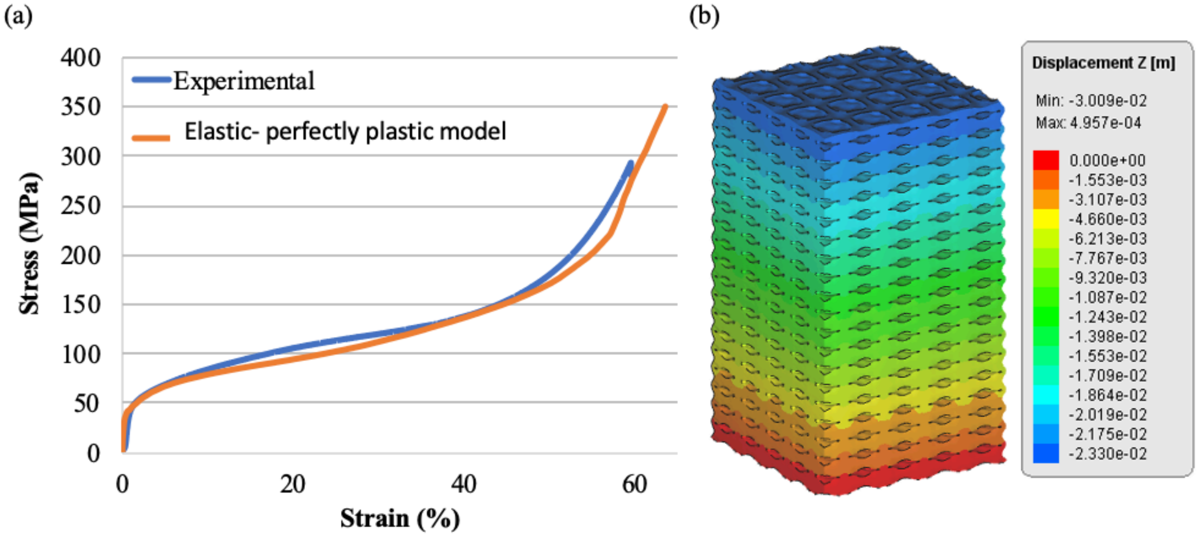

Figure 9. Generated finite element results showing the (a) stress-strain curve obtained using an elastic- perfectly plastic material model paired with the geometric meshing and (b) the simulated SS-CMF sample deformed to 50% strain showing the distribution of displacement throughout.

The geometry gives the displacement curve a relatively consistent slope between 25% to 55% strain that is similar to the experimental data. Densification was appropriately accommodated for by the geometry of the sample as the pores representing the hollow spheres are deformed and stiffen the overall product, as can be seen by the SS-CMF model displaced to 50% strain in Figure 9(b).The quarter symmetry representation in Figure 9(b) shows the collapsed spheres throughout the body as densification of the SS-CMF begins. The specific energy absorption of the model up to 50% stain was measured through the finite element analysis as 56.2 MJ/m^3, which is in close proximity to the experimental findings reported in Table 3. The model's results are slightly lower than the experimental values as it does not consider the effect of air inside closed spheres that resist against deformation resulted compression. Future modeling can aim to incorporate the same geometry used herein and validate it under various loading conditions such as bending and tension as well as considering the air inside the spheres and its effect on the performance of the material under loading.

5.5 Conclusion

In summary, composite metal foam and composite metal foam core sandwich panels were manufactured and tested under quasi-static compression. Two bonding methods, adhesive and diffusion bonding, were tested and compared to the as-processed SS-CMF samples using large-scale manufacturing. It is observed that the face sheets had little effect on the SS-CMF performance under compression, however it did show the viability of multiple attachment methods for future testing of SS-CMF-CSP. Due to the limitations of the epoxy adhesives under heat and moisture exposure and its high stiffness hindering the lateral expansion of the core, it does not seem to be the most effective means of manufacturing SS-CMF-CSP. The diffusion bonding process on the other hand created a cohesive bonding with flexible interface to accommodate lateral deformation during compression and seems to be the most effective means of manufacturing SS-CMF-CSP.

It was also found that the diffusion bonding created a larger grain size in both the matrix and sphere wall during the additional heat cycles the samples were put through. The larger grain size is expected to increase the ductility and reduce hardness of the core, but a strengthening effect was seen for the SS-CMF-CSP. The strengthening is attributed to the secondary heat cycle that promoted diffusion of carbon from the spheres into the matrix. The resulting carbide formation in the matrix surrounding the sphere walls improves the strength of the material above 17% strain. The microstructural changes created a stronger product with 17% higher plateau stress and 10% higher densification stress with uniform deformation under compression.

Additional samples were manufactured with optimized sintering scaled manufacturing parameters to show improvement in the mechanical properties. The optimized samples had a plateau strength approximately 16% higher and absorbed 35% more energy than the unoptimized samples. The second set of tests on the improved SS-CMF and SS-CMF-CSP samples showed a similar trend when comparing the stress-strain curves. The diffusion bonded SS-CMF-CSP continues to show strengthening above 17% strain which can be attributed to additional carbide formation inside and around the sphere walls. The optimized large-scale SS-CMF plates are to be used for future mechanical testing that include tension of SS-CMF and SS-CMF-CSP and puncture test of S-S CMF-CSP. Finite element analysis was completed using Impetus Afea to model the SS-CMF under compression with a complex geometry. The simulation results show good agreement with the experimental work. The measured energy absorption of the SS-CMF was consistent with experimental findings and shows progress to modeling a complex material such as SS-CMF.

6 Tensile Properties of Composite Metal Foam and Composite Metal Foam Core Sandwich Panels

6.1 Abstract

Stainless steel composite metal foam (SS-CMF) and composite metal foam core sandwich panels (SS-CMF-CSP) were manufactured and tested under quasi-static tension. The SS-CMF-CSP were manufactured by attaching stainless steel face sheets to SS-CMF core using solid-state diffusion bonding. The base SS-CMF samples had an ultimate tensile strength between 75-85 MPa and a failure strain between 7.5-8%. The normalized tensile strength of the SS-CMF was approximately 24 MPa/(g/cm^3), at least five times higher than that of other comparable metal foams, with a specific energy absorption of 0.95 J/g under tension which is almost an order of magnitude higher energy absorption per gram of the foam compared to other metal foams. The presence of a matrix bonding the uniformly distributed porosities together seem to be the strengthening factor of SS-CMF under tension when compared to other metal foams. The ultimate tensile strength of the SS-CMF-CSP was more than twice that of the base SS-CMF at 165 MPa with an average failure strain of 23%. The normalized strength of the SS-CMF-CSP was 52% higher than the base SS-CMF. The face sheets support and the microstructural changes during the diffusion bonding heating cycle were found to impact the failure mode of the SS-CMF core. The modulus of elasticity was approximated using the rule of mixtures for the SS-CMF and the SS-CMF-CSP and the experimental results was found to lie within the calculated bounds.

6.2 Materials

Two 25 x 25 cm steel-steel composite metal foam (SS-CMF) panels were manufactured using a powder metallurgy technique (22, 14 ,17) as explained in prior sections of this report. One panel was used to test as base SS-CMF and the other was used to manufacture SS-CMF-CSP. The resulting SS-CMF samples had a density between 2.9 and 3.1 g/cm^3 and a thickness of 13 mm. The panels were manufactured slightly over-sized and ground flat before any post processing treatment or bonding to the face sheets. The SS-CMF-CSP was manufactured by attaching one of the SS-CMF panels to two 3.175 mm (1/8”) thick 316 stainless steel face sheets through diffusion bonding. Multiple dogbone tensile samples were sized in accordance with ASTM-E8 standard and cut using a wire electric discharge machine (EDM) from the SS-CMF and SS-CMF-CSP panels (48). The tensile dogbone samples were cut with a gauge length of 90 mm and a cross section of approximately 12.7x12.7 mm. Following cutting, all surfaces of the samples were hand ground to remove particulates and discolorations caused by the wire EDM process. The samples were then cleaned in an ultrasonic bath of water and soap solution followed by another bath of acetone in order to remove loose particles and contaminants before testing.

6.3 Testing Setup

The SS-CMF and SS-CMF-CSP dogbone specimens were tested under quasi-static tension using an MTS QTest TM012 universal testing machine equipped with a 98kN load cell. At least three samples were tested from both the SS-CMF and SS-CMF-CSP panels. The samples were placed within pneumatic grips and displaced at a rate of 1.27 mm/min at room temperature in accordance with ASTM-E8 control method B (48). The load and displacement were recorded by a computer connected to the frame's load cell and used to create the stress-strain curves. Images of the samples during tension were taken using a digital camera and analyzed following testing to understand the failure of SS-CMF and SS-CMF-CSP under tension. All samples were tested under the same loading conditions to facilitate easy comparison between various tests.

6.4 Results and Discussion

Steel Composite Metal Foam Under Tension

The stress-strain curves resulted from tensile tests of the SS-CMF samples are plotted in Figure 10(a). The shape of the curves is expected for metals and more specifically for metal foams (49, 50). There exists an initial linear elastic region up to about 0.75% strain followed by plastic deformation to the ultimate tensile strength leading to the final failure. The relatively low strains are expected for metal foams due to the presence of porosities within their structure and their resulted stress concentrations under tension. The ultimate tensile strength of the SS-CMF samples was found to be between 75-85 MPa with a failure strain between 7.5-8%. The average yield strength, ultimate tensile strength, failure strain, and elastic modulus of all tested samples are reported in Table 4. The energy absorption by each sample up to its failure was found by calculating the area under their stress-strain curves and is reported in units of MJ/m^3 in in Table 4. As can be seen, the tensile strength of SS-CMF is much higher than those reported for other comparable metal foams (35,36, 37 ,39 ,51). Given the variation in relative densities of metal foams, it is best to normalize the strengths by each sample's density before comparing those.

The normalized stress-strain curves for the base SS-CMF are plotted in Figure 10(b). A consistent behavior can be seen between all samples given their slight variation in density. When normalized, all of the samples show a maximum tensile strength of approximately 24-25 MPa/(g/cm^3) where other metal foams have a maximum normalized strength less than 5 MPa/(g/cm^3) (35,36, 37). The superior strength of SS-CMF compared to other metal foams is due to the presence of a metallic matrix that bonds the uniformly distributed porosities together. The hollow metal spheres create a consistent porosity size within the SS-CMF's structure compared to other metal foams with a larger variation in their cell size and cell wall thicknesses (35,36, 37).The unique structure of SS-CMF gives it a normalized tensile strength five times higher than other metal foams. The specific energy absorption of the SS-CMF under tension was found by dividing the energy absorbed by its density and is compared to that of other metal foams in Table 5. The specific energy absorption of the SS-CMF is found to be about 0.95 J/g whereas other metal foams absorb 0.13 J/g, making SS-CMF almost an order of magnitude more efficient in tension and a much better candidate to be used as the core of sandwich panels.

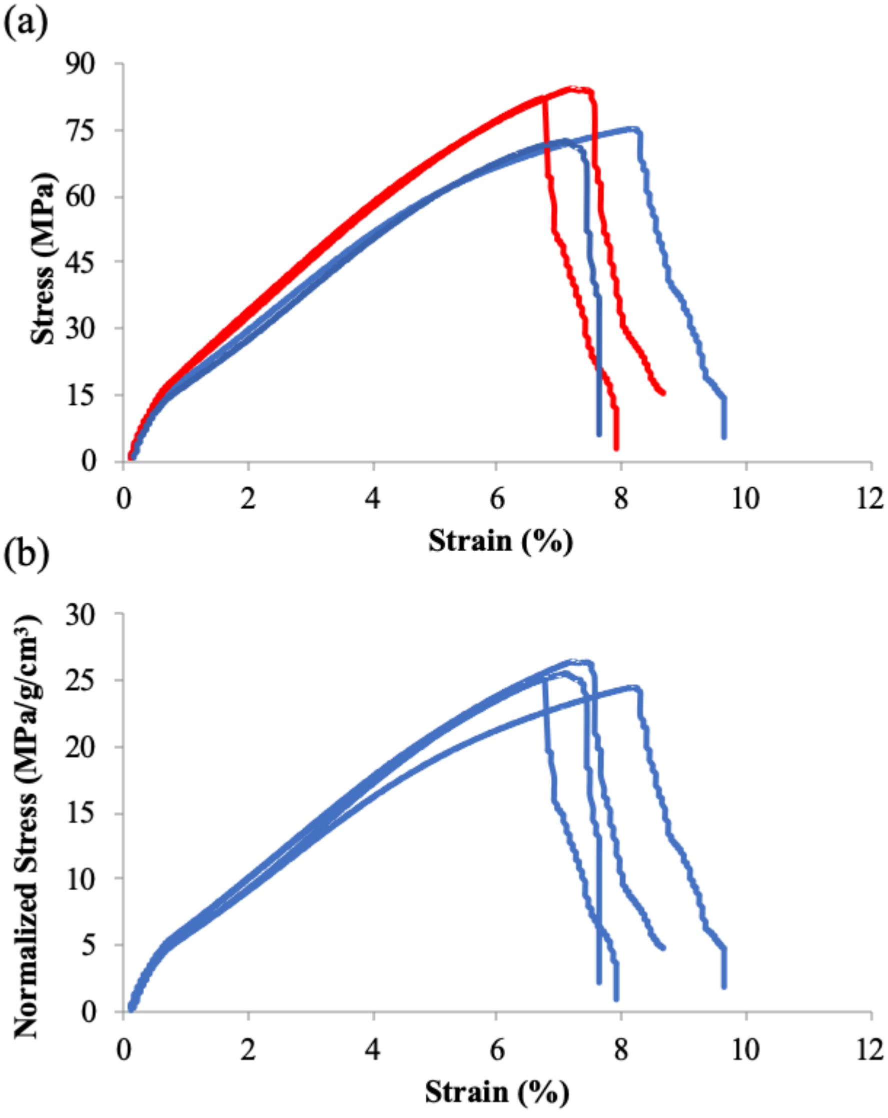

Figure 10. (a) Engineering tensile stress-strain curves of the base SS-CMF samples, and (b) the stress strain curve normalized by the density of each SS-CMF sample.

Digital images taken from the sample during tensile testing are shown in Figure 11. These images show the failure mode of the base SS-CMF is similar to its parent material (steel), with the cracks initiating and growing along the outer surface and then propagating through the thickness of the dogbone sample. The crack propagation in

Figure 11(b)-(e) is highlighted by the magnified images at the bottom of the figure. As can be seen in Figure 11(b-i), the crack initiated at the surface near a hollow sphere open to the surface. The crack proceeds across the surface of the sample prior to moving through the thickness, as seen in Figure 11(d-i). The crack initiation is between 6.0-6.25% strain followed by a progression of failure over a strain percentage of approximately 1% seen by comparing images in Figure 11(c)-(e).

Table 4. Average mechanical properties for SS-CMF and SS-CMF-CSP tested under quasi-static tension. The values from other metal foams are presented for comparison.

	Tensile Yield Strength (MPa)	**Ultimate Tensile Strength (MPa)**	**Tensile Failure Strain (%)**	**Tensile Young's Modulus (GPa)**	**Tensile Energy Absorption (MJ/m^3)**
Base SS-CMF	15.32	77.25	7.75	4.36	2.9
SS-CMF-CSP	91.66	165	22.9	8.26	20.0
Steel Hollow Sphere Foam (HSF)* (38)	3.30	5.35	2.75	3.1	0.15
Alporas Aluminum foam* (36, 37**)**	1.39	1.78	1.82	0.46	0.04

*The values are approximated from data presented in the respective publications

Table 5. Normalized mechanical properties for SS-CMF and SS-CMF-CSP tested under quasi-static tension . The values from other metal foams are presented for comparison.

	Normalized Ultimate Tensile Stress (MPa/(g/cm^3))	**Specific Tensile Energy Absorption (J/g)**
Base SS-CMF	24.14	0.95
SS-CMF-CSP	36.67	4.45
Steel Hollow Sphere Foam (HSF)* (38)	4.73	0.13
Alporas Aluminum Foam* (37)	5.93	0.13

*The values are approximated from data presented in the respective publications

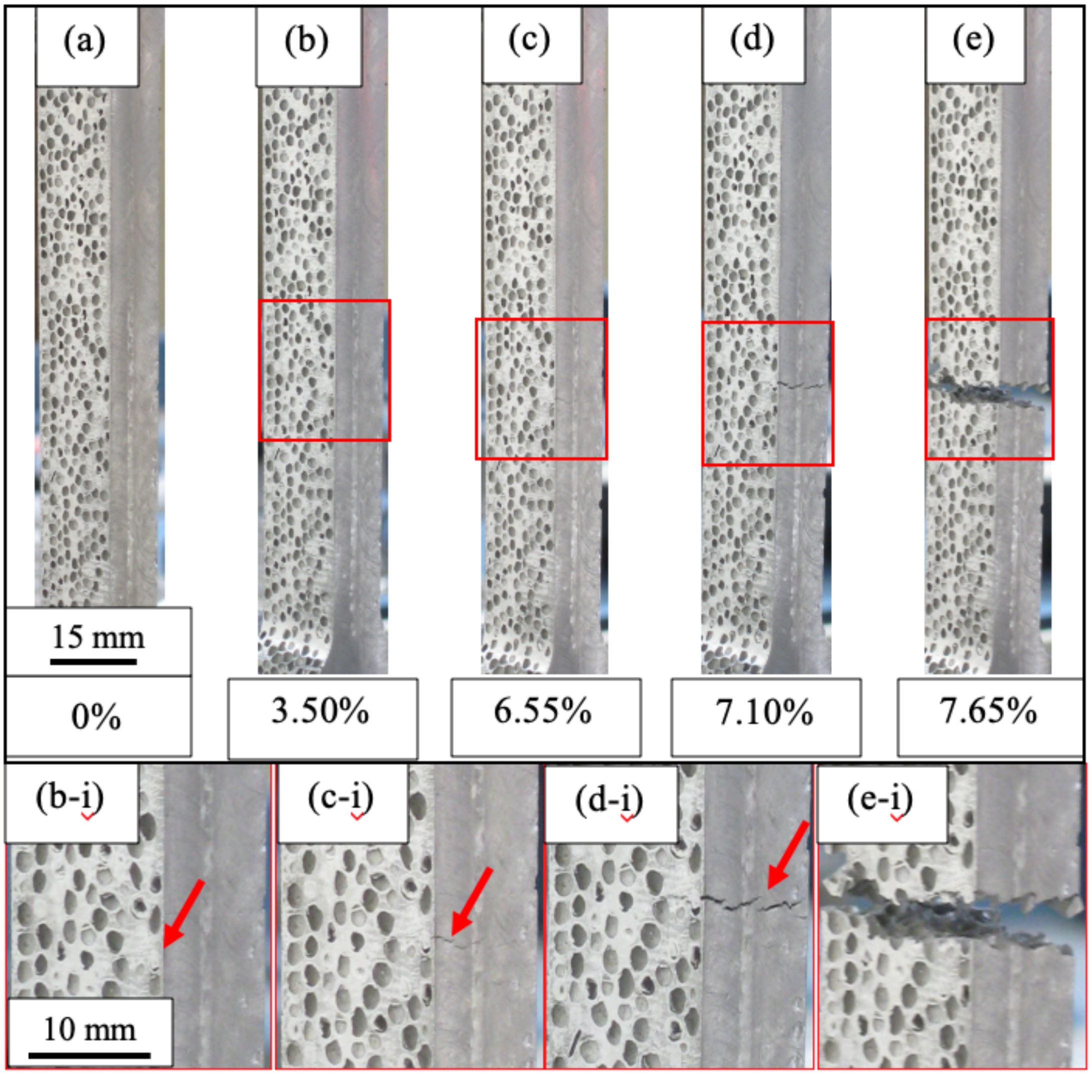

Figure 11. Digital images of SS-CMF sample under tension showing crack initiation and failure (a)-(e). Higher magnification images of the outlined areas are shown below in (b-i)-(e-i).

Images of the fractured surface are presented in Figure 12. The figure shows that the crack was able to maneuver through the micro-porosities of the matrix (shown in Figure 3(a) and (b)). It seems that the crack propagated mostly through the sphere walls rather than debonding of the spheres from the matrix, as can be seen in the digital fractography images in Figure 12 (b) and (c). Debonding of the spheres from the matrix was reported for SS-CMF under four-point bending (52). However, the fracture across the sphere alludes to a strong bond between the matrix and the sphere walls and indicates optimized processing of S-S CMF. Figure 12 (a) shows an additional fracture at the far side of the sample where the crack has moved through the sphere wall. There is one sphere that has been removed from the matrix and is highlighted in Figure 12 (b) as well as the corresponding dimple in Figure 12 (c). This sphere was pulled from the matrix, most likely due to a slight separation and a weak bond around the sphere similar to what was shown in the SEM image in Figure 3 (a).

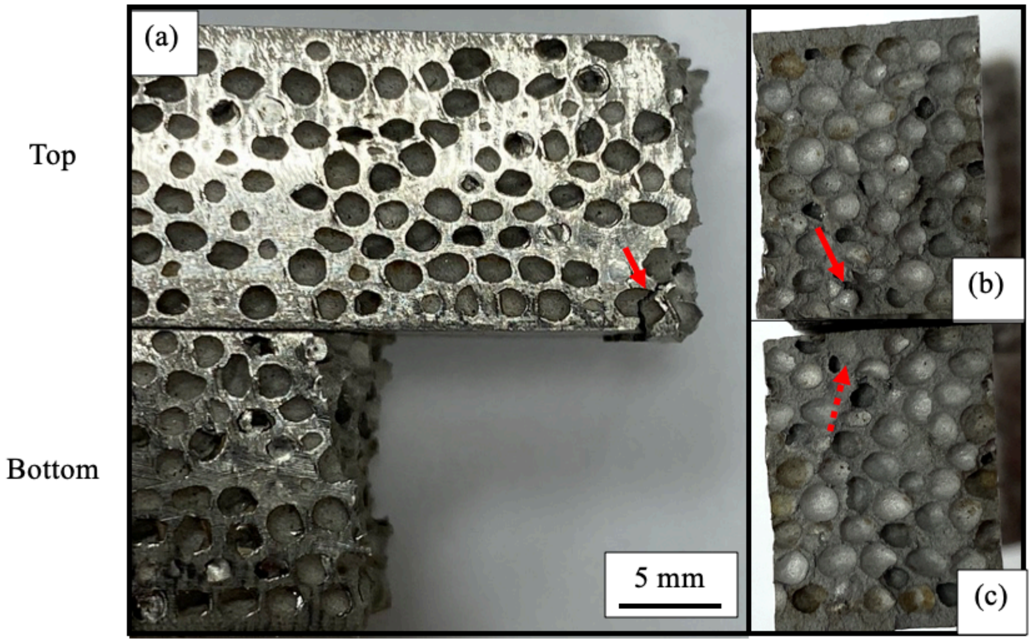

Figure 12. Digital images of the SS-CMF sample shown in Figure 11 after tensile failure. (a) The side of the sample and (b)-(c) the fractography images showing sphere walls tearing rather than debonding from the surface.

Images of another example SS-CMF sample is shown in (Figure 13). This sample has a similar failure mode, but with multiple cracks forming at different locations. Higher magnification images of the failure region outlined by the red boxes can be seen at the bottom of the figure. The primary crack formation can be seen in Figure 13 (b-i). Additional failure regions separate from the primary crack are seen forming in Figure 13 (d-i) and (e-i) on the opposite side of the sample. Failure and cracking across the sphere wall can be seen in Figure 13 (d-i) at multiple locations. Investigation of the failure surface in Figure 14(a)-(d) reveals a similar path of the crack through the sample thickness. The fracture surface in Figure 14 shows the broken spheres along the surface as well as additional cracks forming within the sample in Figure 14 (b) and (d). The sphere highlighted in Figure 14 (d) shows multiple cracks expanding through the sphere wall along the surface, as well as the secondary crack formation on the opposite face of the sample. The strong bond between the sphere walls and the matrix causes splitting of spheres under tension for the base SS-CMF.

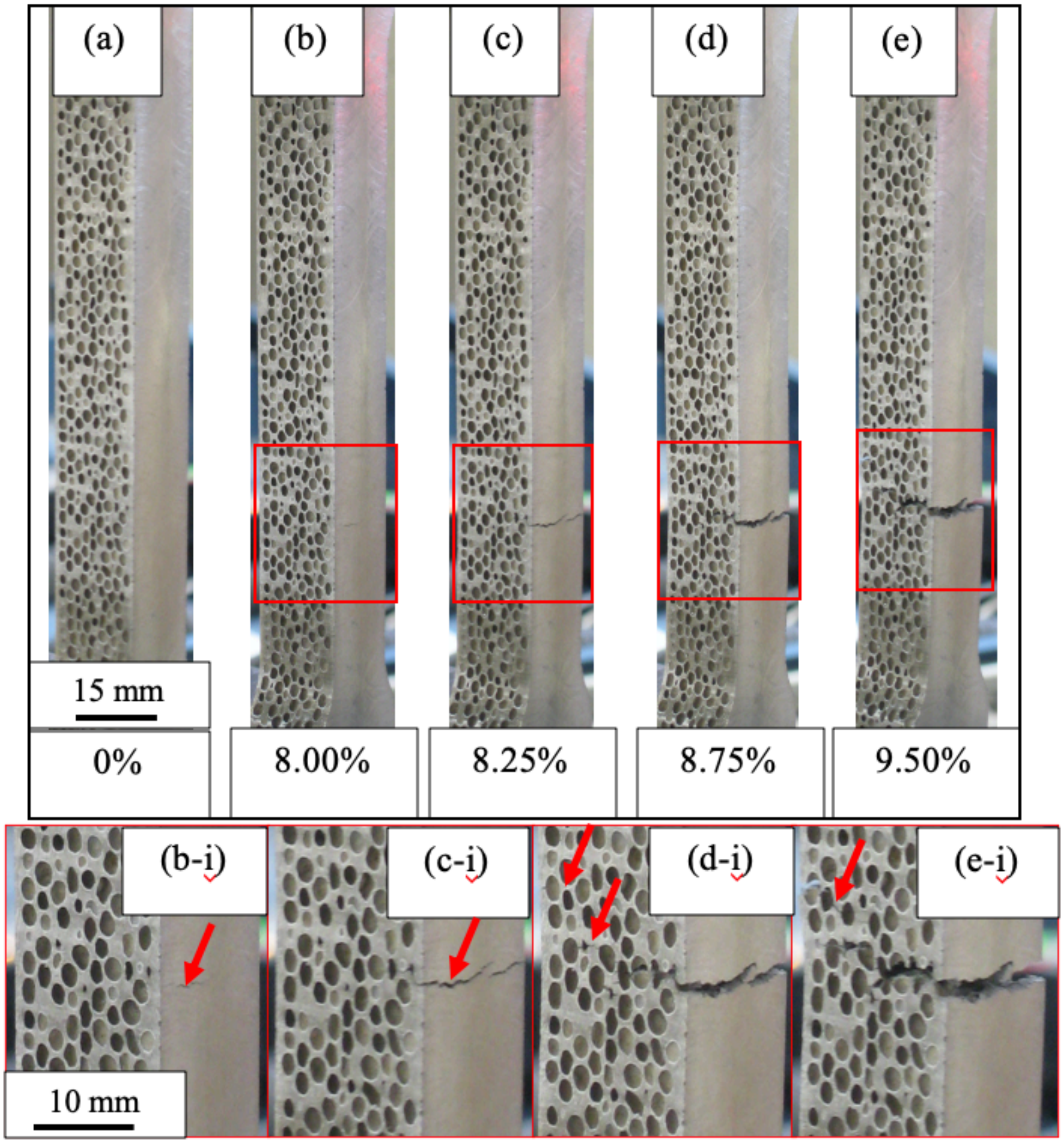

Figure 13. Digital images of a SS-CMF sample under tension with multiple cracks initiating about the same location near failure. The magnified images (b-i)-(e-i) showing crack evolution are highlighted in the respective images above.

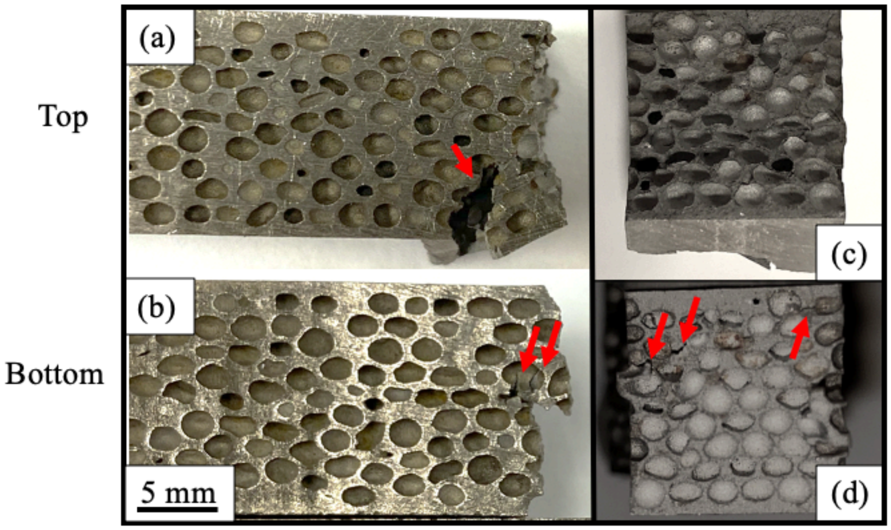

Figure 14. Digital images of the SS-CMF sample shown in Figure 13 with detailed information from the failure surfaces under tension. (a)-(b) the sides of the sample and (c)-(d) the fractography images showing failure across the sphere walls. The red arrows highlight the location of additional crack formations around the failure region.

Steel Composite Metal Foam Core Sandwich Panels Under Tension

The stress-strain curves resulted from tensile testing of SS-CMF-CSP are plotted in Figure 15(a). The stress and strain were calculated as a function of the initial total cross section of the sample, which includes the total thickness of the SS-CMF core and the two face sheets. Digital images taken of the sample during loading indicated that the SS-CMF core fails first while the face sheets continued to elongate further (Figure 16). As such, the first peak of the curve is associated with the failure of the SS-CMF core, followed by the plastic deformation and failure of the stainless steel face sheets at higher strains. These two regions are divided by a vertical dotted line in Figure 15(a). The measured mechanical properties of SS-CMF-CSP are also presented in Table 4 below those of the base SS-CMF properties. The sample had a yield similar to that experienced by the base SS-CMF between 3.5-4% strain followed by plastic deformation and failure. The yield, prior to core failure, is measured between 90-105 MPa. The ultimate tensile strength of the SS-CMF core increased from 77 MPa to 165 MPa, almost two times stronger than the base SS-CMF samples. The failure strain of the core also increases from just under 10% to 20-24% with higher energy absorbed prior to the failure of the core, not including the additional deformation of the face sheets. The face sheets support the core under tension without completely debonding from its surface. Two of the samples, with their stress-strain curve shown in red, have a very similar strength, whereas the sample represented by the blue solid lines experienced a lower core failure strength. The lower yield is attributed to the core failing near the fillet area and close to its radius of curvature due to stress concentrations at the fillet, whereas the other two samples have a very similar yield and failed at the center of the dogbone specimen.

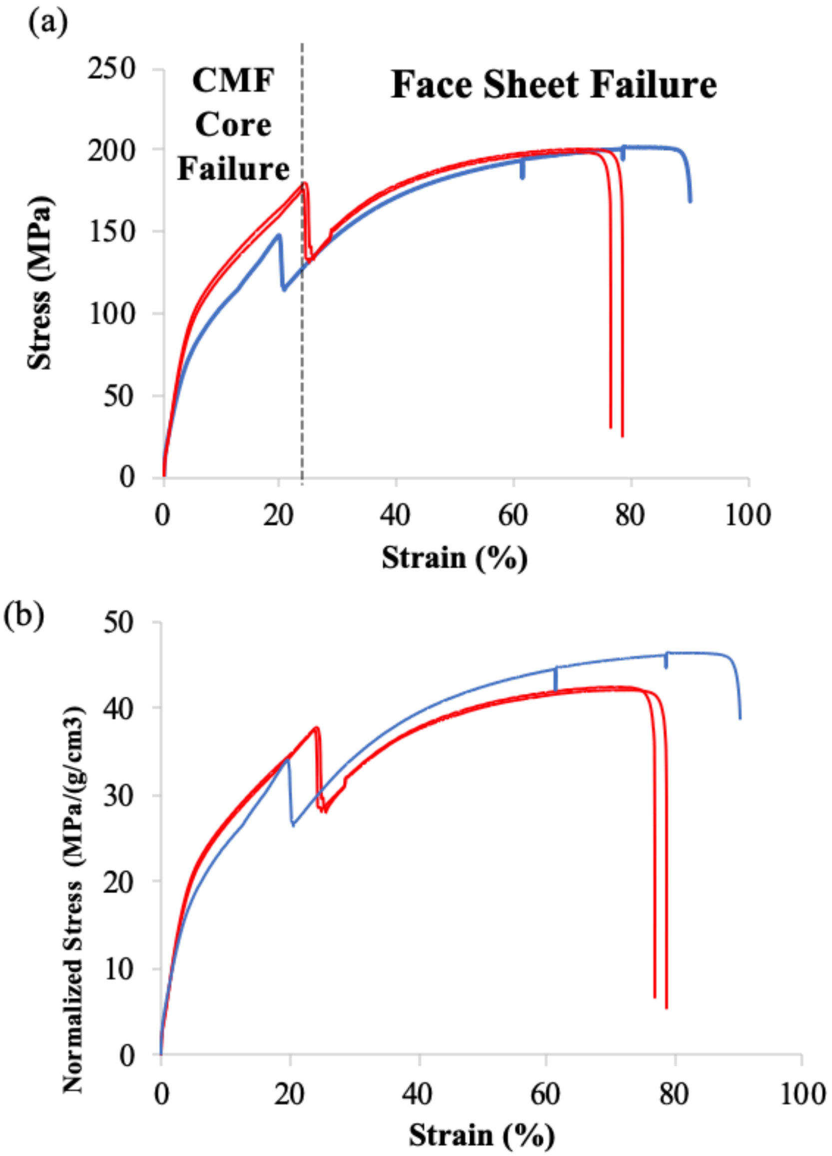

Figure 15. (a) Engineering tensile stress-strain curves of the SS-CMF-CSP samples, and (b) the stress strain curve normalized by the density of each SS-CMF-CSP sample The vertical dotted line divides the CMF core failure region (left) from the additional plastic straining and failure of the face sheets (right).

The normalized stress-strain curves are plotted in Figure 15(b). All of the SS-CMF-CSP samples have a similar normalized core failure stress between 35-40 MPa/(g/cm3). The average specific energy absorption of the sandwich panels under tension up to the core failure was measured as 4.45 J/g. This is more than four times higher than the base SS-CMF panels. The support of the stainless steel face sheets delayed the crack initiation of the core material and improves its average normalized values and specific energy absorption, which are listed in Table 5. The cores of the SS-CMF-CSP's have a normalized failure stress 52% higher than the base SS-CMF samples as well as an increased lifetime up to 20% strain to failure, more than double that of the base samples.

As can be seen in Figure 16 the diffusion bond between the core and the face sheet maintains its integrity up to the core failure but undergoes slight debonding just outside the grip area at 16% strain (Figure 16-b). Debonding does not spread until after crack initiation in the sample and complete core failure as seen in Figure 16(c)-(e). Unlike the base SS-CMF samples, failure of the SS-CMF-CSP initiates from within the core's thickness, as can be seen in the highlighted regions at the bottom of the figure. The face sheets lend enough support to delay the core's onset of failure until the crack starts from the center of the core and moves towards the surface, as seen in Figure 16 (c-i). The crack can be seen forming at the edge of a sphere wall within the center of the core. The crack initiation is most likely due to coalescence of the micro-porosities that exist in the matrix, similar to that of the base SS-CMF. The crack then grows towards the surface causing further debonding of the face sheets from the SS-CMF core around the gripped section and at the center of the sample in Figure 16 (d). Following core failure, the stainless steel face sheets yield up to fracture. Face sheet failure are shown in Figure 16 (f) and (g) with increased debonding highlighted by the red arrows. The failed sample in Figure 16 (g) shows necking of the face sheets at the point of failure. It shows that the diffusion bond creates a strong enough interface between the core and face sheets to promote strengthening of the core without limiting the deformation of the face sheets at higher strains. The overall strength of SS-CMF core sandwich panels can be further optimized in future testing in order to achieve the desired strength/weight ratio for specific applications.

Digital fractography images of one of SS-CMF-CSP samples is shown in Figure 17. The SS-CMF-CSP's fracture surface is different from that of base SS-CMF samples and shows debonding of the sphere walls from the matrix. The percentage of sphere wall separation from the matrix in S-S CMF-CSP is much more than that in base SS-CMF, as can be seen in Figure 17(a) and (b). The debonded spheres are highlighted by solid red arrows and their corresponding dimples are pointed to by dotted arrows in Figure 17(a) and (b). The debonding of the sphere walls from the matrix occurred similarly in all SS-CMF-CSP due to the heat cycle of diffusion bonding of face sheet process. The heat cycle causes grain growth within the sphere wall, as seen in the SEM images in Figure 3. This will increase the ductility of the spheres when compared to the base SS-CMF. Moreover, the heat cycle allows for diffusion of elements between the sphere walls and the surrounding matrix. During the diffusion bonding process, due to the higher carbon content in the sphere walls, carbon diffuses out from the sphere wall into the surrounding matrix. This allows for additional carbide formations within the matrix and along the matrix interface with the sphere wall. The carbides create a more brittle bond with the sphere walls. This brittle interface, in conjunction with improved ductility within the sphere walls, causes debonding of the sphere walls from the matrix in some locations of the SS-CMF-

CSP during tensile test resulting in a mixed failure mode seen in SS-CMF-CSP samples (Figure 17) instead of spheres failure mode seen in base S-S CMF.

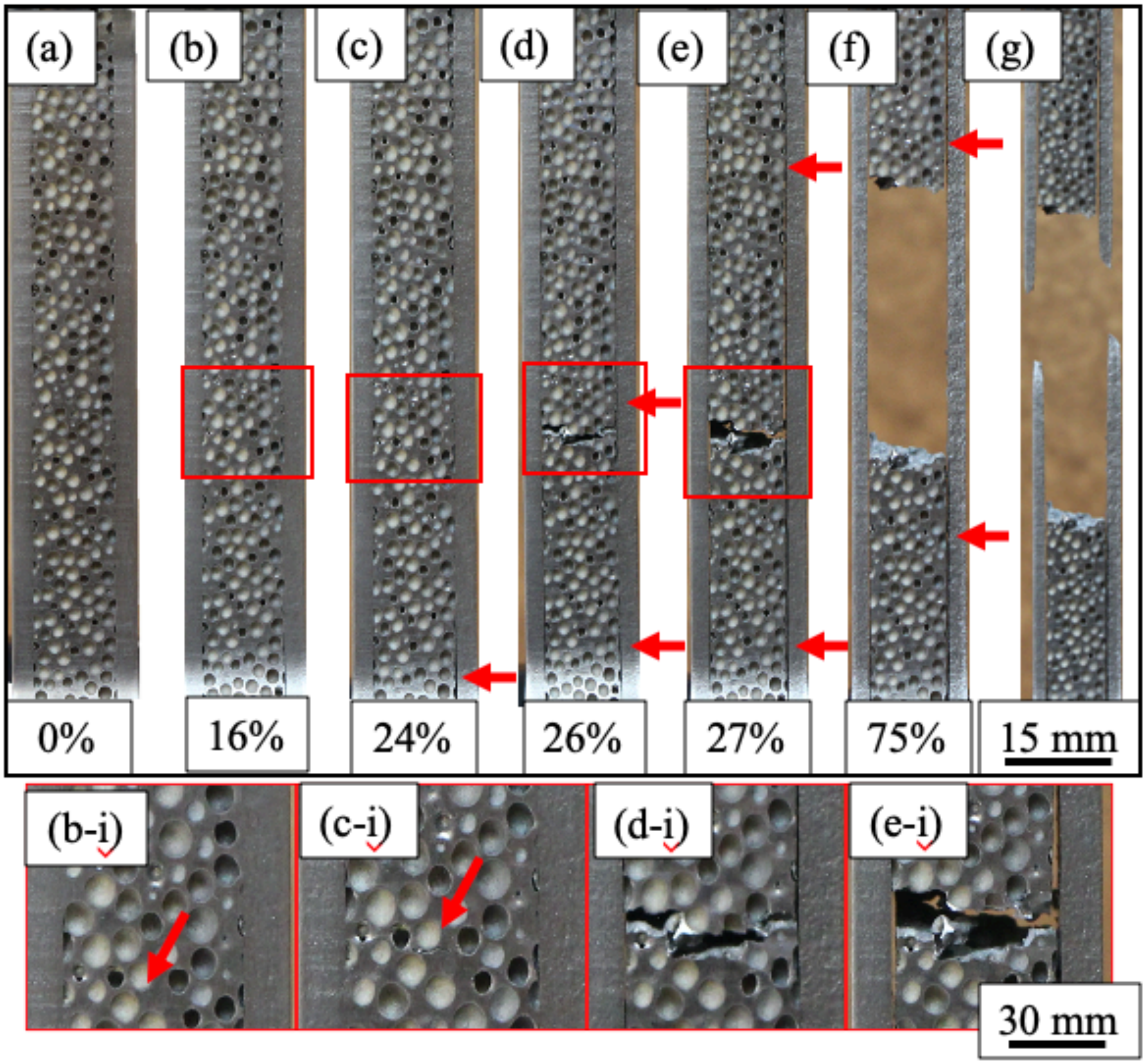

Figure 16. Digital images of an example SS-CMF-CSP under tension. Higher magnification images of the respective strains are shown at the bottom of the figure. The sample was imaged (a) prior to loading, (b) slight debonding occurred just prior to major deformation, and (c) crack initiation at the center of the sample. (d)-(e) Crack growth in the core leads to failure (f) with further debonding and face sheet yielding until (g) failure of the face sheets. The magnified images (b-i)-(e-i) showing crack evolution are highlighted in the respective images above.

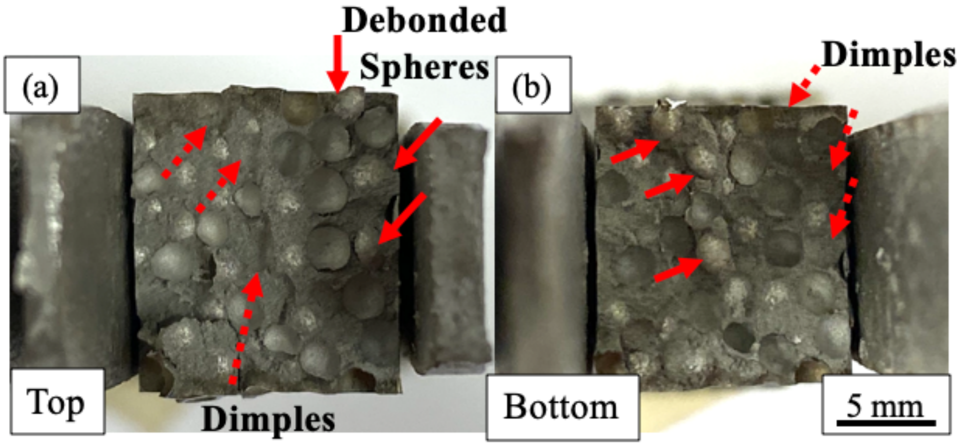

Figure 17. Fracture surfaces of the SS-CMF-CSP sample imaged in Figure 16 with a mixed mode failure when compared to the base S-S CMF. The sample fractures by tearing some sphere walls, while some other spheres are detached from the matrix highlighted by red arrows. Removed spheres are shown by the solid arrows and their corresponding dimples by dotted arrows can be seen in (a) top and (b) bottom fracture surfaces.

6.5 Analytical Approximation

Rule of Mixtures

The rule of mixtures can be used to approximate the properties of SS-CMF by proportionally combining the properties of the hollow stainless steel spheres and sintered 316L stainless steel matrix. The volume fraction of the hollow spheres and matrix have been previously measured as 59% and 41% respectively given the random-loose packed arrangement of the hollow metal spheres within the SS-CMF structure (53). The Young's modulus of closed-cell hollow sphere foam (HSF) that makes up the macro-porous structure inside the SS-CMF has previously been approximated as 2.047 GPa (54). This value is relatively close to what has been found experimentally for hollow sphere foams made with a variety of steels (39, 55). As for the matrix, Falkowska and Seweryn have reported the elastic modulus of sintered 316L stainless steel under tension (56). The tap density of the SS-CMF matrix has previously been measured as 4.25 g/cm3, which is equivalent to a porosity percentage of approximately 46% (53). The measured modulus of 316L sintered stainless steel with a porosity of 41% was reported as 32.9 GPa and was used for calculation of the SS-CMF modulus. The rule of mixtures gives the elastic modulus of SS-CMF as:

$$
\begin{gathered}
\mathrm{E_{SS-CMF}} = [\mathrm{V_{HSF}} \times \mathrm{E_{HSF}}] + [\mathrm{V_M} \times \mathrm{E_M}] \qquad (5\text{-}1) \\
\mathrm{E_{SS-CMF}} = [0.59 \times 2.047] + [0.41 \times 32.9] \\
\mathrm{E_{SS-CMF}} = 14.74\ \mathrm{GPa\ (upper\ bound)}
\end{gathered}
$$

where V_{HSF} and V_M are the volume fraction of the hollow spheres and matrix, respectively. E_{HSF} and E_M are the values used as the Young's modulus inputs for the spheres and matrix. Eq. (5-1) gives the upper bound of the rule of mixtures while the inverse rule of mixtures is used to evaluate the lower bound values as:

$$E_{SS-CMF} = \left[\frac{V_{HSF}}{E_{HSF}} + \frac{V_M}{E_M}\right]^{-1} \tag{5-2}$$

$$E_{SS-CMF} = \left[\frac{0.59}{2.047} + \frac{0.41}{32.9}\right]^{-1}$$

$$E_{SS-CMF} = 3.33 \text{ GPa (lower bound)}$$

The experimentally measured modulus of elasticity of the base CMF samples under tension was 4.36 GPa. This falls between the upper and lower bounds values calculated using the rule of mixtures. It is notable that the model does not count for the strong bonding between the sphere wall and the matrix in S-S CMF and is the most simplistic approach for predicting the mechanical properties of a complex material such as composite metal foam. A detailed model that considers all constituents of the material including hollow metal spheres, metallic matrix, air inside the spheres, and air in the micro-porosities of the sphere walls and matrix is necessary to predict the exact properties of composite metal foams under variety of loading conditions.

6.6 Conclusion

SS-CMF core sandwich panels were manufactured by solid state diffusion bonding of a SS-CMF core panel into two stainless steel face sheets. The mechanical properties of SS-CMF and SS-CMF-CSP were explored through quasi-static tensile testing. The base SS-CMF samples had an ultimate tensile strength between 75-85 MPa and a failure strain between 7.5-8%. The normalized tensile strength was approximately 24 MPa/(g/cm3), more than five times that of any comparable metal foam. The addition of face sheets further improved the performance of SS-CMF core under tension. The ultimate tensile strength of the SS-CMF-CSP was more than twice that of the base samples at 165MPa with an average failure strain of 23%. The normalized strength of the SS-CMF-CSP was 52% higher than the base SS-CMF and absorbed more than four times the energy to failure during loading.

Digital image analysis of the SS-CMF samples under tension showed the crack initiating within the matrix, primarily due to the coalescence of micro-porosities. Surface fractography of the samples reveal failure across the sphere walls as the crack progressed through the sample thickness for the base SS-CMF samples. The SS-CMF-CSP had a mixed mode of failure with multiple spheres debonding from the matrix across the fracture surface. Debonding of the spheres is caused by additional carbide formation around the sphere walls due to the diffusion of carbon from the sphere walls into the surrounding matrix during the heating cycle for manufacturing sandwich panels. The sphere walls stiffen under tension and cause the crack to grow around them rather than through the sphere wall itself.

The elastic modulus of the base SS-CMF and SS-CMF-CSP were approximated using the rule of mixtures. The rule of mixtures gives a simple approximation for the Young's modulus with the measured values of both the SS-CMF and the SS-CMF-CSP being between the approximated lower and upper bound. A detailed model that considers all constituents of the material including hollow metal spheres, metallic matrix, air inside the spheres, and air in the micro-porosities of the sphere walls and matrix is necessary to predict the exact properties of composite metal foams under variety of loading conditions.

The face sheets on the SS-CMF-CSP not only improve the performance of the SS-CMF core in tension, but also provide a non-porous surface that can protect against corrosion and be used in a variety of engineering applications.

7 Puncture Resistance of Composite Metal Foam Core Sandwich Panels

7.1 Abstract

The stainless-steel composite metal foam (SS-CMF) core sandwich panels (SS-CMF-CSP) were manufactured by attaching stainless steel face sheets to SS-CMF core using either solid-state diffusion bonding or adhesion bonding. The performance of the sandwich panels was experimentally evaluated using a 0.50 caliber Mann gun barrel, modified to fire 2.54 and 3.175 cm diameter steel ball bearings. Upon firing the 0.50 caliber cartridge, the expanding gas pressure ejects the steel ball creating a large kinetic energy on the steel ball to puncture through the SS-CMF sandwich panel target. The projectile energy was gradually increased by increasing the amount of gunpowder used as well as the size of the steel ball. In the first round of experiments, the kinetic energy of the 2.54 cm steel ball upon arriving at the target (2300 to 4300 Joules) was not enough to create a complete penetration through any of the panels. The Mann gun barrel was then modified to fire a 3.175 cm steel ball bearing, which almost doubled the mass of the steel ball. The quantity of the gunpowder was also maximized to create the largest amount of puncture energy. The higher velocities of the larger steel ball created kinetic puncture energies from 10,445 to 14,500 Joules in the second round of experiments. But, no compete penetrations through any of the SS-CMF sandwich panels of 30 x 30 cm dimensions and 6.8 Kg to 11.7 Kg areal densities was achieved. The results indicate the effectiveness of composite metal foams in absorbing the puncture energy of an impactor. It is notable that these experiments were restricted to relatively small-scale samples, no larger than 30x30 cm dimensions. Full-scale tank-car puncture testing is necessary for a complete evaluation of the performance of composite metal foam and its sandwich panels to protect tank-cars transporting hazardous materials.

7.2 Puncture Test Setup

7.2.1. Quasi-static puncture Setup

First attempt in conducting puncture tests on Composite Metal Foam core sandwich panels included the use of a quasi-static puncture test setup in an MTS 810 universal testing machine equipped with a 220 kips load cell. SS-CMF-CSP testing panels were placed on top of a 40 x 40 cm rigid steel base reaction plate with a 10 cm diameter circular central hole and centered with regards to the plate and indenter. The indenter was supported in the top grip and the testing panel was supported on the rigid steel base reaction plate at the bottom. Two different indenters / or punchers of 5 cm and 3.75 cm diameter both with a hemispherical nose were used to punch through the testing panels (Figure 18). A displacement control loading was selected and the loading was continued until a full penetration through the entire thickness of the panel is achieved. The load and displacement were recorded by a computer connected to the frame's load cell to be used to create the related energy absorption curves. However, a number of issues with this approach resulted in discontinuing the use of this technique and designing a new test method for evaluating the puncture performance of SS-CMF-CSPs. Those issue are including:

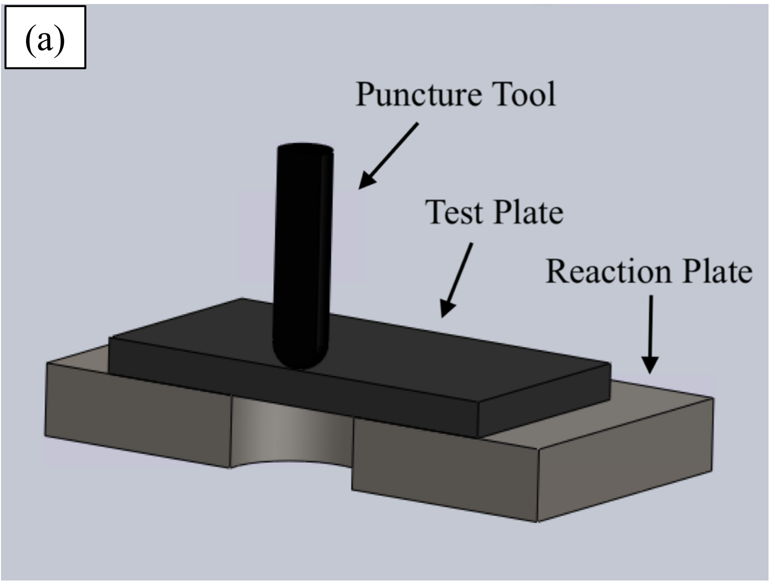

Figure 18. (a) Solid Work design of the puncture test set up for quasi-static loading and (b) bottom deformed puncture tool under loading.

1. The puncture tool itself is deformed while puncturing through the panel absorbing large amount of energy, making it difficult to identify the energy absorbed by the panel itself (Figure 18). As such the generated data was not reliable.
2. The clearance between the puncture tool and manhole in reaction plate needed to be adjusted for panels with various thicknesses in order to be able to compare the results. This means for each panel thickness; a different puncture tool will be needed.
3. A tank-car puncture resulted from a rail accident is always associated with high speed impact even when it is traveling at lowest speed limits. As such, the quasi-static puncture cannot accurately mimic a real puncture scenario.

As such a new method for puncture testing of the panels was designed that could be used for variety of panel thicknesses without the need for changing the test set up and could generate reliable and repeatable data that mimic the tank-car accident scenarios.

7.2.2. High Speed Puncture Setup

The Code of Federal Regulations outlines the procedures for testing the survivability of tank-car-head puncture-resistance systems for coupler-to-head impacts (57). Railroad tank-cars must be able to withstand a 29 km/hour (18 mph) coupler to head impact from a ram car weighing 119.3 ton (263,000 lb.) (57). Unfortunately, conducting such full-scale puncture tests are quite expensive (58). As a result, a small-scale experimental test is designed and utilized to evaluate the puncture resistant of composite metal foam core sandwich panels. The experiment is designed to use a 0.50 caliber Mann gun barrel, modified by attaching a heavy walled steel cannon barrel at its front end with a non-rifled 2.54 cm bore to accommodate firing steel ball bearings of 2.54 cm diameter at varying velocities to generate a large kinetic puncture energy on the ball arriving at the SS-CMF core sandwich panels and mimic full-scale puncture tests. This experiment was conducted at the Technology Development Directorate – Aviation Technology (TDD-AV) at Fort Eustis.

Figure 19-a shows the Mann gun barrel that was modified for shooting the steel balls. Figure 19-b shows one of the steel balls used in this investigation. The ballistic “Mann” type gun was mounted on a rigid frame with cannon barrel threaded on to its front end. A laser bore sight was installed on the cannon barrel to locate the ballistic impact point. Each SS-CMF-CSP target was rigidly clamped to a rigid steel support during the test using two aluminum wide flange beams and a number of C-clamps and targeted for impact at its center of mass. The distance from the muzzle to the target was approximately seven 7 meters (~23 feet). All panels were mounted in a similar fashion. The projectiles were targeted with 0° of obliquity in reference to the target face. Figure 20 shows the test article configuration.

In each test, a fully assembled 0.50 caliber cartridge case was disassembled (projectile removed), the gun powder was removed, and reloaded with a measured amount of gunpowder required to obtain a predetermined velocity. The projectile was not reinserted in the cartridge case so a small amount of cotton wadding was used to hold the gunpowder in the case, on top of the gun powder, before the cartridge case was chambered for firing. For the most part, the velocity of the projectile was increased for each subsequent test. The intent was to impart an increased amount of projectile energy into each test article until a complete penetration through the panel was achieved.

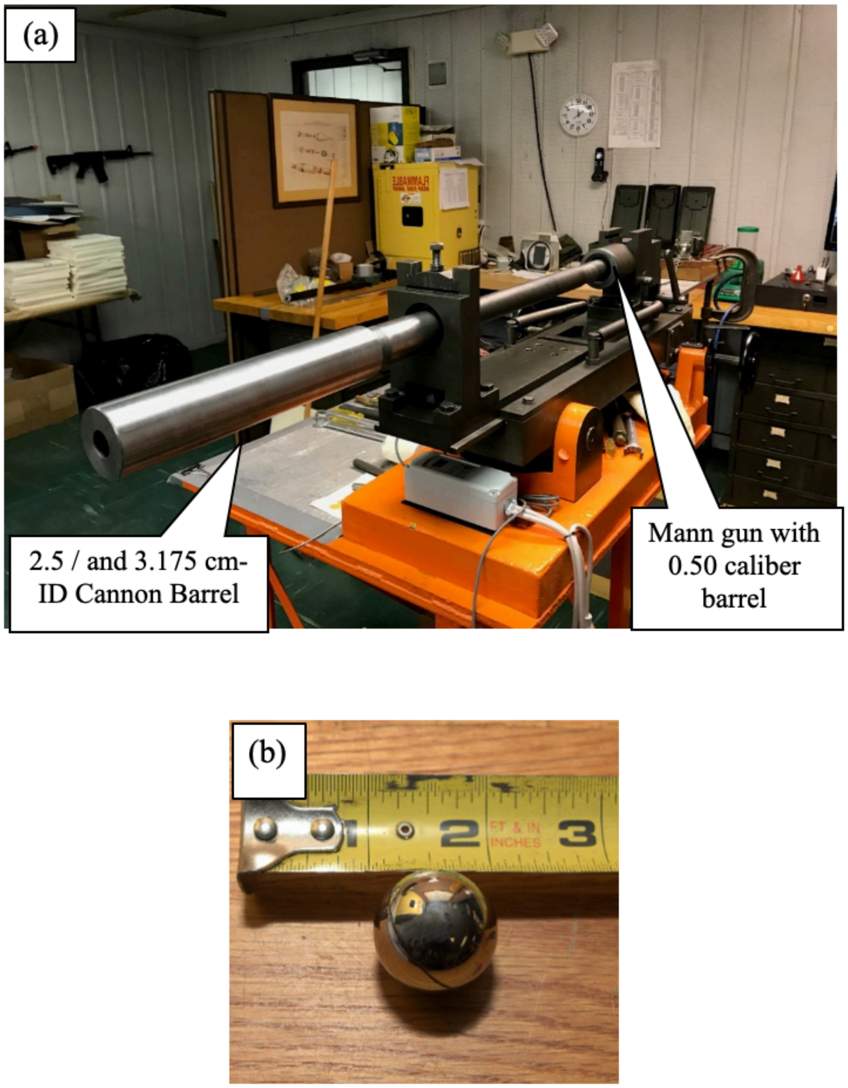

Figure 19. (a) Modified 0.50 caliber Mann gun configuration for shooting 2.54 and 3.175 cm steel ball; (b) One of the 2.54 cm Steel Balls used for Testing.

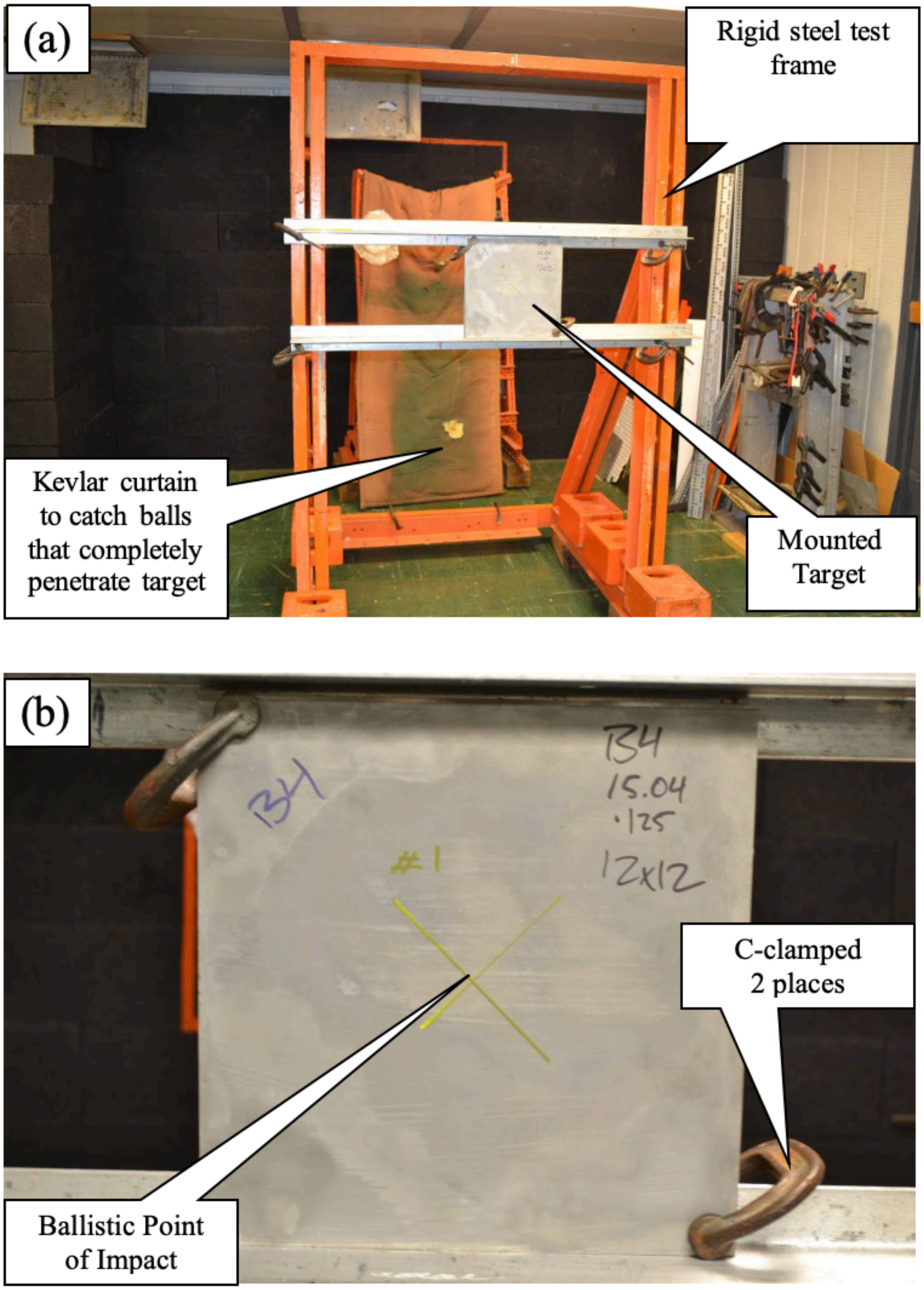

Figure 20. (a) target mounting configuration showing the rigid steel test frame and a SS-CMF sandwich panel target mounted; (b) Close up of the SS-CMF sandwich panel target mounted on the rigid steel frame using C- clamps

The steel ball was inserted and then packed into the modified cannon barrel prior to chambering the cartridge case into the Mann gun breach. Each cartridge case was fired remotely using the range's gunfire control system. The expanding gasses from the burning gun powder propelled the steel ball down range, striking the intended target. Multiple calibration test shots were conducted to establish the correct projectile velocity before the test articles were mounted and impacted. After each ballistic test, the result of the impact was recorded and the panel was either removed or repositioned for the next impact.

An Oehler Type 57 velocity chronograph, consisting of three infrared screens and tape readout, was placed in the shot line in front of the target to record the pre-impact projectile velocity. A photograph showing the velocity chronograph and test fixture, located in front of the Mann gun, is shown in Figure 21-a. Note that the velocity chronograph was further moved towards the target in order to read the final velocity of the steel ball at the time of impact.

Additionally, a digital high-speed camera was positioned facing perpendicular to the shot line, immediately in front of the target (Figure 21-b). This camera was used to record the path of the steel ball just prior to impact. After each ballistic event, the high-speed video was reviewed and the frames showing the steel ball traveling just prior to striking the target were used to determine the velocity of the ball at impact. The velocity or "rate of displacement" was determined by using known values such as the steel ball diameter and the video capture frame rate. Each calculation was repeated several times for each ballistic event and the average velocity was used in the data analysis. The high-speed video was used to confirm the velocity readouts from the velocity chronograph. In all cases, the velocity measured by the chronograph agreed well (±25 fps) with the velocity calculated using high speed video.

Table 6 shows the weight and dimensions of all panels used in the first set of experiments and the specification of various components of each panel.

After a series of experiments conducted using the 2.54 cm steel balls and noting that none of the steel balls could penetrate through the SS-CMF core sandwich panels, a second set of experiments was designed in which the cannon barrel was modified to fire 3.175 cm (1.25 inch) steel balls. This way the mass of the ball was doubled to offer a higher kinetic energy. In addition, through the use of different gun powder, the kinetic energy was further increased to near 14500 joules.

In the second round of tests, seven ballistic tests were conducted against six different targets of SS-CMF core sandwich panels. Table 7 shows the dimension of various components of all panels used in the second set of experiment along with their weight. The thickness of the CMF and the face sheets were varied to achieve a variety of target areal densities.

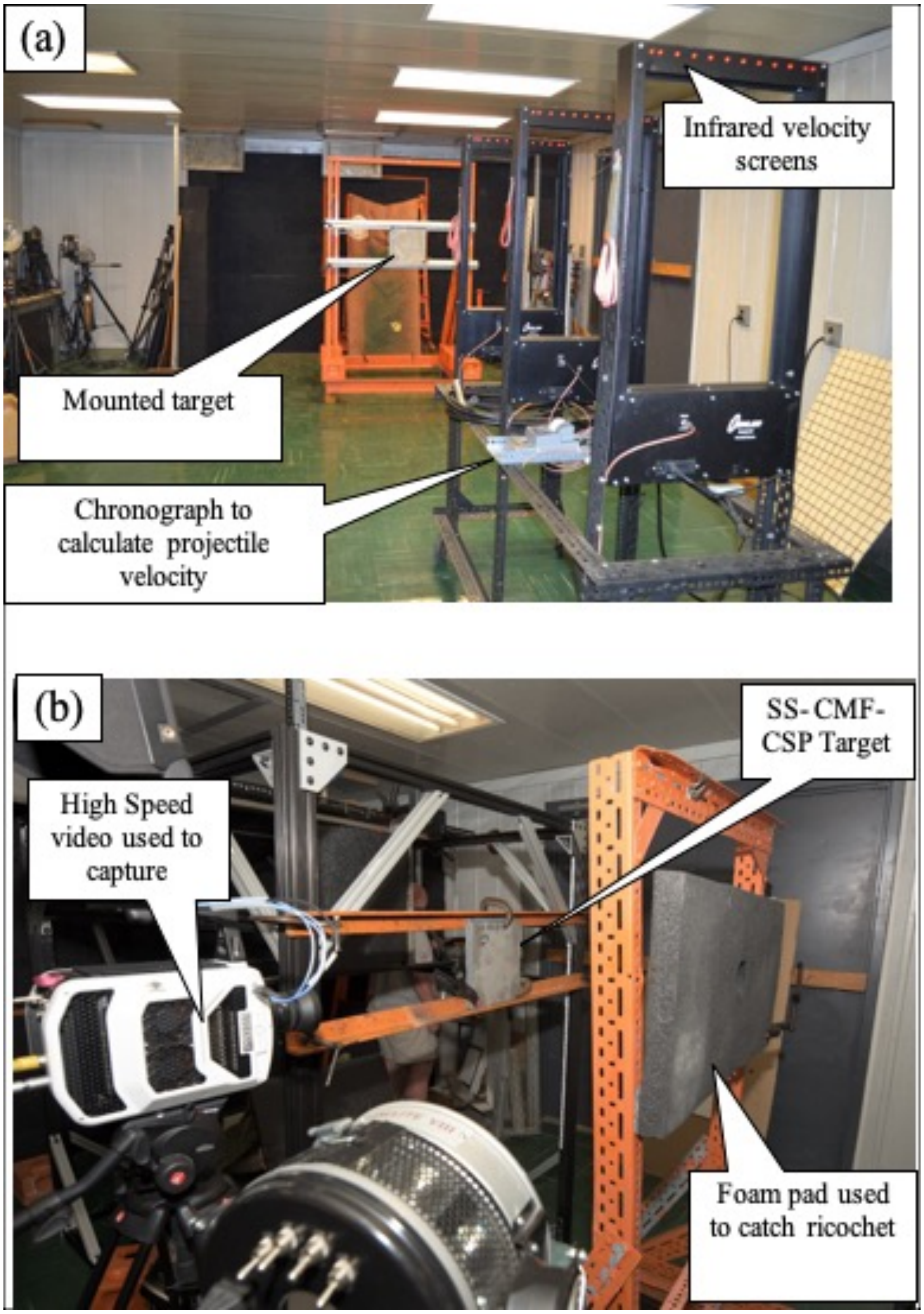

Figure 21. (a) View of indoor range showing velocity chronograph and test fixture; (b) Testing configuration showing the position of high speed camera, SS-CMF sandwich panel target, and a foam pad used to catch potential ricochet steel ball;

Table 6. SS-CMF core sandwich panels tested in the first round of experiment using 2.54 cm steel balls along with each panel's dimensions, total weight and equivalent weight of a 30x30 cm panel as a representative of the areal density of each panel.

Test #	Panel #	Panel Length (cm)	Panel Width (cm)	SS-CMF Thick -ness (cm)	SS-CMF Mass (g)	SS-CMF Density (g/cm^3)	Face Sheet Thick-ness, (cm)	Total Weight of Sandwich (Kg)	Equivalent Weight of 30x30 cm Sandwich (Kg)
1	75B Adhesive	25.65	25.60	1.79	3255	2.77	0.3175	6.41	8.78
2	75B Adhesive	25.65	25.60	1.79	3255	2.77	0.3175	6.41	8.78
3	75B Adhesive	25.65	25.60	1.79	3255	2.77	0.3175	6.41	8.78
4	75B Adhesive	25.65	25.60	1.79	3255	2.77	0.3175	6.41	8.78
5	12D Diffusion	30.42	30.38	1.59	3925	2.68	0.3175	8.22	8.00
6	12B Diffusion	30.45	30.38	2.03	4325	2.30	0.3175	8.75	8.51
7	12C Diffusion	30.39	30.40	2.29	5780	2.74	0.3175	10.14	9.87
8	1A Diffusion	25.59	25.59	2.43	4365	2.75	0.3175	7.41	10.18
9	B3 Diffusion	30.20	30.30	0.92	2165	2.57	0.635	10.82	10.64
10	Odd B Adhesive	24.77	25.24	2.08	2160	2.4	0.3175	5.40	7.77

Table 7. SS-CMF core sandwich panels tested in the second round of experiment using 3.175 cm steel balls along with each panel's dimensions, total weight and equivalent weight of a 30x30 cm panel as a representative of the areal density of each panel (all SS-CMF core panels are diffusion bonded to their face sheets).

Test #	Panel #	Panel Length (cm)	Panel Width (cm)	SS-CMF Thickness (cm)	SS-CMF Mass (g)	SS-CMF Density (g/cm^3)	Face Sheet Thickness, (cm)	Total Weight of Sandwich (Kg)	Equivalent Weight of 30x30 cm Sandwich, (Kg)
1; 2nd round	B4 First Shot	30.15	30.30	0.93	2330	2.74	0.3175	6.82	6.72
2; 2nd round	7A2-18	25.73	25.78	0.96	2080	3.27	0.3175	5.15	6.98
3; 2nd round	B4 2ND Shot	30.15	30.30	0.93	2330	2.74	0.3175	6.83	6.72
4; 2nd round	B1	30.23	30.35	0.99	2195	2.41	0.635	11.52	11.30
5; 2nd round	44A	25.35	25.55	1.03	2120	3.18	0.635	8.21	11.40
6; 2nd round	12G top	30.40	30.99	1.06	2685	2.70	0.635	11.79	11.27
7; 2nd round	12F	30.78	30.35	1.33	3080	2.47	0.635	12.17	11.73

7.3 Result and discussion

Round 1 of experiments with lower impact energy

Ten test shots were fired against six SS-CMF sandwich panel targets in the first round of this study with two sandwich panels bonded together using adhesive bonding and other four using diffusion bonding. All panels were made with SS-CMF cores of about 2.3- 2.7 g/cc density and 0.3175 cm stainless steel face sheets except one panel (B3 or test 9) with a thicker face sheet of 0.635 cm.

Table 8. Summary of the steel ball velocities, their associated energies , and the performance of SS-CMF-CSPs in the first round of experiment using 2.54 cm steel balls

Test #	Panel #	Steel ball velocity, m/s	Energy of steel ball, Joules (ft.lb)	Notes
1	75B Adhesive	122	488 (360)	Ball bounced back, no face tearing, no debonding, no back indentation
2	75B Adhesive	191	1192 (879)	Ball bounced back, no face tearing, no debonding, no back indentation
3	75B Adhesive	226	1677 (1237)	Ball bounced back, no face tearing, no debonding, small back indentation
4	75B Adhesive	270	2398 (1768)	Ball bounced back, no face tearing, front face sheet debonding, small back indentation
5	12D Diffusion	266	2319 (1710)	Ball fused, no face tearing, no debonding, small back indentation
6	12B Diffusion	287	2692 (1986)	Ball fused, front face tearing, back face partial debonding, small back indentation
7	12C Diffusion	321	3388 (2499)	Ball fused, front face tearing, back face partial debonding, small back indentation
8	1A Diffusion	362	4293 (3166)	Ball fused, front face tearing, back face partial debonding, small back indentation
9	B3 Diffusion	360	4244 (3129)	Ball fused, no front face tearing, no back face debonding, small back indentation, entire panel bent
10	Odd B Adhesive	322	3390 (2500)	Ball fused, front face tearing, back face complete debonding, small back indentation

Table 8 shows the velocities of the steel balls and their kinetic energy at the point of impact for all 10 experiments.

The first four tests started with lower velocities of steel balls all against one panel (panel 75B). The velocity of the ball was gradually increased from one shot to the next in an attempt to reach to a point where the ball could have a complete penetration into the panel. However, none of these four projectile impacts resulted in a complete penetration through the panel and all of them bounced back from the surface under the reaction forces resulted from the impact. The resulting kinetic energy of each ball at the point of impact was calculated using its mass and velocity and are tabulated in *Table 8*. The highest puncture energy was achieved on the fourth shot with a 270 m/s velocity of the projectile (steel ball) resulting in 2398 joules kinetic energy. Figure 22 shows the front (a) and back (b) of panel 75B after all four shots. As can be seen very minimal deformation is observed on the back of the panel indicating the need for higher energy of the ball to penetrate through the panel. As such, more gun powder was used to increase the velocity of the steel ball and its related kinetic energy in the forthcoming shots. It is worth mentioning that upon the fourth shot the adhesive bonding between the SS-CMF core and the front face sheet was started to separate as can be seen in Figure 22-c.

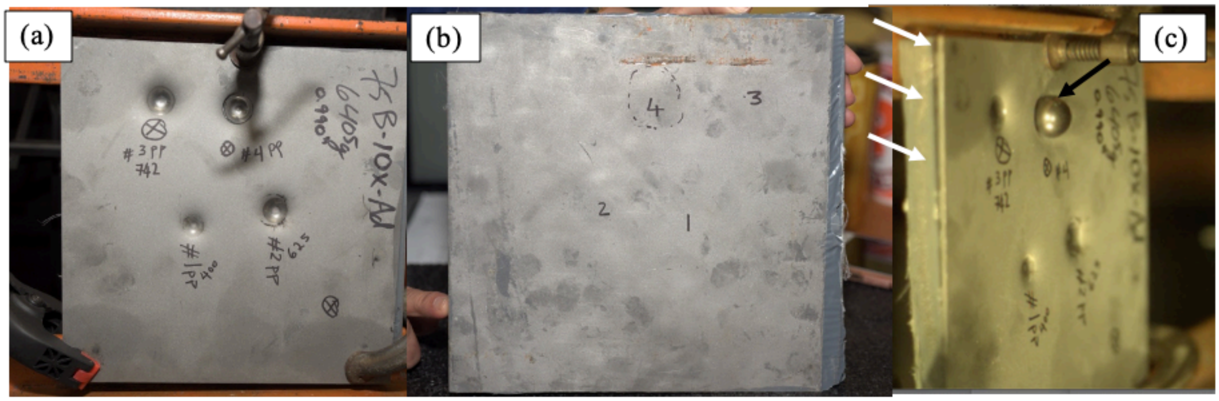

Figure 22. Digital images of a) Strike face and b) the back face of the panel used in test #1- 4 with 4 shots all bounced back from the panel. C) Screen shot of the high-speed video showing the steel ball #4 arriving at the surface of the panel causing separation between the top face sheet and SS-CMF core marked by white arrow.

It is also notable that while both adhesively bonded panels (test 4 and 10) delaminated upon high speed impacts of the projectile, most diffusion bonded panels could survive delamination, particularly at lower impact velocities. Upon steel ball impact, the panel undergoes distributed tensile forces on the back face and compressive forces on the front panel with shear stresses at the interface of the face sheets and SS-CMF core. Such shear stresses at the interface were not well accommodated by the high stiffness epoxy bond layer of panel 75B, particularly on its fourth shot (with higher energy of the ball) causing the face sheet to be separated from the core. But the diffusion bond layer with a uniform stiffness of the bond layer and the SS-CMF core, could accommodate shear stresses associated to the impact of the panel. Figure 22-c shows the steel ball at the point of bouncing back from the surface (black arrow) with separation between the front face sheet and SS-CMF core (marked with white arrows).

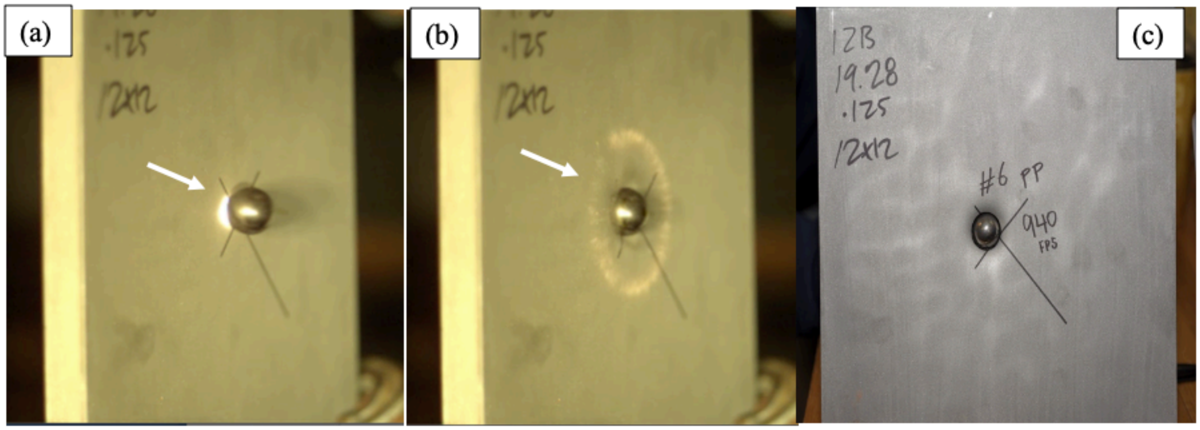

Figure 23. a) Screen shot of the high-speed video showing the steel ball in test #6 arriving at the surface of the SS-CMF-CSP target igniting upon impact (showed by arrow), b) Screen shot of the high-speed video in test # 6 showing the impacting ball and its resulted tensile waves bouncing back, c) the Strike face of test # 6 with the projectile steel ball welded to the surface upon impact

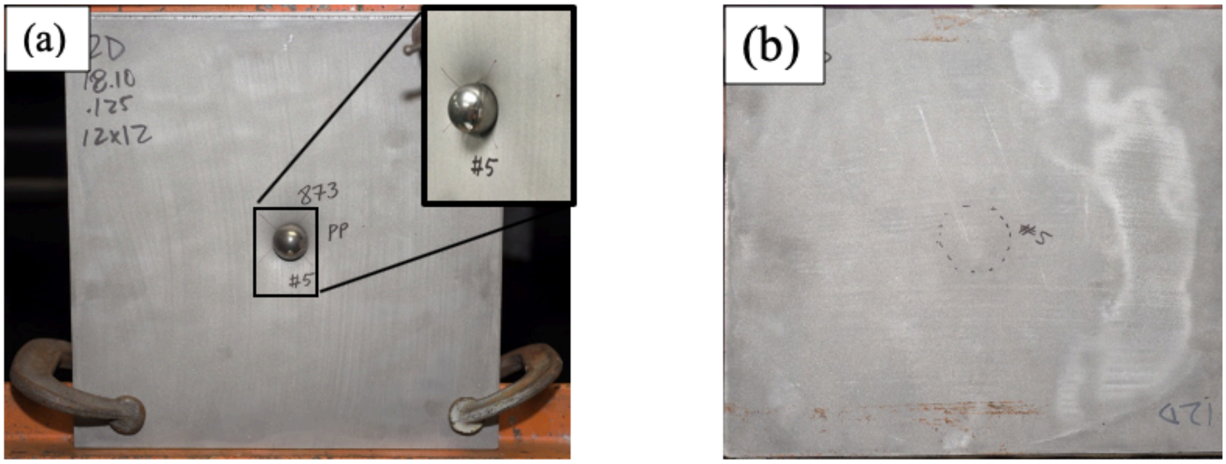

Figure 24. a) the Strike face and b) the back face of Test #5 with the steel ball projectile stuck to the surface with an inset zoom in image of the ball stuck to the surface in a).

In tests 5 to 9, the velocity of the steel ball increased gradually from 266 to 360 m/s by increasing the gunpowder in the 0.50 cal. cartridge case. As a result, the associated energies of the steel balls were increased up to about 4300 joules, as shown in *Table 8*. In all of these tests the steel balls were fused onto the surface of the panel upon impact. Figure 23 shows a screenshot of panel 12B (test 6) at the moment where the steel ball hits the surface. A burst of heat is shown by the arrow at the interface between the ball and the target. The main sources of such a burst of energy are the heat generated through firing the ball, the friction heat between the two surfaces in contact and the heat generated through the high strain rate deformation of the panel and the ball at the point of impact. Upon arrival of the ball at the surface of the sandwich panel such heat fuses the ball that is pressed against the panel creating an instant bonding/ welding between the two (similar to a friction stir welding).

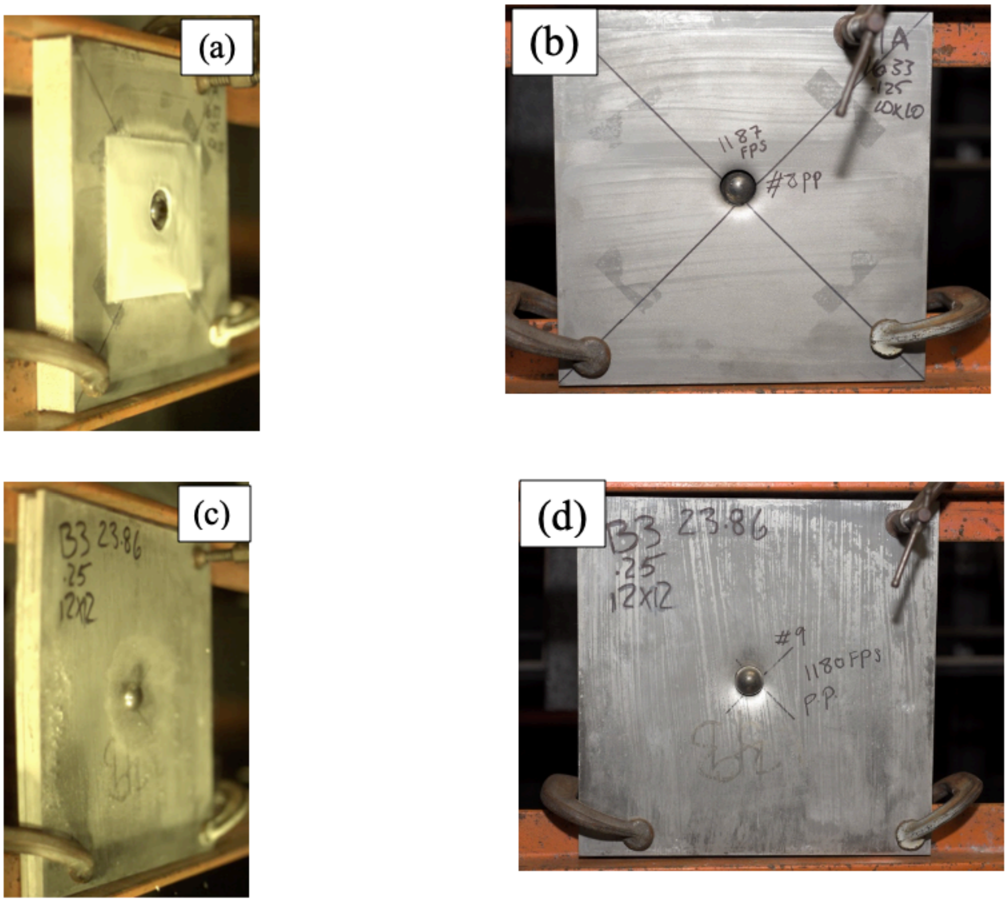

Figure 25. a) and b) the Strike face of Test # 8; c) and d) the Strike face of test # 9. Both panels have similar projectile velocities and impact energies. Test 8 has thinner face sheets and thicker SS-CMF core while test 9 has thicker face sheets and higher total weight. The steel ball projectiles stuck to both panels but comparing the screen shots of the ball in a) and c) suggest larger bending in panel 9 while panel 8 absorbs the energy through thicker SS-CMF layer. Note: the white sheet over image a) is a thin sheet of Teflon that was taped over the panel to prevent the steel ball from welding to the surface. But it was not capable to do so and the ball welded anyway.

As the kinetic energy of the steel ball increases in tests 5-9, the depth of penetration of the ball into the top face sheet progresses resulting in the gradual build up of compressive waves on the SS-CMF core layer until it yields and further deforms plastically at higher compressive loads absorbing the kinetic energy of the steel ball. Figure 24 shows the front and back of test #5 (panel 12D). As can be seen, the face sheet has a slight indentation, but no major deformation or damage can be observed in either front or back face of the panel.

Large stress gradients between the area directly underneath the steel ball projectile (compression) and its surrounding area (tension) creates shearing stresses in the top face sheet of the sandwich panel. Such shear stress increases with increasing the velocity of the steel ball that in some of the panels with thinner face sheets (tests 6, 7, 8 and 10) eventually tear the top face sheet allowing the ball to penetrate through the first layer of the panel. But, the SS-CMF core layer traps the ball using its extra-ordinary energy absorption in compression and stops its complete penetration. Note that test 9, used a thicker face sheet that could resist such shearing stresses. Figure 25 shows the front and back of panels 1A and B3 (tests 8 and 9, respectively). While 1A has thinner face sheets, both panels could absorb the entire energy of the steel ball projectile without any major deformation on the back face. Panel 1A with lower areal density could stop the ball within the SS-CMF core after the face sheet was sheared, while B3 (with thicker face sheets) could stop the projectile without shearing of the face sheet. However, the entire panel was bent as the SS-CMF layer was not thick enough to absorb and dampen the impact energy (Figure 25-c) meaning that thicker SS-CMF core panels will be needed to absorb the impact energies efficiently.

Upon the impact of the steel ball projectile, the compressive stresses of the ball traveling through various layers (face sheet/SS-CMF core/ and back face), experiencing sudden changes in mechanical impedance between various layers. The impedance of SS-CMF can be estimated using the simple equation of the impedance (Z) as:

$$\mathrm{Z} = \sqrt{\mathrm{E}\rho} \qquad (1)$$

where E is material's modulus and ρ is its density. Considering the fact that the density of SS-CMF is about 35% that of bulk steel (13) and its tensile modulus of elasticity is 2.3% that of bulk steel (E SS-CMF= 4.36 GPa (59) and E stainless-steel = 193 GPa (60)) the impedance of SS-CMF core is about 9% that of steel face sheets. As such at the time of impact of steel ball to the sandwich panel's face sheet, tensile stresses are created due to the sudden changes in mechanical impedance between stainless steel face sheets and SS-CMF core as well as the stainless steel back face and air. These tensile stresses are reflected from the back into the sandwich panel towards the impact face. At lower impact energies of the ball, the energy passing through the panel, creating tensile waves assist bouncing the ball back as could be seen in tests 1 - 4. At higher impact energies of the ball, when the ball itself welds to the surface of the panel, the tensile waves will pull the ball and the panel towards the projectile resulting in debonding at the interface between the face sheets and the core. Such debonding was mostly observed in adhesively bonded samples such as tests 4 and test 10. The diffusion bonded panels, however, have a higher ductility at the bonding layer due to the uniformity of the stiffness of the core and the bonding layer, making the panel more capable of accommodating the combination of tensile and compressive stresses associated with the projectile impact. One interesting observation is that test 4 shows debonding in between the front face sheet and the SS-CMF core, while test 10 with higher impact energy caused debonding of the back face from the SS-CMF core. This phenomena could be due to the lower impact or puncture energies that were all absorbed by the front panel and localized plastic deformation of SS-CMF core in tests 4 resulting in the reflective tensile stresses bouncing from SS-CMF core- face sheet interface that separated the front sheet. The energy of the projectile in test 10 on the other hand was large enough to engage the entire thickness of the panel and reach all the way to the back plate. Upon reflecting from the back, the tensile stresses separate the back face from the core. All other panels tested at high impact velocities with some degrees of separation showed the same phenomena as test 10.

Round 2 of experiments with higher impact/ puncture energies

Since in the first set of puncture tests all steel balls were caught by the SS-CMF sandwich panel targets, a second set of experiments were designed with larger steel balls (double the mass of the projectile) and increased velocity of the ball using different type of gunpowder. In this set of tests, 7 steel balls were shot at 6 SS-CMF core sandwich panels, all having about 1 cm thick SS-CMF core (except panel 12F that was thicker) and all processed through diffusion bonding. Four panels had thicker face sheets of 0.635 cm and two others had face sheets of 0.3175 cm. Table 9 illustrates the velocity of the steel balls for each test along with their associated impact or puncture energies. In this case the velocities ranging from 350 to 470 meter per second was achieved, resulting in puncture energies of 8100 to over 14,500 joules.

Similar to the first set of experiments, all panels could catch the steel balls without a complete penetration/ or puncture through, even the lightest panel with an areal density of 6.7 kg did not show a complete penetration of the projectile. One of the lighter panels, target B4, was shot twice and the second shot, aimed onto the back of the panel, did result in a complete penetration. Figure 26 shows the strike face and back face of the panel B4 after the first shot and a close up of two projectiles after the second shot. Since that panel was already compromised after the first shot, its second shot result should only be considered for information purposes and not a true representation of the puncture performance of the sandwich panel.

In the rest of the panels the steel balls were struck at the surface of each target with increased velocities and all of those were stopped with steel balls fused on the surface of the panel as is evident in Figure 27 through Figure 29. Figure 27 compares the results of Tests 2 and 5. These two panels had similar thicknesses of SS-CMFcore, but the thicknesses of their face sheets were different. The thickness of the face sheets of panel 44A (test #5) was double those of the panel 7A2-18 (test #2). However, despite a large difference in their resulting areal densities, they both performed similarly in stopping the projectile without a complete puncture. Both panels show a tear up of the front panel and stopped the projectile at the SS-CMF core layer. Interestingly though, both panels

Table 9. Summary of the steel ball velocities, their associated energies, and the performance of SS-CMF-CSPs in the second round of experiment using 3.175 cm steel balls

Test #	Panel #	Steel ball velocity, m/s	Energy of steel ball at the target, Joules (ft.lb)	Notes
1	B4 1st shot	352	8109 (5980)	Ball fused, front face tearing, back face debonding, small back indentation
2	7A2-18	354	8208 (6053)	Ball fused, front face tearing, back face complete debonding, small back indentation, no gap between projectile & surrounding SS-CMF
3	B4 2ND shot	400	10445 (7703)	Ball penetrated through upon the second shot, front and face tearing,
4	B1	398	10366 (7644)	Ball fused, front face tearing, back face complete debonding, small back indentation, SS-CMF stuck to back plate, large gap between projectile & surrounding SS-CMF
5	44A	395	10176 (7505)	Ball fused, front face tearing, back face complete debonding, small back indentation, SS-CMF stuck to back plate, large gap between projectile & surrounding SS-CMF
6	12G top	397	10271 (7574)	Ball fused, front face tearing, no back face debonding, small back indentation,
7	12F	472	14522 (10710)	Ball fused, front face tearing, small back indentation,

had a delamination of their back face allowing a closer investigation of the inner surfaces of panels.

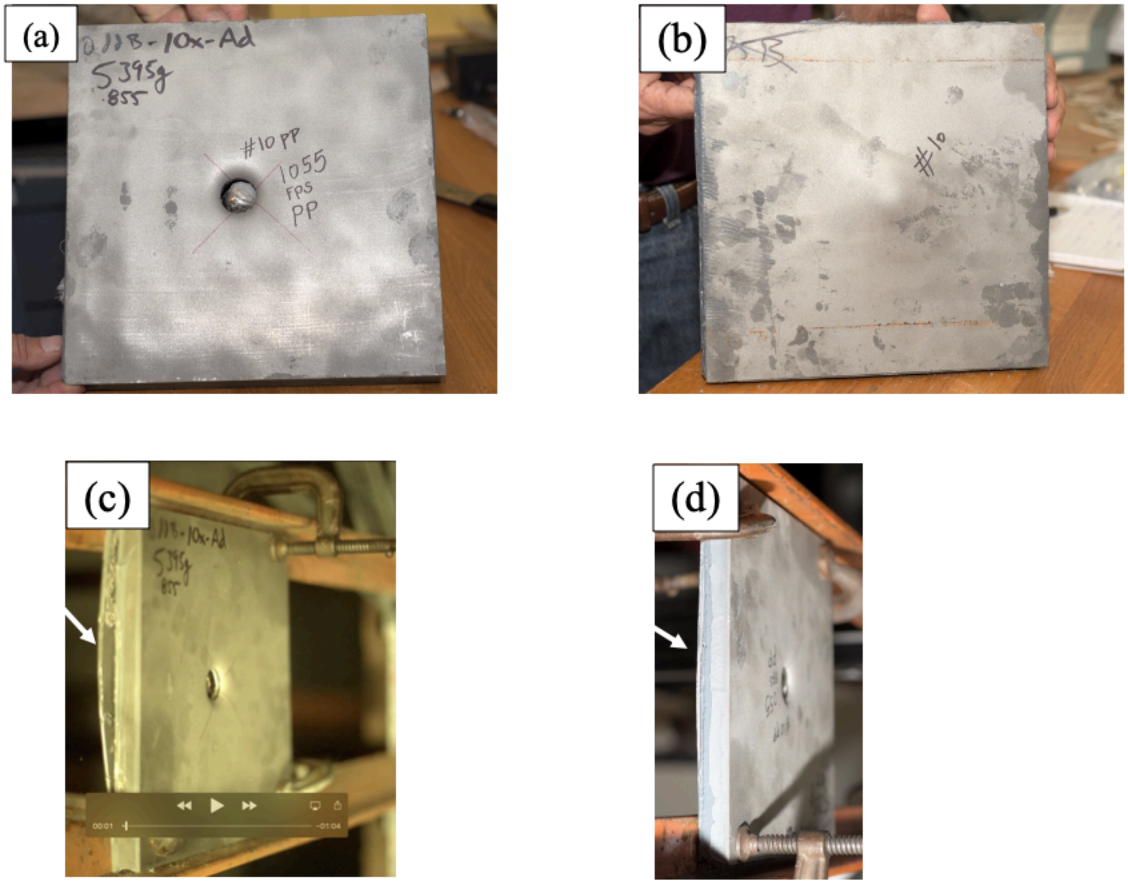

Figure 26. a) Front, and b) Back of test panel #10 with adhesion bonding; c) screen shot of the high-speed video and d) image of the side of the panel after the test both showing a separation of the back face marked by an arrows.

Figure 28 shows the closeup of the interface between the back faces and SS-CMF core of both panels. As can be seen, the radial cracks (resulted from reflected tensile stresses) in both panels are limited to the area around the projectile impact and the rest of the panel is not damaged. The back face deformation seems to be far from a complete puncture through. This can be due to the energy absorption of composite metal foam core. One major difference observed between *Figure 28*-b and *Figure 28*-d is the gap between the projectile area (center) and surrounding SS-CMF core. This gap is much larger in panel 5 (Figure 27-b) indicating the large tensile waves bouncing off of thicker face sheets in panel 5 compared to the lower tensile waves generated at thinner face sheets of panel 2. This is a good indication that the SS-CMF core is the main energy absorbing component in the ensemble and panel 5 was over designed for this purpose.

A thinner layer of face sheet could be sufficient for this purpose. A second look at Figure 27-b and Figure 27-d confirms that argument as the back face deformation look the same in both panels. Another interesting phenomena is the separation of the SS-CMF core from the steel ball projectile area and stuck over the thicker back face as shown in *Figure 28*-C, while *Figure 28*-e shows that the thin back face is clean and all SS-CMF core is stuck to the projectile area shown in 13-d. This is also resulted from the large tensile stresses generated at the thicker back plate of test 5 that separated the SS-CMF from the projectile while test 2 with thinner face sheets and lower tensile waves did not separate the SS-CMF from the projectile itself. The crushed spheres shown in 13-c also confirm that the compressive stresses absorbed by the SS-CMF core.

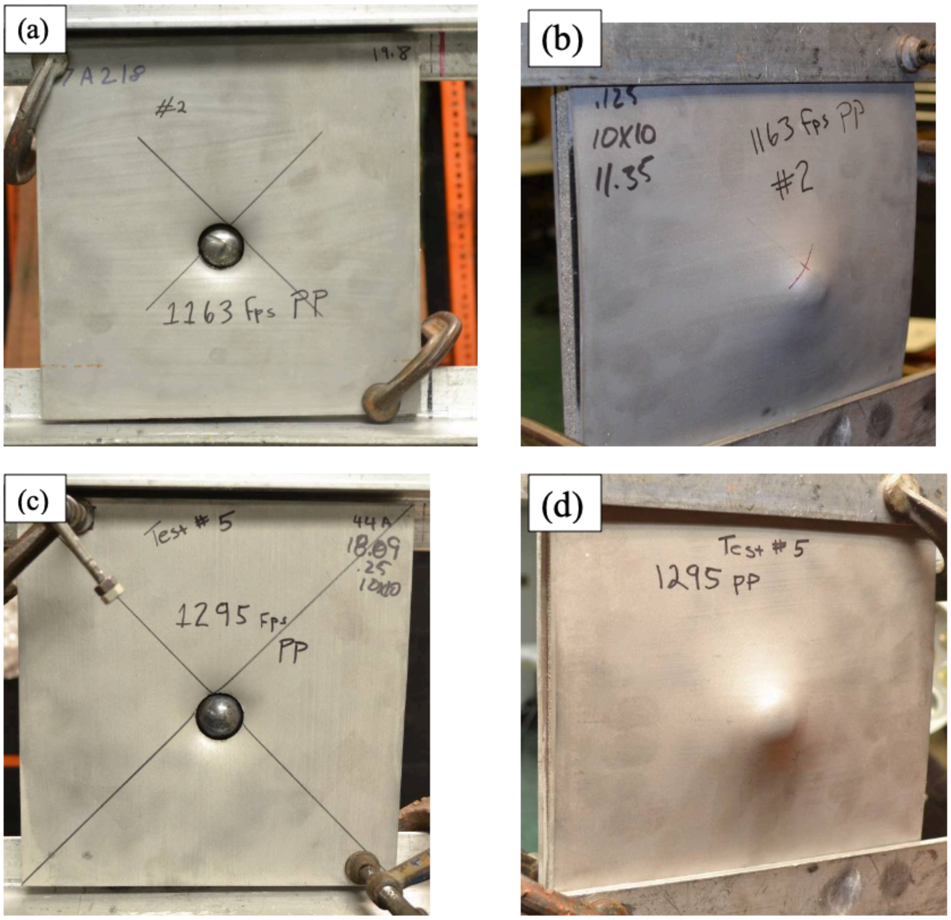

Figure 27. a) and b) the strike and back faces of Test #2; c) and d) the strike and back face of test #5 both in second series of testing and both have same thickness and mass of SS-CMF core. But, the total areal density of panel #5 is almost double that of panel #2 due to its thicker face sheets. Both panels show tearing of the face sheets and debonding of the back plate, but could catch the projectile and absorb its entire energy within the SS-CMF core.

Figure 29 shows the strike and back face of tests 6 and 7 with the highest puncture energies of over 10,000 to 14,500 joules. As can be seen in this figure, the steel balls stuck on the strike face of both targets. Test 7 panel did show shearing of the strike face and penetration of the steel ball into the panel. But, the ball was soon caught by the SS-CMF core and stopped without tearing the back plate. Interestingly, the back face was not separated from the SS-CMF core. This indicates the toughness of the diffusion bonding layer. As previously discussed, because of the significance of impedance matching of these layers, further studies will be necessary to optimize the diffusion bonding process of future panels.

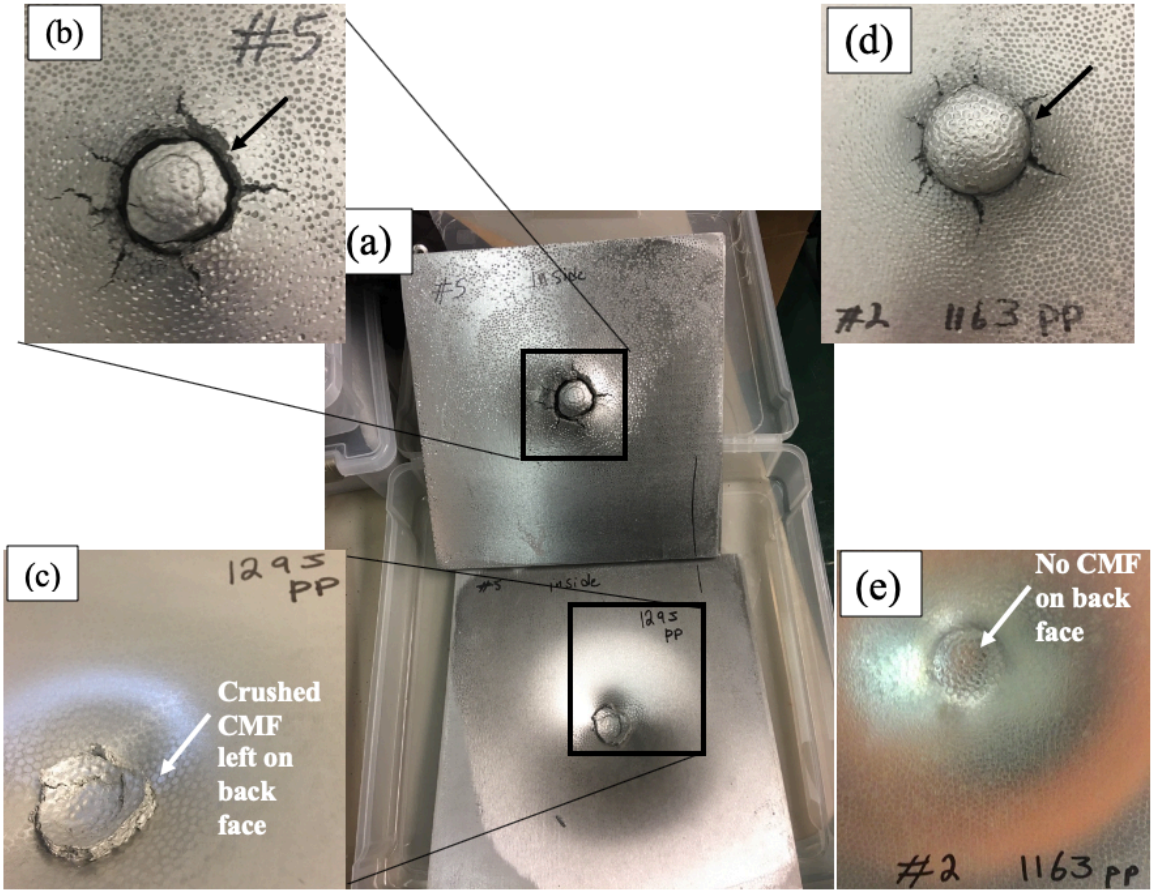

Figure 28. a), b) and c) show the debonding interface between the back plate and SS-CMF core of panel 44A (test #5) with a zoom in of the SS-CMF core in b) and the left-over of the core on the back face in c). Figures d) and e) show the same areas of b) and c) in the panel 7A2-18 (test #2) with thinner face sheets and a much lower areal density.

Figure 30 shows the puncture/ or impact energy absorption of all panels tested in both sets of experiments as a function of the areal densities of each panel. In order to be able to compare various panels with different components, an equivalent areal density is calculated based on the actual dimensions and weight of each panel and shown in Table 6 and Table 7 along with Figure 30. It is notable that none of these panels were perforated through. The second set of tests shows that even lighter panels with less than 7 Kg areal densities were sufficient to absorb the large impact energies without any complete penetrations. This is due to the large energy absorption capacity of composite metal foam core of the sandwich panel, while the face sheets improve the performance of the CMF core under tension. The face sheets also offer a non-porous surface that can protect against corrosion and be used in a variety of engineering applications. Even though this study shows good puncture resistance of SS-CMF core sandwich panels, a full-scale puncture test is required to evaluate the survivability of SS-CMF core sandwich panels for tank-car-head puncture-resistance systems.

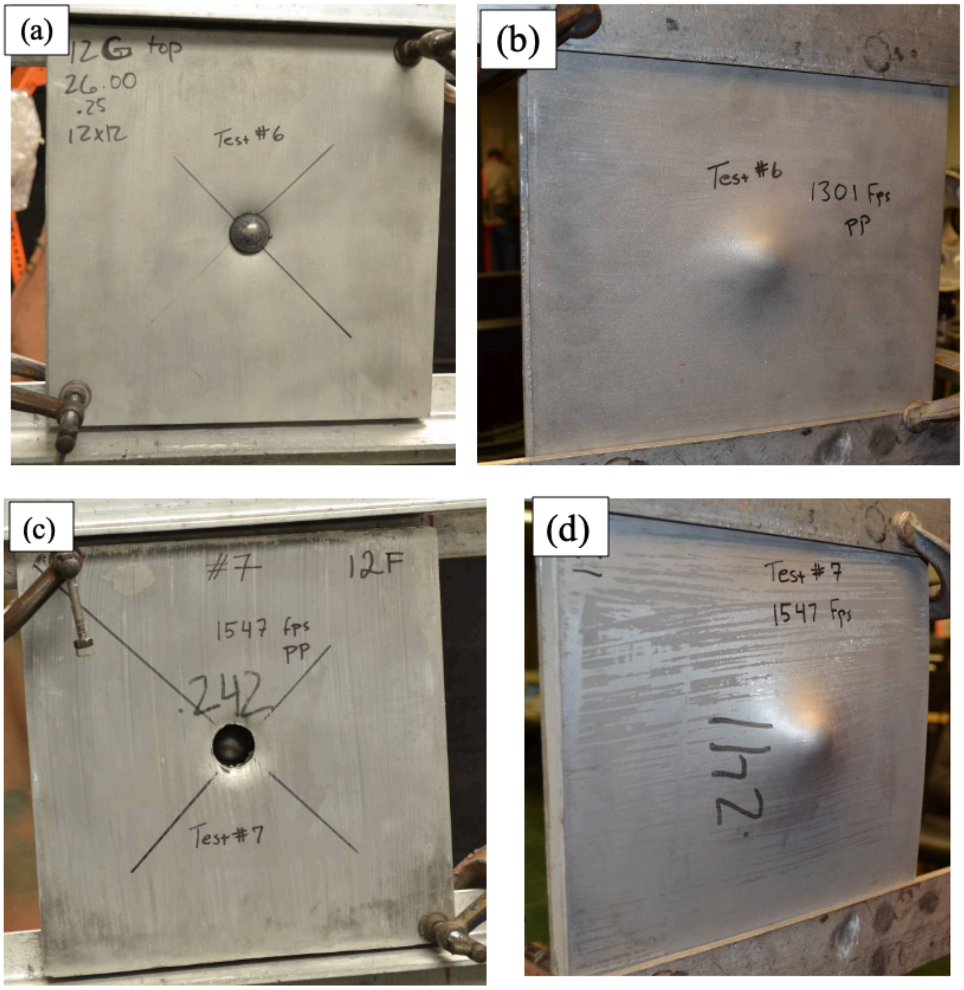

Figure 29. a) and b) the strike and back face of Test #6 absorbing over 10,000 joules of puncture energy without any puncture through the panel; c) and d) the strike and back face of Test #7 absorbing about 14500 joules of puncture energy without any complete perforation through the panel.

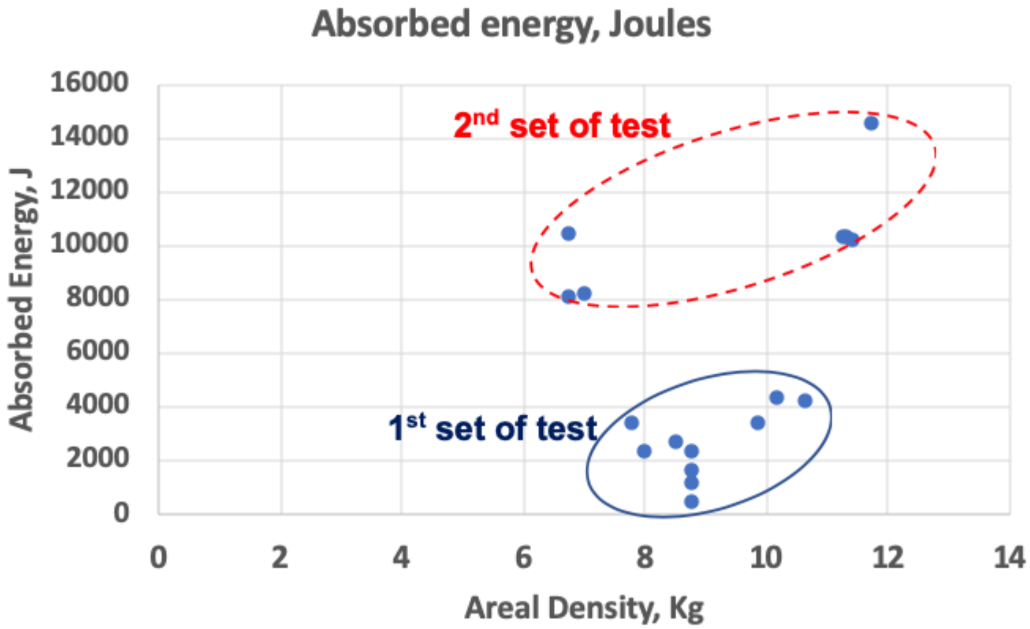

Figure 30. Puncture energy absorbed by each SS-CMF-CSP panel through the two sets of tests versus each panel's areal density. None of these tests caused a complete puncture through the thickness except one that was shot twice with the second shot at a close vicinity of the first shot.

7.4 Conclusions

Two sets of puncture tests were conducted on steel-steel composite metal foam core sandwich panels with two different thicknesses of stainless steel face sheets. The bonding of the SS-CMF core and face sheets was through adhesive bonding and diffusion bonding. Panels assembled using adhesive bonding were showing a debonding of the face sheets from the core upon the impact of the projectile at lower velocities. A close observation of the bonding area after each puncture test indicated that the epoxy adhesive bonding with a stiffer bonding layer does not accommodate the shear and normal stresses upon impact resulting in debonding of the face sheets from the SS-CMF core at lower impact velocities. The diffusion bonded panels with a cohesive bonding interface show more flexibility at the interface and better accommodate the stresses particularly at lower impact energies. Most diffusion bonded panels were not showing debonding of face sheets from SS-CMF core, except for those tested at higher impact energies indicating a preferred process of assembling SS-CMF core sandwich panel can be through diffusion bonding. However, additional studies needed to optimize the bonding strength between SS-CMF core and face sheets. Various thicknesses of the CMF core and face sheets created a variety of target areal densities from about 6.7 to about 11.7 Kg per each tile of 30x30 cm. Targets were impacted using 2.54 and 3.175 cm diameter steel balls fired at velocities ranging from 120 to 470 meter per second resulting in puncture energies from 488 to 14,500 joules. However, none of the panels, even those with the lowest areal densities, showed a complete penetration / puncture through their thickness. This was mostly due to the energy absorption capacity of the SS-CMF core in compression, while the face sheets strengthen the CMF core to better handle tensile stresses. Sandwich panels with thicker face sheets show less effectiveness and a thin face sheet seemed to be sufficient to support the SS-CMF core for absorbing such puncture energies. Even though this study shows good puncture resistance of SS-CMF core sandwich panels, a full-scale puncture test is required to evaluate the survivability of SS-CMF core sandwich panels for application in tank-car-head puncture-resistance systems.

8 Pool Fire Testing and Modeling of a Composite Metal Foam

8.1 Abstract

A comprehensive experimental and numerical simulated pool fire test is conducted on stainless steel composite metal foams (SS-CMF) panels and is reported in this chapter. The uncertainty assessment for the measured and calculated results on the unexposed surface temperatures in the calibration and simulated pool fire tests on the SS-CMF specimens are also conducted and reported. This test procedure is designed to measure the thermal effects of new or untried thermal protection systems, such as S-S CMF, and to test for its survivability when exposed to a 100-minute pool fire condition. The assembly was tested in triplicate in three consecutive simulated pool-fire exposures as specified in 49 CFR Part 179, Appendix B and achieved successful results. Based on the experimental and modeling results as well as the uncertainty studies, the 15.9 mm thick steel-steel composite metal foams tested as novel insulation system met the acceptance criteria for the simulated pool fire test in 49 CFR 179 Appendix B by a large margin and is expected to pass with near certainty if the test were to be reproduced in a different laboratory. The main reason for successful performance of SS-CMF is attributed to the large air content in the material. The numerical studies reported in this study indicated that the low surface emissivity of the material is also contribute to the superior performance of the material to some extent. To complete the full test requirements of CFR Part 179 App. B, the material will need to be tested against the torch-fire exposure in duplicate. This research indicates that one of the potential applications of lightweight SS-CMF can be in tank-cars carrying hazardous materials and replacing conventional structural steel with demonstrated benefits of excellent thermal insulation, fire resistance, low weight along with its established energy absorption capabilities.

8.2 Pool Fire Tests

Material Tested

Three panels of 305 × 305 × 16 mm panels of Steel-Steel Composite Metal Foam (S-S CMF) were manufactured for testing using a previously-discussed powder metallurgy technique (14). The SS-CMF panels consisted of 2 mm diameter hollow stainless steel spheres surrounded by a 316L stainless steel matrix. After hot press processing, each SS-CMF panel was cleaned and surface ground using a 35 x 150 cm Gallmeyer & Livingston Co. “Grand Rapids” grinding machine to create a flat surface and uniform thickness of 1.59 cm.

A base ASTM A516 Grade 70 steel plate of 40.6 × 40.6 × 1.59-cm dimensions was used for calibration of the furnace. The plate is constructed in a manner such that heat is transferred only by conduction through the plate and not through any other heat paths. The base plate also works as the sample holder providing a 5 cm lip around the perimeter of the test panel that will be centered over it. Table 10 shows the specification of all three SS-CMF panels as well as the grade 70 steel calibration panels used in this study.

Table 10. Test Material Information.

Material Name	Measured Thickness (cm)	Measured Width × Length (cm)	Measured Weight (g)
Steel-steel CMF Sample C-2	1.59	30.2 x 30.2	3,805
Steel-steel CMF Sample C-3	1.58	30.2 x 30.2	3,732
Steel-steel CMF Sample C-5	1.59	30.2 x 30.2	3,661
Pool-Fire Calibration Plate[1]	1.59	40.6 × 40.6	20,443[3]
Pool-Fire Test Plates (3)[2]	1.59	40.6 × 40.6	20,443[3]

[1] Steel plate used in simulated pool fire calibration

[2] Steel plates used as a sample holder for the CMF specimens

[3] Estimated based on the dimensions and the density.

Test Method:

The pool fire test was conducted at Southwest Research Institute® (SwRI®) in San Antonio Texas according to the test methods described in 49 CFR Part 179, Appendix B. These tests are intended to evaluate the thermal resistance of new or untried thermal protection systems for tank-cars and to test for system survivability.

A pool-fire environment is simulated by combusting a hydrocarbon fuel to obtain exposure temperatures of 871 °C ± 73.3 °C for the 100 minutes duration of the test. Since Steel loses load carrying capacity and begins to deform at 427 °C, the maximum fail/ pass temperature for simulated pool fire testing is set at 427 °C in accordance with the Federal Railroad Administration's simulated pool fire test methods described in 49 CFR Part 179, Appendix B. Prior to testing the SS-CMF panels, a calibration is conducted to ensure the specimens are exposed to a proper heat flux at this temperature. For the simulated pool-fire calibrations, a 40.6 × 40.6 × 1.59-cm base steel plate with nine Thermocouples (TCs) installed on the unexposed face, in accordance with 2.a.2 of 49 CFR Part 179 App. B, was placed in the same sample holder used for the test runs. The sample holder exposed 30.5 × 30.5 cm of the base plate to the furnace conditions. A ceramic fiber blanket was used over the 5 cm lip around the perimeter of the test panel to ensure no paths of heat transfer on the samples except for conduction directly through the CMF testing panel. Furnace temperatures during the calibration and tests were measured at four evenly distributed points within the furnace, approximately 30.5 cm in front of the center point of the walls, 42.5 cm below the exposed surface of the test samples.

The calibration was considered successful if a minimum of two TCs reach a temperature of 427 °C (800 °F) after 13 ± 1 min. Figure 31 shows the arrangement of thermocouples on the unexposed surface of the calibration steel panel as well as the small horizontal furnace used for pool fire testing with lid removed. For the simulated pool-fire exposure, a containment frame was used that had one opening to measuring nominally 30.5 × 30.5 cm (1 × 1 ft) for assembling the test panel.

Three 15-min calibration tests were conducted prior to the simulated pool fire experiments on the SS-CMF specimens. All tests were conducted in the small horizontal fire resistance test furnace (interior dimensions: 1.44 × 1.44 × 1.5 m) at Southwest Research Institute® (SwRI®). The purpose of the calibration tests was to establish the furnace gas target temperature and the corresponding furnace burner settings to achieve the thermal exposure conditions for the SS-CMF experiments specified in the CFR.

After the calibration, the SS-CMF panels were centered over the exposure side of the base steel plate and placed at the center of a horizontal furnace closure for testing in the simulated pool-fire environment. The test samples were instrumented in the same manner as the calibration plate. According to the 49 Code of Federal Regulations (CFR) Part 179, Specifications for Tank-car, Appendix B Procedures, the simulated pool-fire test is considered successful if, after 100 min of exposure, no TCs on the unexposed surface of the testing panel (SS-CMF in this case) register a temperature greater than 427 °C (800 °F). Moreover, a minimum of three successful simulation pool-fire tests must be performed with a minimum time interval of 8 h between the completion of one test and the start of the next. As such, the three SS-CMF samples were individually tested in three consecutive days with one simulated pool-fire test per day.

The small-horizontal furnace used in this study has overall inner chamber dimensions of 1.52 × 1.52 m Figure 31. The furnace is equipped with four pre-mixed natural gas burners and is capable of exposure temperatures of up to 1260 °C (2300 °F). The furnace consists of a steel shell, lined with ceramic fiber insulation. A steel furnace gas exhaust plenum is located at the bottom of the shell. The plenum is connected to an exhaust fan and smoke abatement system. The furnace gases are extracted through open vents located at the four corners of the furnace. Ceramic fiberboard risers (Morgan Thermal Ceramics KWL) are placed in each corner to ensure that all combustion products, which accumulate below the furnace lid, are continuously extracted.

The walls of the shell are insulated with 203 mm thick refractory fiber modules (Morgan Thermal Ceramics Z-Blok®) covered with a single layer of 25 mm ceramic fiber blanket (Morgan Thermal Ceramics 96 kg/m^3 Superwool®). Furthermore, the steel plate separating the furnace from the exhaust plenum is covered with two layers of 25 mm ceramic fiber blanket on the furnace (top) side and insulated with an additional three layers of blanket on the plenum (bottom) side. The steel furnace lid is also insulated with three layers of 25 mm ceramic fiber blanket. The resulting interior dimensions of the furnace are 1.44 × 1.44 × 1.5 m.

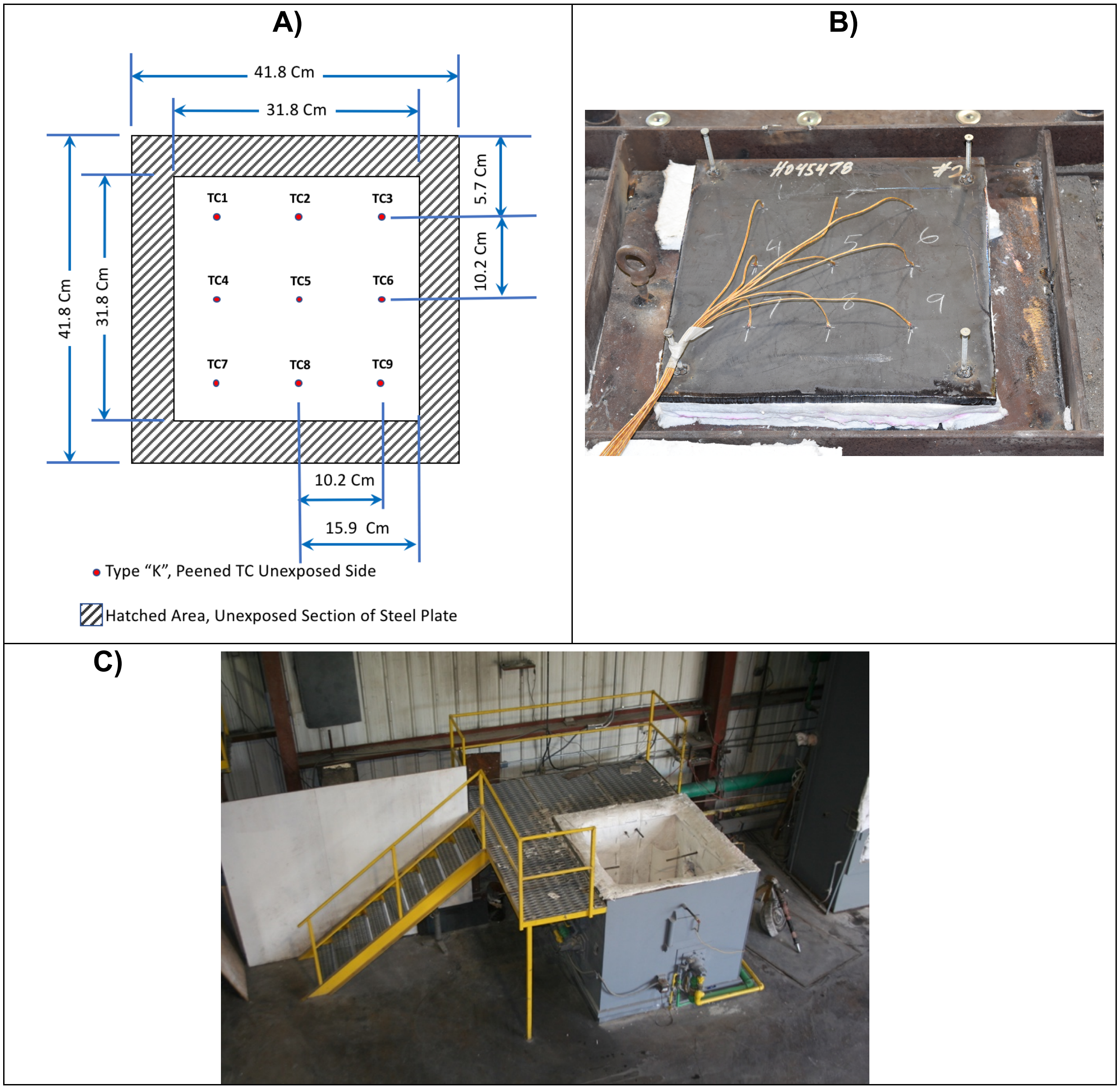

Figure 31. A) Drawing of the calibrating base steel plate with the position of all 9 thermocouples and B) Digital image of the calibrating base steel plate with nine thermocouples assembled on its unexposed surface, C) Small horizontal furnace with lid removed used for simulated pool fire testing.

Due to the furnace temperature requirement for this exposure, only three of the four burners were used during testing. The interior furnace temperature was measured using four exposed bead, non-shielded, quick response, Type K TCs which were evenly distributed across the area of the furnace located 42.5 cm (16.75 in.) below the surface of the samples. The interior furnace dimensions along with the frame used provided for full engulfment of the exposed 30.5 × 30.5-cm (1 × 1-ft) face of each sample.

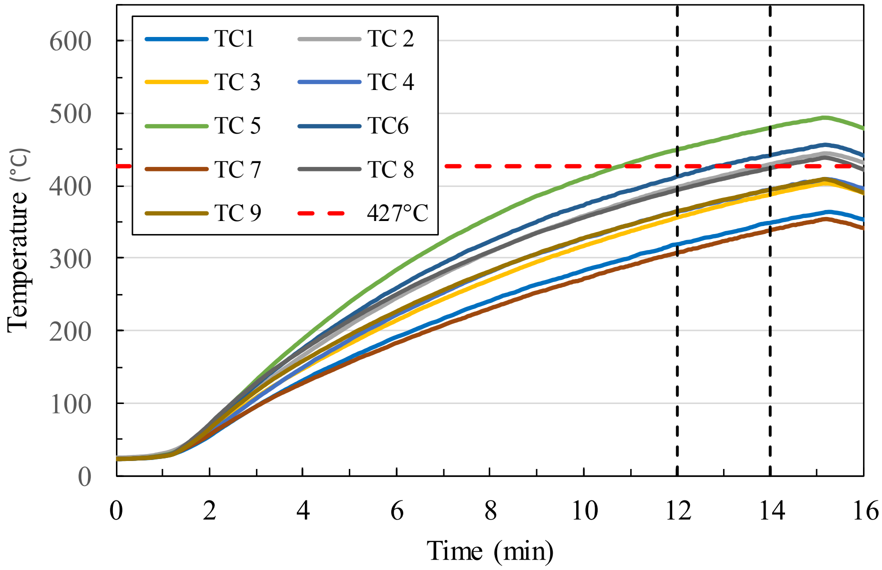

Figure 32. Unexposed Surface Temperatures from the Third Calibration Test (61).

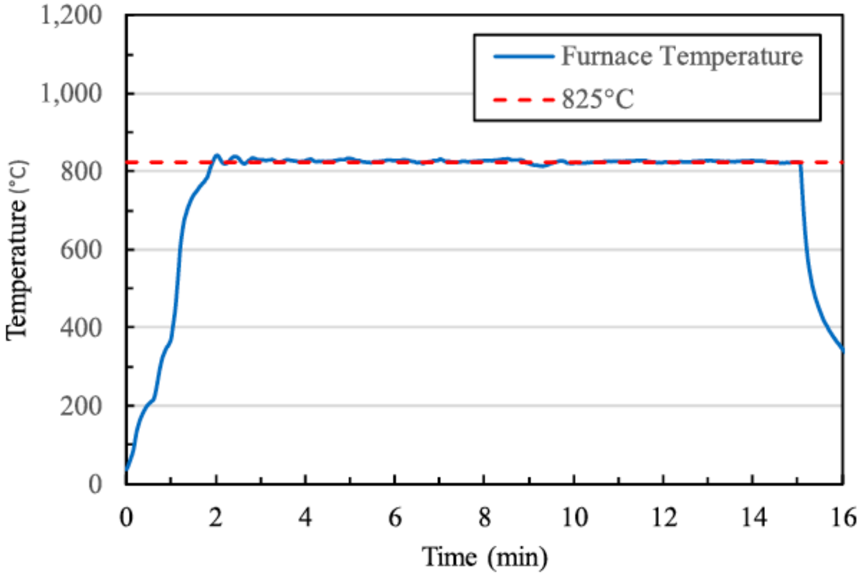

Figure 33. Time-temperature curve of the furnace during calibration for simulated pool-fire tests.

In each calibration test, a base 0.406 × 0.406 m ASTM A516 Grade 70 carbon steel plate, 16 mm in thickness, was mounted on top of a 0.305 × 0.305 m opening in the furnace lid. The latter consisted of a stiffened 6.35 mm thick steel plate, insulated on the furnace (bottom) side with three layers of 25 mm thick ceramic fiber blanket (density 96 kg/m^3). Type K thermocouples (TCs) were installed at nine locations in a 3 × 3 array on the unexposed face of the plate, as shown in Figure 31.

The steady furnace gas temperature that was used in the simulated pool fire tests was determined from a calibration test in which at least two of the nine specimen TC readings are equal to or greater than 427°C after 13 ± 1 min of exposure. The latter was accomplished in the third calibration test, and the furnace gas time-temperature from this calibration (linear rise to 825°C in 2 min, followed by a steady temperature of 825°C for the remaining 13 min) was used in the SS-CMF simulated pool fire tests. The unexposed plate surface temperatures measured in the third calibration test are shown in Figure 32 while Figure 33 shows Time-temperature curve of the furnace during one of the calibration for simulated pool-fire tests.

8.3 Experimental Results

Calibration Results:

The average initial plate temperature was measured to be 23.7 °C prior to the calibration. Furnace run was conducted at 825 °C continuous temperature and the conditions specified in 2.a.6 of 49 CFR Part 179 App. B were achieved with three of nine TCs reaching 427 °C (800 °F) at 13 min ± 1 min. Successful calibration results for the simulated pool-fire tests can be seen in Figure 32 and Figure 33. The setup used for the calibration test was duplicated for all three simulated pool-fire exposures, including the distance between the TCs and the sample, the distance from the four furnace burners and TCs, and the average furnace temperature.

Test Results:

Three simulated pool fire tests were performed. In each test, a 302 × 302 × 16 mm SS-CMF specimen was exposed to a constant temperature furnace environment at 825°C for 100 min. The specimens were backed by a 16 mm thick carbon steel plate, identical to that used in the calibration tests, instrumented with nine thermocouples inserted into the unexposed surface of the plate. The unexposed surface thermocouple layout was the same as that in the calibration tests. At no time during the three tests did any of the nine thermocouples indicated a temperature in excess of the failure threshold of 427°C and all temperatures stayed well below 400°C.

Figure 34 shows the exposure side of two SS-CMF samples (C-2 and C-5) with one panel showing the ceramic fiber blanket over the 5 cm lip around its perimeter and the other panel assembled at the center of the top closure of the horizontal furnace, prior to simulation pool-fire testing. The unexposed surface temperatures measured in the first simulated pool fire tests are shown in Figure 35. As can be seen both in Table 11 and

Figure 35, all SS-CMF panels successfully passed the requirements of 49 CFR Part 179 Appendix B simulated pool fire for the new isolating system with a large margin showing that the 15.9 mm thick steel-steel CMF can perform as insulating material. The table shows the highest temperature registered behind each of the three CMF panel over the course of the 100 minutes duration of the simulated pool-fire test. The table also shows that TC-5, which was the thermocouple located in the center of the panel registered the highest temperature on each sample. The superior performance of SS-CMF in such simulated pool fire testing can be related to the presence of large percentage of air bubbles inside the steel plate. Figure 36 shows the exposed side of two of the SS-CMF (panel C-2 and C-3), both after 100 minutes exposure to the simulated pool fire conditions. Comparing the before and after images of the CMF panels, it is clear that the SS-CMF panels only experienced minor discoloration and surface oxidation after 100 minutes exposure to 825 °C without any warping, cracking or other visible damages.

Figure 34**.** Exposure side of A) CMF sample (C-5) with a ceramic fiber blanket over the 5 cm lip around its perimeter , B) another CMF sample (C-2) assembled at the center of the top closure of the horizontal furnace, prior to simulation pool-fire testing.

Table 11. Simulated Pool-Fire Test Experimental Results on SS-CMF panels.

Test No.	**Sample No.**	**Initial Plate Temp**	**Max Temperature Measured at 100 min**
1	C-5	21.5 °C	379.7 °C (TC 5)
2	C-3	18.3 °C	351.6 °C (TC 5)
3	C-2	20.5 °C	376.2 °C (TC 5)

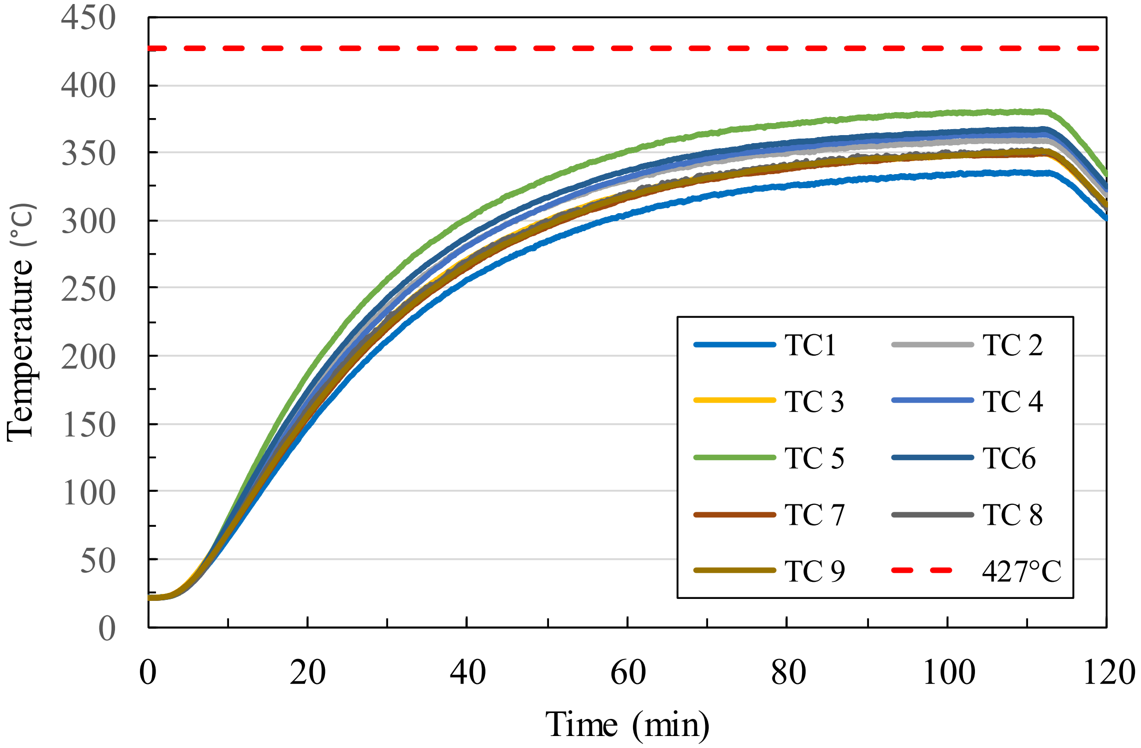

Figure 35. Unexposed Surface Temperatures from the First Simulated Pool Fire Test

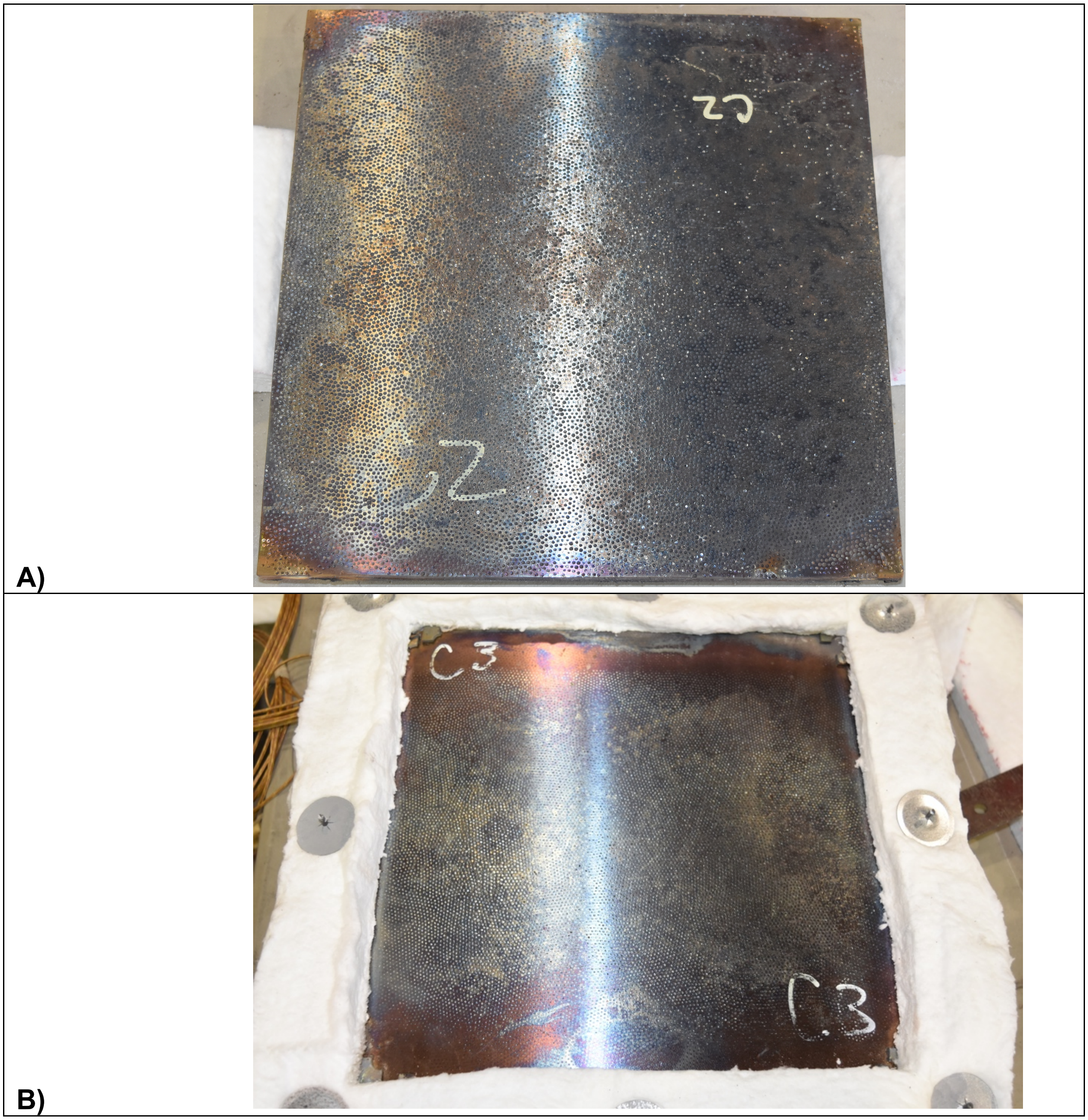

Figure 36 Exposed side of A) Sample C-2 and , B) Sample C-3, both after 100 minutes exposure to the simulated pool fire conditions showing no major sign of physical damage to the panel due to extended exposure to heat.

8.4 FDS Modeling (1-D model)

This section describes the development of a mathematical model to predict the performance of the SS-CMF samples tested according to the simulated pool fire test procedure specified in 49 CFR Part 179 Appendix B simulated pool fire test.

A two-step process was used to predict the performance of the SS-CMF specimens. The first step involved a numerical simulation of the final calibration test to determine the incident heat flux to the test specimen, which rises from zero at the start of the test to a relatively steady value after approximately 10 min of heating. The second step consisted of a conduction heat transfer analysis to calculate the temperature at the center of the unexposed side of the SS-CMF test specimen and to determine whether the pass/fail limit is or is not exceeded during the 100-min thermal exposure.

In the first step, version 6.7 of Fire Dynamics Simulator (FDS) (62) is used to model the fire resistance furnace in which the simulated pool fire test is performed. FDS is a computational fluid dynamics (CFD) code developed at the National Institute of Standards and Technology (NIST) in Gaithersburg, MD specifically for simulating fires. It is necessary to model the furnace environment because the test procedure defines the thermal exposure conditions in terms of the furnace gas temperature instead of incident heat flux to the specimen surface. Although the incident heat flux to the exposed side of the test specimen, which is needed for the heat conduction analysis in step two, depends on the gas temperature, it is also affected by the furnace wall temperature, direct flame radiation, etc. resulting in the need to model the furnace.

In the first step of modeling, the flow rate has to be determined using an iterative process. This approach will provide the flow rate that results in calculated calibration specimen and/ or furnace gas temperatures that match the measured temperatures.

Step two includes the conduction heat transfer model in FDS, which is a sub-model of the pyrolysis model. FDS provides the option to significantly accelerate the conduction heat transfer analysis by disabling the time-consuming gas phase calculations, which are not necessary to calculate heat conduction when the thermal boundary conditions are known. The pyrolysis model in FDS can handle conduction heat transfer through a solid consisting of multiple layers with multiple components within each layer. Thermal properties of the constituent materials can be temperature-dependent, but conduction heat transfer is assumed to be 1-D, i.e., perpendicular to the exposed surface (although a 3-D version is now available in beta). In future sections of this report the 3-D beta version of the work will be reported to account for lateral heat transfer and heat losses at the edges of the test specimen.

Numerical Simulation of the Calibration Test

Three calibration tests were conducted prior to the simulated pool fire experiments on the CMF specimens. The purpose of the calibration tests was to establish the furnace gas target temperature and corresponding furnace burner settings to achieve the thermal exposure conditions for the CMF experiments specified in the CFR.

In the calibration tests, a 40.6 x 40.6 cm carbon steel plate with a 16 mm thickness, was mounted on top of a 30.5 x 30.5 cm opening in the furnace lid. Type K thermocouples (TCs) were installed at nine locations in a 3 x 3 arrays on the unexposed face of the plate as shown in *Figure 31*. The steady furnace gas temperature to be used in the simulated pool fire tests is determined from a calibration test in which at least two of the nine TC readings are equal to or greater than 427 °C after 13 ± 1 min of exposure to 825 °C. The furnace gas time-temperature from such calibration (825 °C in 2 min, followed by steady temperature of 825 °C) was used in the CMF simulated pool fire tests. The first step of the modeling process, i.e., numerical simulation of the calibration test with FDS, is discussed in the following sub-sections.

FDS Model of the Furnace

A Smokeview (63) rendering of the furnace is shown in Figure 37. Smokeview is a companion program developed at NIST that is used to visualize FDS simulation results. The furnace is equipped with four premixed natural gas burners (Fives North American model No. 4422-6), one in each wall as shown in Figure 37. Only three of the four burners were used in the simulated pool fire tests (the natural gas flow to the burner in the West wall was shut off). The volumetric air flow rate for the three remaining burners was fixed and set at 11 times the maximum burner natural gas flow rate.

The primary component of natural gas is methane. The balance is mostly nitrogen and small amounts of heavier hydrocarbon gases. For the simulation the latter were neglected and it was assumed that the net heat of combustion of the natural gas used in the simulated pool fire tests was 45,810 kJ/kg (64). Based on a net heat of combustion of 50,030 kJ/kg for methane (65), this implies that the mass fraction of methane Y_{CH_4} = 45,810/50,030 ≈ 0.916 g/g and the mass fraction of nitrogen is therefore equal to Y_{N_2} = 1- 0.916 = 0.084 g/g.

Initially the plan was to model the combustion of the premixed natural gas-air mixture. However, by default FDS assumes that the fuel and oxidizer are not premixed and that the rate of the combustion reactions is controlled by turbulent mixing (turbulent diffusion flame). Premixed combustion can be modeled in FDS, but the user needs to specify the Arrhenius reaction model parameters (well-known for methane) and force FDS to employ finite-rate reaction rates. Unfortunately using finite-rate combustion increases the run time. Moreover, the FDS validation guide (66) does not include any premixed combustion test data. For these reasons it was decided to use diffusion flame burners, at least for the initial simulations described in this paper. The modified setup and the mesh are shown in Figure 38. The mesh size was 24 mm in the X and Y directions, and 25 mm in the Z direction. The interior space of the furnace was subdivided in eight zones, each containing 30 x 30 x 30 = 70,000 cells for a total of 216,000 cells.

The furnace gas temperature in simulated pool fire tests is monitored with four type K base-bead TCs located at 300 mm from the nearest furnace wall and approximately 300 mm below the lid insulation. FDS has the capability of modeling TCs so that response time and radiation errors can be accounted for. Although the wire diameter is known (~0.5 mm for 24 AWG wire), the bead size is subject to uncertainty. To assess the effect of bead size, three sets of TCs were included in the model with 1.0 mm, 1.5 mm, and 2.0 mm diameter beads, respectively.

Finally, it is necessary to specify several fuel parameters, more specifically (1) the fraction of the heat release rate that is lost to the surroundings in the form of radiation, and (2) the yields of products of incomplete combustion, i.e., CO and soot. From the chemical, convective and radiative heat of combustion values in Table A.39 of the Appendix to the 5th Edition of the SFPE Handbook of Fire Protection Engineering (67) it can be determined that the radiative fraction for well-ventilated methane fires is approximately equal to $\chi_r = 0.14$. This is on the low side of values for medium to large methane diffusion flames reported in the literature (68,69) and is a reasonable estimate of the radiative fraction for premixed methane flames. Although the furnace burner flames are modeled as diffusion flames, to improve the accuracy of the simulation, the values for the radiative fraction and the CO and soot yields should be representative of a premixed methane flame.

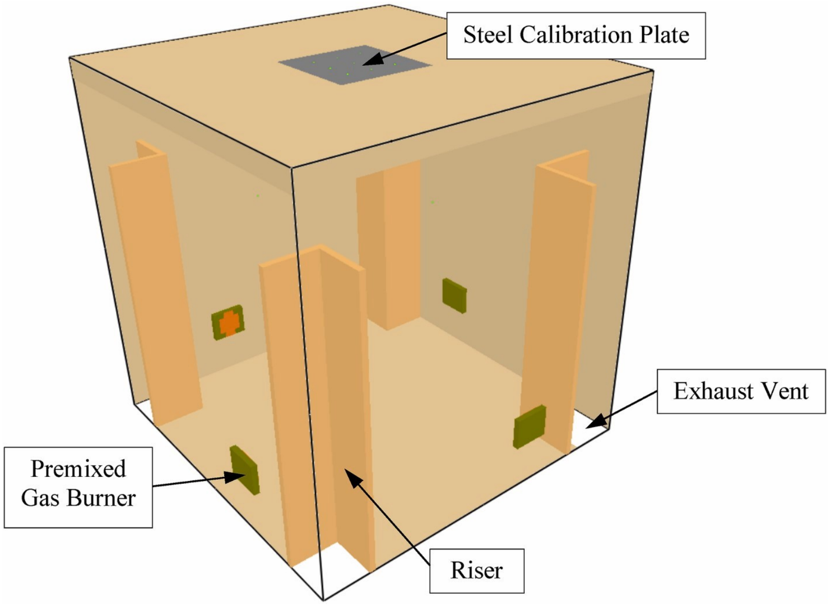

Figure 37. Smokeview rendering of the small horizontal furnace at SwRI

Table 39 in the SFPE handbook (67) gives the CO and soot yields (Y_{CO} and Y_s) for a large range of fuels but does not provide Y_{CO} and Y_s values for methane. However, Table 40 (70) indicates that Y_{CO} for a well ventilated ethane diffusion flame is smaller than 0.001 g/g and that Y_s for the same fuel is 0.002 g/g. Ethane (C_2H_6) is the next alkane in the series. It has a higher molar mass and is expected to produce more CO and soot than methane. It therefore seems reasonable in the simulation to assume $Y_{CO} = Y_s \approx 0$ for a premixed methane flame.

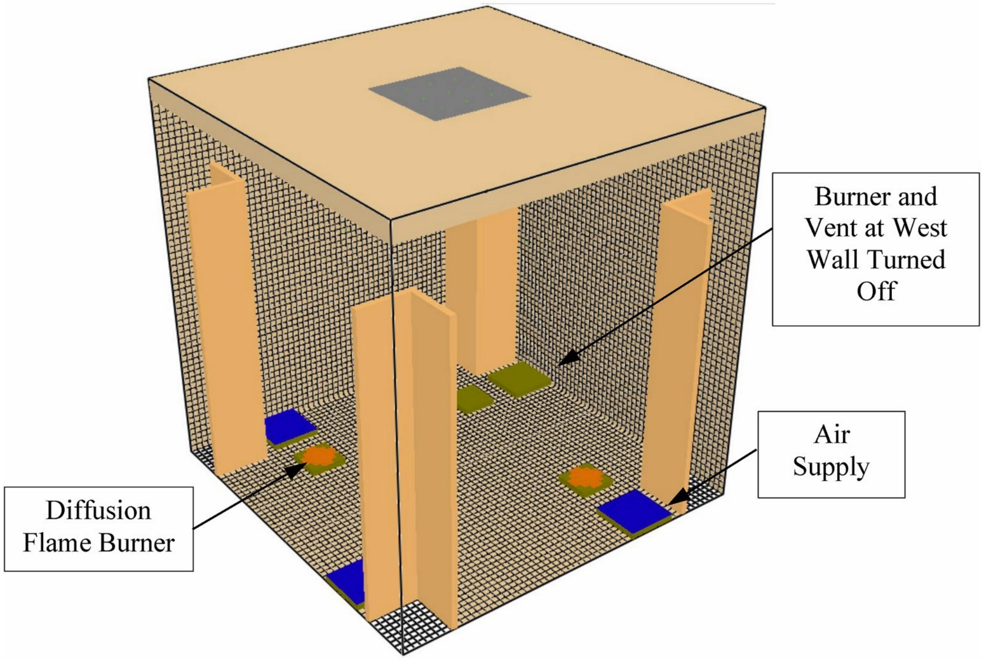

Figure 38. Alternative furnace setup with diffusion flame burners.

Thermal Properties

Three types of ceramic fiber insulation products were used in the construction of the furnace. The walls of the furnace shell are insulated with 203 mm Morgan Thermal Ceramics Z-Blok (density 149 kg/m^3). In addition, the walls, floor and ceiling are covered with one, two and three layers of 25 mm Morgan Thermal Ceramic Superwool (density 96 kg/m^3), respectively. The Morgan Thermal Ceramics KWL risers are made of Kaowool ceramic fiberboard with a wall thickness of 19 mm and density of 641 kg/m^3. A surface emissivity of 0.9 was assumed for all three products (71). The thermal property data for these three products were obtained from the Thermal Ceramics Product Data Book (72) and a collection of input data for fire modeling compiled by Gross (71). The thermal conductivity and specific heat values that were used in the present study are given as a function of temperature in Table 12 and Table 13 respectively. In some cases, the values at ambient temperature were obtained through extrapolation.

The thermal conductivity and specific heat of carbon steel of the calibrating base steel plate were obtained from Eurocode 3: Design of steel structures—Part 1–2: General rules—Structural fire design (39). The values used in the simulations are presented as a function of temperature in Table 5. For fire design of steel structures, a value of 7850 kg/m^3 is used for the density of carbon steel and 0.7 for its surface emissivity. The peak of the specific heat of steel at 735 °C corresponds to its austenitization (change of its crystal structure from ferrite to austenite).

Table 12. Thermal conductivity for ceramic fiber products (71,72).

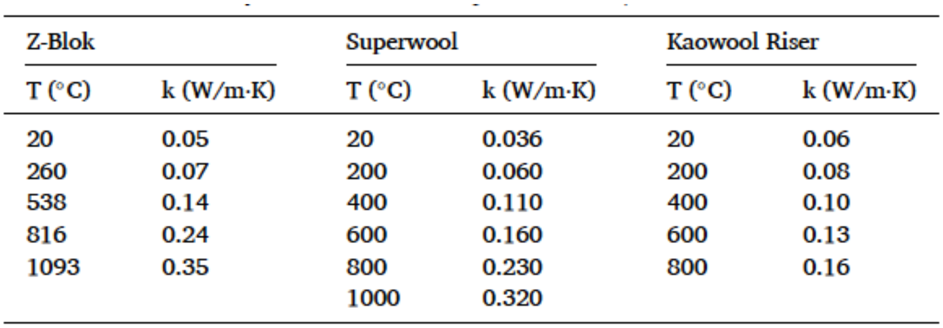

Z-Blok		Superwool		Kaowool Riser	
T (°C)	k (W/m·K)	T (°C)	k (W/m·K)	T (°C)	k (W/m·K)
20	0.05	20	0.036	20	0.06
260	0.07	200	0.060	200	0.08
538	0.14	400	0.110	400	0.10
816	0.24	600	0.160	600	0.13
1093	0.35	800	0.230	800	0.16
		1000	0.320		

Table 13. Specific heat for ceramic fiber products (71,72).

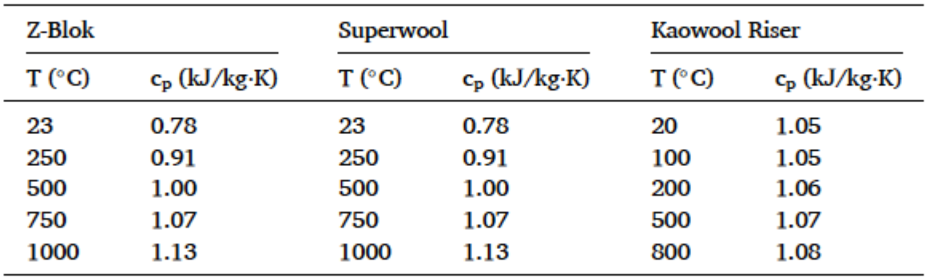

Z-Blok		Superwool		Kaowool Riser	
T (°C)	c_p (kJ/kg·K)	T (°C)	c_p (kJ/kg·K)	T (°C)	c_p (kJ/kg·K)
23	0.78	23	0.78	20	1.05
250	0.91	250	0.91	100	1.05
500	1.00	500	1.00	200	1.06
750	1.07	750	1.07	500	1.07
1000	1.13	1000	1.13	800	1.08

Table 14. Thermal conductivity and specific heat for carbon steel (73).

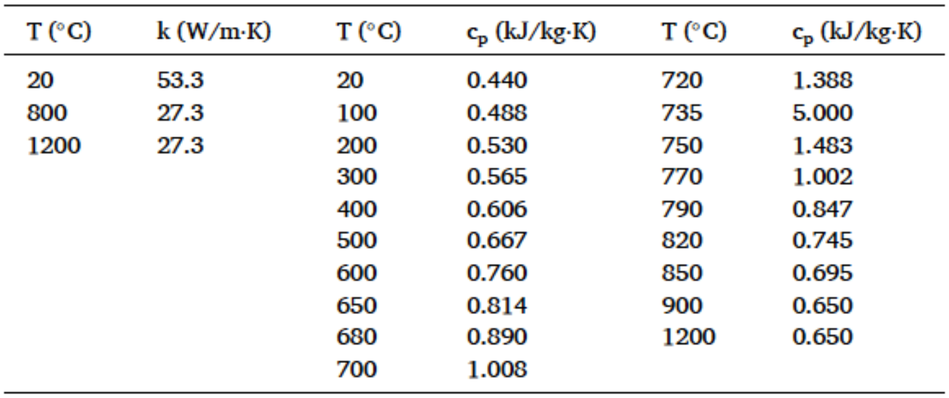

T (°C)	k (W/m·K)	T (°C)	c_p (kJ/kg·K)	T (°C)	c_p (kJ/kg·K)
20	53.3	20	0.440	720	1.388
800	27.3	100	0.488	735	5.000
1200	27.3	200	0.530	750	1.483
		300	0.565	770	1.002
		400	0.606	790	0.847
		500	0.667	820	0.745
		600	0.760	850	0.695
		650	0.814	900	0.650
		680	0.890	1200	0.650
		700	1.008		

Simulation Results

The purpose of modeling the calibration test with FDS was to determine the incident heat flux to the test specimen as a function of time during the first 15 min of a simulated pool fire test. It was assumed and later confirmed that the incident heat flux reaches a steady state after approximately 10 min of exposure. Consequently, if the initial heat flux profile and steady value are known, the performance of a material can be predicted from a heat conduction analysis without having to simulate the entire 100-min furnace test.

FDS calculates the temperature distribution in the test specimen by solving the 1-D heat conduction equation with the following boundary condition at the exposed surface of the specimen:

$$-k\frac{\partial T}{\partial x}\bigg|_{x=0} = \dot{q}_{net}'' = \varepsilon\left(\dot{q}_{inc}'' - \sigma T_s^4\right) + h_c\left(T_g - T_s\right) \tag{1}$$

where.

k = thermal conductivity of the test specimen (W/m·K);
T = temperature (K);
x = distance from the exposed surface of the specimen (m);
$\dot{q}_{net}''$ = net heat flux into the solid (kW/m^2);
ε = surface emissivity/absorptivity;
$\dot{q}_{inc}''$ = incident radiant heat flux (kW/m^2);
σ = Boltzmann constant ($5.67 \cdot 10^{-11}$ kW/K^4·m^2);
T_s = surface temperature (K);
h_c = convection coefficient (kW/m^2·K); and
$T_{s\backslash g}$ = gas temperature (K).

The emissivity, ε, is a known material characteristic and T_s is calculated by FDS. Consequently, to perform the calculations in step two values for $\dot{q}_{inc}$”, h_c, and T_g need to be supplied. Ideally, these values are constant, but in reality they vary as a function of time during the first 10 min due to the initial transient. At the start of a test the operator will supply more natural gas than needed to keep the furnace at the desired temperature of 825 °C to ensure that the target is reached in 2 min or less. However, as the furnace temperature approaches the desired value, the furnace operator will need to reduce the natural gas flow to avoid overshooting the target temperature. Soon thereafter a smaller increase may be needed followed by an even smaller decrease to keep the furnace temperature within tolerance. After a few oscillations only small and gradual natural gas flow adjustments will be needed to keep the furnace gases at the desired temperature for the remainder of the test. These variations can result in the fluctuations in temperature-time curve shown in Figure 33.

Twenty-four FDS simulations of one of the calibration tests (third one) were performed to identify a burner heat release rate (HRR) profile that would result in the same response of the calibration test as measured in the experiment. The 2–15 min average values of $\dot{q}_{inc}$”, h_c, and T_g for this simulation were equal to 71.7 kW/m^2, 10.5 W/m^2·K, and 790 °C, respectively.

Figure 39 compares the calculated (UST) to the measured (STC) unexposed surface temperatures of the calibration plate. The figure compares the calculated versus measured average, highest and lowest temperatures for the nine TC locations. Similar to the experimental results, the highest temperature is always at the center of the plate, while the lowest is in the corner or at the edge closest to the burner in the West wall, which was shut off in all calibration tests and subsequent CMF experiments. The predicted maximum temperature tracks the measured temperature well for the first 10 min. Later, however, the calculated temperature starts to slightly deviate and become higher.

Figure 39 shows that the difference between the highest and lowest is significantly smaller for the calculated temperatures. This is probably because FDS perform a 1-D calculation, which neglects lateral heat conduction and heat losses at the edges. FDS 6.7 has a 3-D option in beta that can be explored in future section. Alternatively, the incident radiant heat flux, convection coefficient and gas temperature at the exposed side opposite the nine unexposed surface TC locations calculated by FDS can be used together with a 3-D thermal analysis program such as ANSYS®-Mechanical or COMSOL Multiphysics® to perform a more accurate heat transfer calculation.

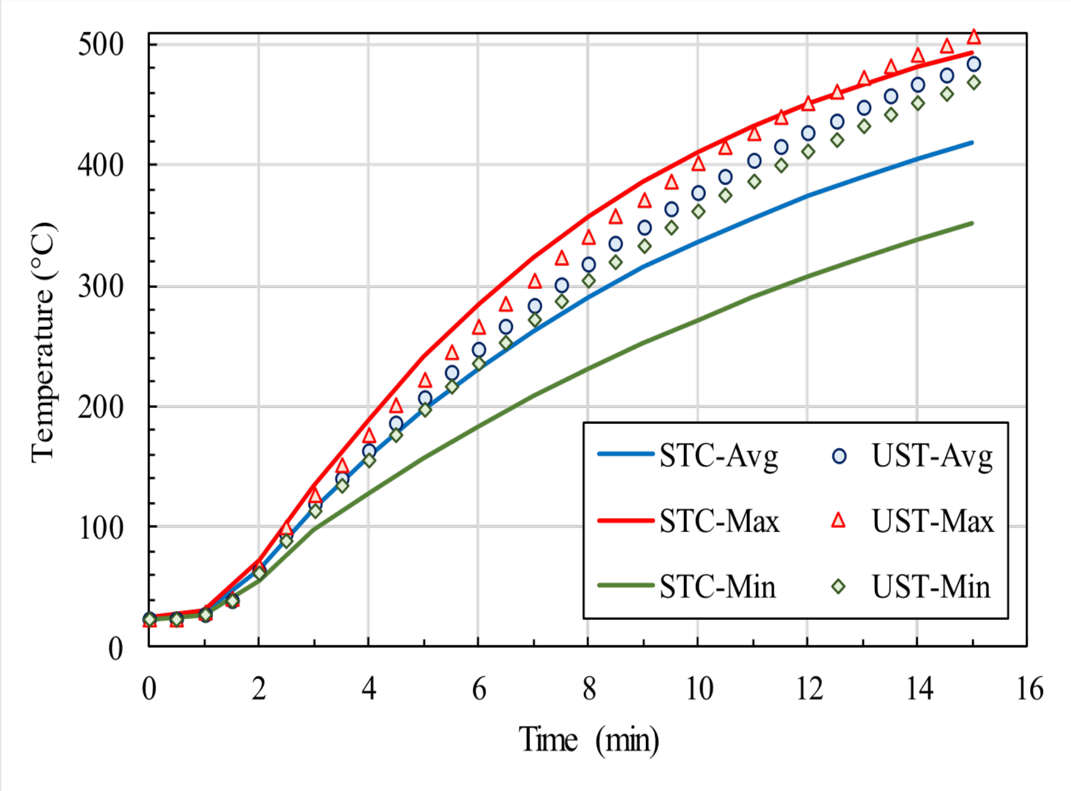

Figure 39. Best-fitting calculated vs. measured calibration plate temperatures (1-D model)

Numerical simulation of CMF response in simulated pool fire tests

FDS Model

FDS was utilized to predict the response of the CMF specimens in the first simulated pool fire tests with the gas phase calculations turned off, i.e., the heat conduction model in FDS with specified boundary conditions that are representative of the thermal environment in the furnace. The advantage of this approach is that it eliminates the need to simulate the furnace environment and reduces run times to simulate a 100 min long test from several days to a few minutes.

FDS determines the mesh for the solid phase based on the thickness and the thermal properties of the solid. Since FDS uses a 1-D heat conduction calculation it is not computationally intensive compared to the gas phase calculations, the mesh size is much smaller than the size of the spheres in the S–S CMF. FDS actually models a porous material as a solid with apparent thermal conductivity, specific heat and density. For a more comprehensive heat transfer calculation that considers the detailed porous structure, a thermal analysis software package such as COMSOL Multiphysics would be needed. The use of such a package would also allow for a 3-D analysis to account for the heat losses at the edges of the test specimen.

For the FDS heat conduction calculations it is assumed that the exposed side of the specimen is heated by convection and radiation according to Equation (1), with $\dot{q}_{inc}$”, h_c, and T_g ramping up from initial (0 for and h_c, and ambient temperature for T_g) to steady state values in 2 min and remaining at these values for the remainder of the test. The steady values were chosen based on the results of the FDS furnace simulations of: $\dot{q}_{inc}$” = 71.7 kW/m^2, h_c = 10.5 W/m^2·K, and T_g = 790 °C. The 35 °C difference between the steady gas temperature near the surface of the specimen and the average furnace TC temperature is partly due to radiation error (74,75), but also because the specimen surface is recessed into the insulated furnace lid by 80–100 mm. The latter may also explain the low convection coefficient.

To verify that Equation (1) and the chosen steady values are reasonably accurate characterization of the thermal exposure in the furnace, an FDS heat conduction calculation was first performed to predict the unexposed surface temperature in the third calibration test at the center of the steel plate, which was also the highest of the nine unexposed surface temperatures that were measured in the test. The result of the FDS heat conduction model calculations is shown in Figure 40. A comparison between Figure 39 and Figure 40 confirms the validity of the FDS heat conduction model calculations.

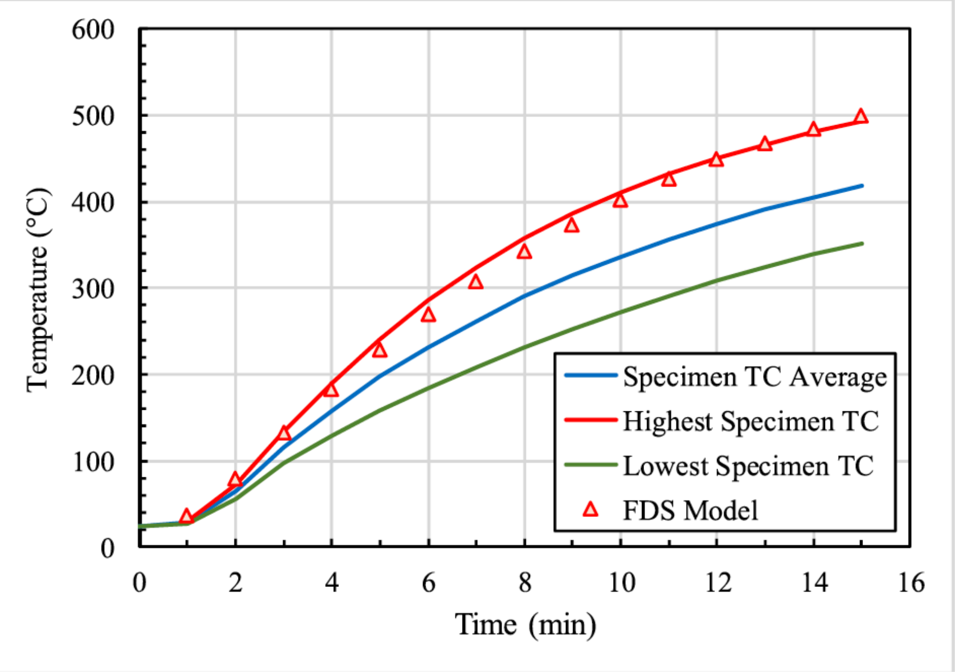

Figure 40. FDS heat conduction model vs. measured calibration plate temperatures.

Thermal Properties

The CMF density (2624 kg/m^3) was calculated from the measured mass (3.805 kg) and dimensions (approximately 30.2 x 30.2 x 1.6 cm) of the CMF test specimens. CMF heat conduction calculations were performed with three sets of thermal property values referred to as Base Case, Case a, and Case b. The thermal conductivity and specific heat are given in Table 15 and *Table 16*. For all cases a surface emissivity of 0.4 was assumed based on the recommendations in Annex C of Eurocode 3, Part 1–2 (73).

The thermal conductivity values of CMF at the specified temperatures are identical for the Base Case and Case a. The values at 300–600 °C (shaded cells in Table 15) are taken from our prior studies reported elsewhere (40). The values at the remaining temperatures were obtained from a slightly non-linear extrapolation consistent with the functional relationship between the thermal conductivity of stainless steel and temperature reported in Eurocode 3, Part 1–2 (73). The Base Case values for the specific heat of CMF at the specified temperatures are equal to the values for stainless steel recommended in Annex C of Eurocode 3, Part 1–2 (73). The Case a cp values are equal to 1.2 times the Base Case values. The 20% increase is based on the measured cp value at ambient temperature for 4 mm sphere stainless steel CFM of 0.551 kJ/kg·K reported in our prior studies (40).

The thermal properties for Case b are included in Table 15 and *Table 16* for comparison purposes. For Case b the CMF is specified in FDS as a material that consists of two components: (1) stainless steel with a density of 7850 kg/m^3 occupying approximately 33% of the volume, and (2) air with a density of 1.188 kg/m^3 accounting for the remaining 67% of the volume (40). FDS calculates the thermal properties as a volume-based (for k) or mass-based (for cp) weighted average of the properties for the components (76). Values for the latter are provided in Table 17.

Table 15. Thermal conductivity of CMF (73, 40 ,77).

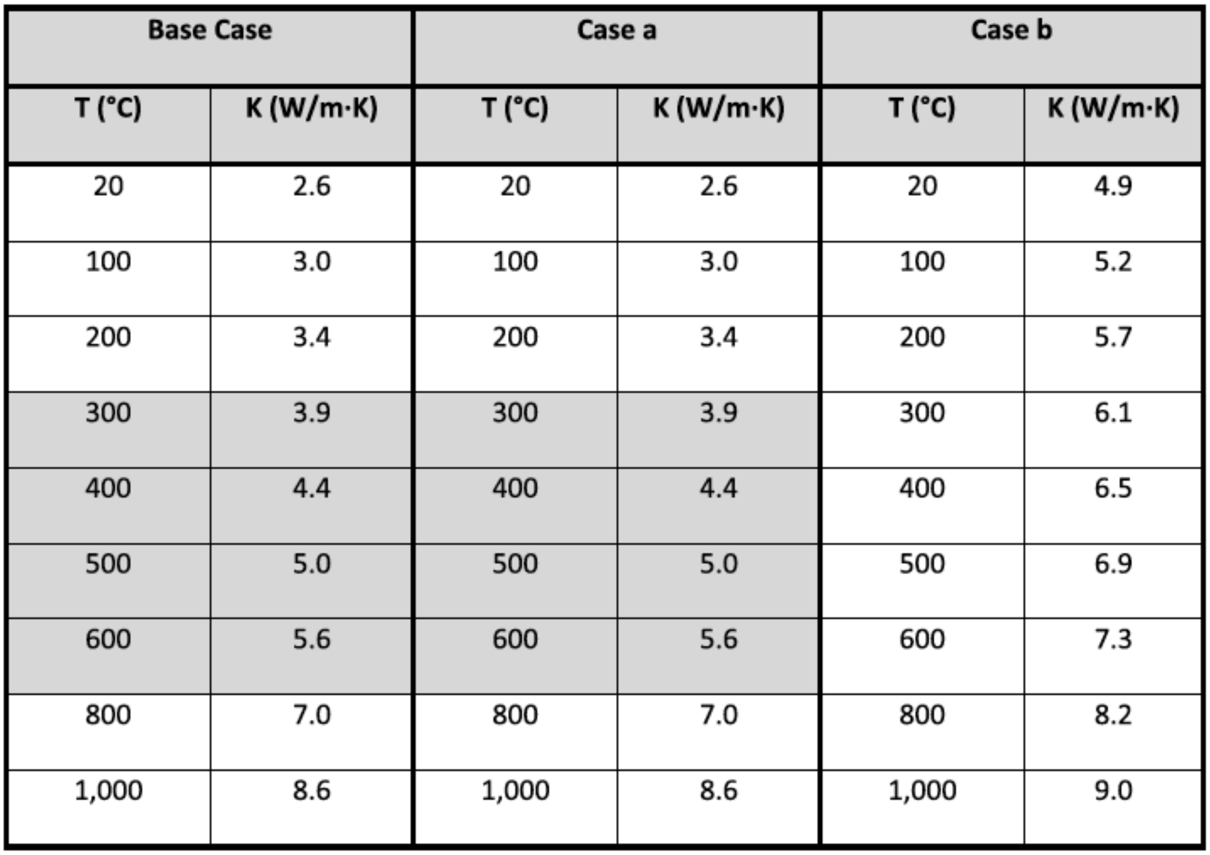

Base Case		Case a		Case b	
T (°C)	K (W/m·K)	T (°C)	K (W/m·K)	T (°C)	K (W/m·K)
20	2.6	20	2.6	20	4.9
100	3.0	100	3.0	100	5.2
200	3.4	200	3.4	200	5.7
300	3.9	300	3.9	300	6.1
400	4.4	400	4.4	400	6.5
500	5.0	500	5.0	500	6.9
600	5.6	600	5.6	600	7.3
800	7.0	800	7.0	800	8.2
1,000	8.6	1,000	8.6	1,000	9.0

Table 16. Specific heat of CMF (73,40 ,77).

Base Case		Case a		Case b	
T (°C)	c_p (kJ/kg·K)	T (°C)	c_p (kJ/kg·K)	T (°C)	c_p (kJ/kg·K)
20	0.455	20	0.546	20	0.455
100	0.475	100	0.570	100	0.475
200	0.495	200	0.594	200	0.495
300	0.511	300	0.613	300	0.511
400	0.524	400	0.629	400	0.524
500	0.534	500	0.641	500	0.534
600	0.542	600	0.650	600	0.542
700	0.549	700	0.659	700	0.549
800	0.556	800	0.667	800	0.556
900	0.564	900	0.677	900	0.564
1000	0.573	1000	0.688	1000	0.573

Table 17. Thermal properties of stainless steel (73) and air (77).

Stainless Steel			Air		
T (°C)	K (W/m·K)	c_p (kJ/kg·K)	T (°C)	K (W/m·K)	c_p (kJ/kg·K)
20	14.9	0.455	20	0.025	1.01
100	15.9	0.475	100	0.031	1.01
200	17.2	0.495	200	0.038	1.02
300	18.4	0.511	300	0.044	1.04
400	19.7	0.524	400	0.050	1.07
500	21.0	0.534	500	0.056	1.09
600	22.2	0.542	600	0.061	1.12
800	24.7	0.556	800	0.070	1.15
1000	27.3	0.573	1000	0.079	1.18

Simulation Results (1-D Model)

Figure 41 compares the unexposed surface temperatures from the FDS heat conduction calculations for the three cases to the temperatures measured at the center of the unexposed surface in the three simulated pool fire tests that were conducted on the CMF specimens. There is very little difference between the three predictions. All cases significantly overestimate the unexposed surface temperature measured in the simulated pool fire tests. More importantly, the heat conduction calculations predict that the CMF specimen would exceed the 427 °C failure threshold, while in actuality all three tests were successful.

The FDS heat conduction calculations for the three cases were performed with thermal property values that are consistent with measurements and data reported in the literature. Small changes, e.g., to account for the specific type of stainless steel, the contact resistance between the CMF specimen and the steel plate, and even the lateral heat conduction and heat losses at the edges of the test specimen are not likely to improve the agreement with the experimental data very much.

There is, however, one material property that may have a significant effect and has not been examined, and that is the surface emissivity. The value of 0.4 recommended in the Eurocode for stainless steel is likely to be on the high side, i.e., a value that leads to conservative estimates of the performance of a stainless steel structure in a fire. Values for the emissivity of polished steel as low as 0.07 have been reported in the literature (78). A sensitivity study was performed with the Base Case thermal conductivity and specific heat and lower surface emissivity. Good agreement was found between the calculated and measured temperatures for an emissivity of 0.13, as shown in Figure 42. This case is referred to as Case c. An attempt was made at measuring the emissivity of the SS-CMF to verify that 0.13 is a realistic value. These measurements are discussed in the next section.

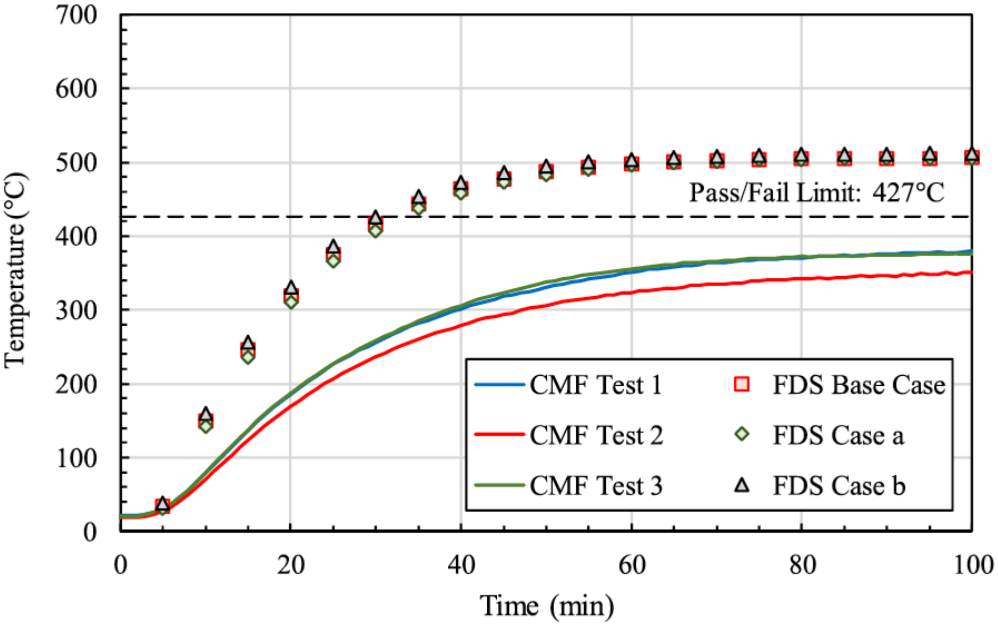

Figure 41. Calculated versus measured unexposed SS-CFM surface temperatures (ε = 0.4).

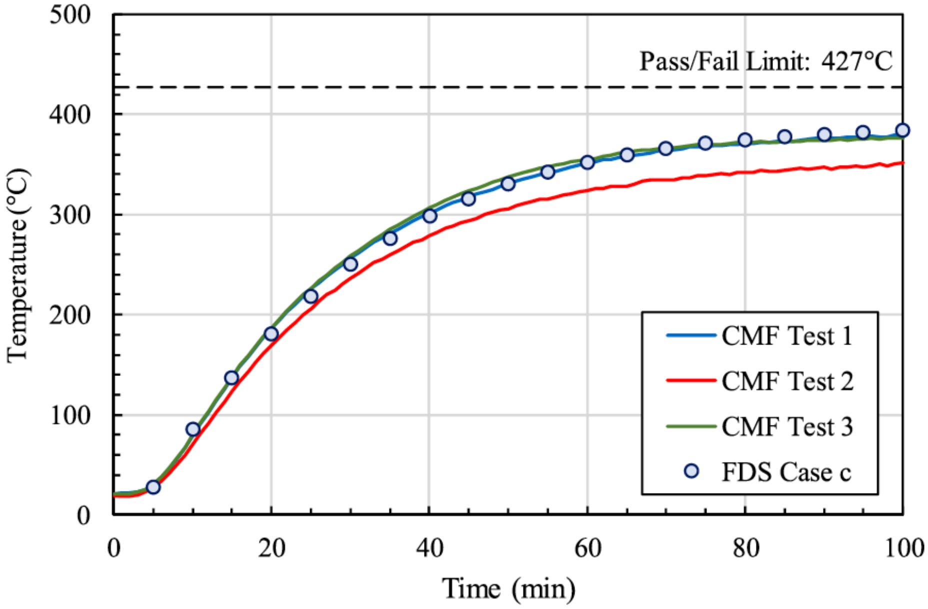

Figure 42. Calculated versus measured SS-CFM surface temperatures (ε = 0.13).

Surface Emissivity Measurements

Two sets of emissivity measurements were conducted on a 15 x 10 x 1.6 cm SS-CMF specimen with similar properties as the simulated pool fire test panels. Prior to the first set of measurements, the surface of the specimen had a ground mirror-like appearance. For the second set, it had a duller appearance, presumably due to a slight oxidation at the surface resulted from the first test exposure. The second set was performed to determine whether the emissivity is affected by surface oxidation. The same procedure was used for both sets of measurements. The CMF was instrumented with an Inconel-sheathed TC to measure the surface temperature at the center of the specimen. The instrumented specimen was heated in a muffle furnace. When the specimen temperature reached a steady state, the oven door was opened and an IR camera was used with assumed target surface emissivity set to 1.0 to obtain a video recording of the temperature distribution over the front face of the specimen as it was cooling down. The actual emissivity was then calculated from the ratio of the emitted heat flux calculated based on the IR camera and TC temperature readings.

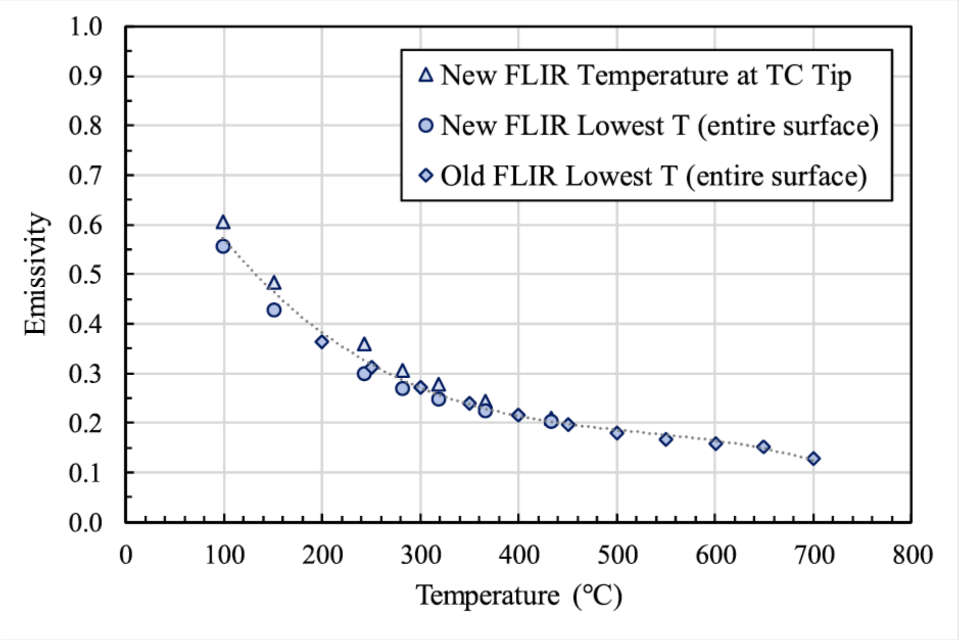

Figure 43. Results of emissivity measurements on SS-CMF panel.

Figure 43 shows the emissivity measurements as a function of the TC temperature for the first set (based on the IR camera temperature at the TC tip and the lowest temperature over the specimen surface) and the second set (based on the lowest IR camera temperature over the 11 specimen surface). As can be seen in this figure and considering the fact that the furnace temperature rises to 825 °C in 2 min, and the surface temperature quickly rises to 600–700 °C, assuming a surface emissivity 0.13 is reasonable. However, in the FDS calculations a constant emissivity is assumed. Prior to the torch fire modeling, it will be necessary to verify the accuracy of the emissivity measurements and to quantify the uncertainties introduced by not specifying an emissivity that varies with temperature.

Uncertainty assessments

This section describes the uncertainty assessment for the measured and calculated unexposed surface temperatures in the calibration and simulated pool fire tests on the S-S CMF specimens. The assessment is based on the procedure described in ASTM E2536, *Standard Guide for Assessment of Measurement Uncertainty in Fire Tests*. ASTM E2536 is based on ISO/IEC Guide 98-3, also referred to as the GUM (Guide on Uncertainty of Measurements). The ASTM guide specifically describes concepts and calculation methods to assess the uncertainty of measurements obtained in fire tests. The uncertainty assessment for the unexposed surface temperature measurements and calculations are discussed here.

ASTM E2536:

The value of a measurand is generally not obtained from a direct measurement, but is determined as a function, f, from N input quantities; X_1, X_2, …, X_N:

$$\mathrm{Y} = \mathrm{f}(\mathrm{X}_1, \mathrm{X}_2, \dots, \mathrm{X}_\mathrm{N}) \qquad [2]$$

where

Y = true value of the measurand;

f = functional relationship between measurand and input quantities; and

X_i = true values of the input quantities (i = 1 … N.)

The input quantities may be categorized as:

- quantities whose values and uncertainties are directly determined from single or repeated observation; or
- quantities whose values and uncertainties are brought into the measurement from external sources such as reference data obtained from handbooks.

An estimate of the value of the measurand, y, is obtained from Equation 1 using input estimates x_1, x_2, …, x_N for the values of the N input quantities:

$$\mathrm{y} = \mathrm{f}(\mathrm{x}_1, \mathrm{x}_2, \dots, \mathrm{x}_\mathrm{N}) \qquad [3]$$

The standard uncertainty of y is obtained by appropriately combining the standard uncertainties of the input estimates $x_{1,}$ $x_{2,\dots,}$ x_N. If all input quantities are independent, which is often the case, the combined standard uncertainty of y is given by:

$$\mathrm{u_c(y)} = \sqrt{\sum_{\mathrm{i}=1}^{\mathrm{N}} \left[\left.\frac{\partial \mathrm{f}}{\partial \mathrm{X_i}}\right|_{\mathrm{x_i}}\right]^2 \mathrm{u}^2\,(\mathrm{x_I})} \equiv \sqrt{\sum_{\mathrm{i}=1}^{\mathrm{N}} [\mathrm{c_i}.\mathrm{u}(\mathrm{x_i})]^2} \qquad [4]$$

where

u = standard uncertainty;

u_c = combined standard uncertainty; and

$c_{i,}$ = sensitivity coefficients.

The standard uncertainty of an input estimate x_i is obtained from the statistical distribution of possible values of the input quantity X_i. There are two types of evaluations depending on how the distribution of possible values is obtained.

A type A evaluation of standard uncertainty of x_i is based on the frequency distribution, which is estimated from a series of n repeated observations $x_{i,k}$ (k = 1 … n).

$$u(x_i) \approx \sqrt{s^2(\bar{x}_i)} = \sqrt{\frac{s^2(x_i)}{n}} = \sqrt{\frac{\sum_{k=1}^{n}\left(x_{i,k}-\bar{x}_i\right)^2}{n(n-1)}} \quad \text{with} \quad \bar{x}_i \equiv \frac{\sum_{k=1}^{n} x_i}{n} \qquad [5]$$

A type B evaluation of standard uncertainty of x_i is not based on repeated measurements but on an *a priori* frequency distribution. In this case the uncertainty is determined from previous measurements, experience or general knowledge, manufacturer specifications, data provided in calibration certificates, uncertainties assigned to reference data taken from handbooks, etc.

Often the uncertainty of an input quantity is expressed in the form of upper and lower limits. Usually there is no specific knowledge about the possible values of X_i within the interval and one can only assume that it is equally probable for X_i to lie anywhere in it. Often the corresponding rectangular distribution is symmetric with respect to its best estimate x_i. The standard uncertainty in this case is given by:

$$u(x_i) = \frac{\Delta X_i}{\sqrt{3}} \qquad [6]$$

where

ΔX_i = half-width of the interval.

Equation 4 is referred to as the law of propagation of uncertainty and based on a first-order Taylor series approximation of $Y = f(X_1, X_2, \ldots, X_N)$. When the nonlinearity of f is significant, higher-order terms must be included.

The combined standard uncertainty in Equation 4 is usually multiplied by a coverage factor to raise the confidence level. A multiplier of 2 is often used, which corresponds to a confidence level of approximately 95 %.

Uncertainty of Unexposed Surface Temperature Measurements

It is not possible to calculate the uncertainty of the measured unexposed surface temperature according to Equation 4, primarily because the functional relationship between the measurand and the input quantities (f in Equation 2) is unknown. This limitation of ASTM E2536 is discussed in section X.2 of the guide.

Theoretically, it would be possible to estimate the uncertainty of the unexposed surface temperature measurements from a series of repeat experiments based on Equation 5. However, fire resistance tests are expensive and conducting a statistically significant number of repeat experiments is cost-prohibitive. The maximum temperatures from repeat testing given in Table 2 provide an indication of the uncertainty of the unexposed surface temperature measurements in the simulated pool fire tests. The maximum temperatures measured in Test 1 and Test 3 are very close but the value is approximately 7% lower for Test 2.

ASTM E119 is the furnace fire test standard used in the U.S. to determine the fire resistance rating of building elements and assemblies. The precision and bias section in the standard reports a repeatability standard deviation of 0.6 minutes (or approximately 1% of the average failure time) for a 3 × 3 m loaded wall assembly that consists of a light steel-stud frame protected with one layer of 16 mm Type X gypsum board on both sides. The reported repeatability is based on three tests that were performed according to the ASTM E119 standard in a single laboratory.

The time for the highest unexposed temperature to reach 181°C (one of the end-point criteria specified in ASTM E119) recorded in S-S CMF Test 1 and Test 3 was 19 min 18 s and 19 min 20 s, respectively. This is well within the expected repeatability of 1%. However, in Test 2 the highest unexposed surface temperature did not reach 181°C until 2 minutes later, which is about 10% of the measured value.

Uncertainty of the Calculated Unexposed Surface Temperatures

The unexposed surface temperature in the calibration test is a function of ten input quantities. These input quantities are categorized into three groups:

- Thermal exposure input quantities:

    - X1 = furnace gas temperature, T_g (K);
    - X2 = furnace side convection coefficient, $h_{c,exp}$ (kW/m^2·K); and
    - X3 = incident radiant heat flux, $\dot{q}''_{inc}$ (kW/m^2).
- Unexposed side input quantities:
    - X4 = initial and ambient temperature, T_a (K); and
    - X5 = unexposed side convection coefficient, $h_{c,unexp}$ (kW/m^2·K).
- Carbon steel input quantities:
    - X6 = surface emissivity, ε_{cst};
    - X7 = thermal conductivity, k_{cst} (W/m·K);
    - X8 = density, ρ_{cst} (kg/m^3);
    - X9 = specific heat, $c_{p,cst}$ (kJ/kg·K); and
    - X10 = thickness, δ_{cst} (m).

For the unexposed temperature in the simulated pool fire tests, the following five input quantities need to be added:

- Composite Metal Foam input quantities:
    - X11 = surface emissivity, ε_{cmf};
    - X12 = thermal conductivity, k_{cmf} (W/m·K);
    - X13 = density, ρ_{cmf} (kg/m^3);
    - X14 = specific heat, $c_{p,cmf}$ (kJ/kg·K); and
    - X15 = thickness, δ_{cmf} (m).

Estimates of the uncertainties of the 15 input parameters are provided in Table 18. The fourth column contains the input quantity values that were used in the FDS heat conduction calculations reported in this study. For some input quantities, these values are slightly different from the mid-point values in the next column as the uncertainty range was not symmetrical around the value used in the simulation or the average for the three SS-CMF tests was used instead of the value for one of the three tests. A brief discussion of how these uncertainty estimates were obtained follows.

Table 18. **Standard Uncertainties or Ranges of the Input Quantities.**

Input Quantity	Symbol	Unit	Base Value	Mid-Point Value	Uncertainty or Range
X_1	T_g	°C	790	790	± 1.31°C
X_2	$h_{c,exp}$	$W/m^2 \cdot °C$	10.5	10.5	negligible
X_3	$\dot{q}''_{inc}$	kW/m^2	71.7	71.7	± 0.5 kW/m^2
X_4	T_a	°C	24 /22 *	24 /22 *	± 1.31°C
X_5	$h_{c,unexp}$	$W/m^2 \cdot °C$	7.0	7.0	negligible
X_6	ε_{cst}		0.7	0.7	0.6-0.8
X_7	k_{cst}	W/m·K	Table 5	Table 5	(Table 5)×(0.8-1.2)
X_8	ρ_{cst}	kg/m^3	7850	7840	7800-7880
X_9	$c_{p,cst}$	kJ/kg·K	Table 5	(Table 5) ×1.08	(Table 5) ×(1.00-1.16)
X_{10}	δ_{cst}	m	0.15875	0.01626	0.014859-0.017653 m
X_{11}	ε_{cmf}		0.13	0.13	± 0.01
X_{12}	k_{cmf}	W/m·K	Table 6	Table 6	± 5%
X_{13}	ρ_{cmf}	kg/m^3	2624	2574	2524-2624 kg/m^3
X_{14}	$c_{p,cmf}$	kJ/kg·K	Table 7	(Table 7) ×1.05	(Table 7)×(1.0-1.1)
X_{15}	δ_{cmf}	m	0.01575	0.01585	0.01580-0.01590

* First value from calibration test/Second value from SS-CMF test

- T_g was determined by adjusting the heat release rate profile of the furnace burners until the measured and calculated furnace TC temperatures matched. Consequently, the uncertainty of T_g was estimated as the measurement uncertainty of the Type K thermocouples, which was taken from the example in ASTM E2536.

- $h_{c,exp}$ was determined from the FDS furnace simulations of the calibration test. The uncertainty of this input quantity is due to the uncertainty in the furnace temperature measurement and was negligible.

- The uncertainty of $\dot{q}''_{inc}$ was assumed to be due to the uncertainty of the radiation temperature. The latter was assumed equal to that for T_g.

- T_a was determined from the unexposed surface thermocouple data for each test. Its uncertainty is therefore the same as the measurement uncertainty for T_g.

- The same value for $h_{c,unexp}$ was used for heat conduction calculations as for the furnace simulations. Its uncertainty was therefore negligible.

- The uncertainty ranges for the thermal properties of the carbon steel (ε_{cst}, k_{cst}, ρ_{cst} and $c_{p,cst}$) were based on the ranges of generic values at ambient temperature reported in textbooks and on web sites.

- The uncertainty of δ_{cmf} is based on allowable tolerances for the thickness of steel plates for pressure vessels specified in ASTM A20/A20M.

- The measurement uncertainty of ε_{cmf} was determined using Equation 4 and the uncertainties of the IR camera and thermocouple temperature measurements.

- The uncertainty of k_{cmf} is reported in 40.

- The uncertainty range of ρ_{cmf} is based on the density range of the three tested CMF specimens.

- The uncertainty range for $c_{p,cmf}$ is based on the range of generic values at ambient temperature for stainless steel reported in textbooks and on web sites.

- The uncertainty of δ_{cmf} is based on the measurement uncertainty for a CMF specimen used in Test 1.

Two approaches were used to estimate the uncertainty of the unexposed surface temperature predictions for the calibration and simulated pool fire tests. In the first approach, the uncertainty of the unexposed temperature predictions was calculated according to Equation 4. The sensitivity coefficients were estimated numerically based on the change of the calculated unexposed surface temperature for a small change of each of the input quantities. The second approach involved a Monte Carlo simulation. The simulation consisted of 1,000 realizations. In each realization, all input quantities were varied randomly according to a normal or uniform distribution.

For each approach, two sets of calculations were performed. In the “full” set, the uncertainties of the thermal properties of the steel were included. The calculated combined uncertainty from the full calculations should be used when the calibration or test specimen is exposed to a specified heat flux, but the properties and exact thickness of the steel are unknown. However, because the heat flux in the present study was determined so that the calculated unexposed surface temperature in the calibration test matches the measured temperature, it is not necessary to account for the uncertainties of the thermal properties and thickness of the steel. For this reason, a second set of “reduced” calculations were performed. The results of the uncertainty calculations are given in *Table 19* and *Table 20* for the calibration test and simulated pool fire test, respectively. The temperature in the second column is the calculated unexposed surface temperature at the specified time with input quantities equal to the mid-point values.

The results in *Table 19* for the full calculations indicate that the expanded uncertainty of the unexposed surface temperature at 12-14 minutes can be as high as ± 46.6°C. It is notable that the values in *Table 19* are the standard uncertainties, which correspond to one standard deviation. The expanded uncertainty elevates the confidence level to 95% and is equal to about two times the standard uncertainty. As such the highest value for the standard uncertainty between 12 and 14 minutes (23.3 C) will result in an expanded uncertainty of ± 46.6°C. This implies that the thermal exposure conditions for the simulated pool fire tests, which are based on the furnace settings in the calibration test that cause at least three of nine unexposed surface TCs to reach 427°C or higher at 13 minutes ± 1 minutes, can vary significantly in severity due to variations in the thermal properties, density and thickness of the steel plate. Moreover, *Table 20* shows that the highest unexposed surface temperature detected in all three S-S CMF panels in the simulated pool fire test at 100 minutes is more than four times the “full” standard uncertainty and over six times the “reduced” standard uncertainty below the 427°C pass/fail limit. Consequently, it can be concluded that the S-S CMF specimen meets the acceptance criteria for the simulated pool fire test in 49 CFR 179 Appendix B by a large margin and is expected to pass with near certainty if the test were to be reproduced in a different laboratory.

Table 19. Calculated Combined Standard Uncertainties for Calibration Test.

Time (min)	**$T_{s,\ unexposed}$ (°C)**	**Full u_c (°C)**		**Reduced u_c (°C)**	
		Eq. 4	**MC***	**Eq. 4**	**MC***
0	24.0	± 1.3	± 1.1	± 1.3	± 1.1
1	36.4	± 1.8	± 1.7	± 1.3	± 1.1
2	74.8	± 4.9	± 5.0	± 1.2	± 1.1
3	124.1	± 9.1	± 9.2	± 1.3	± 1.1
4	169.8	± 12.7	± 12.8	± 1.3	± 1.2
5	212.1	± 15.8	± 15.9	± 1.4	± 1.3
6	251.3	± 18.4	± 18.5	± 1.6	± 1.4
7	287.5	± 20.4	± 20.5	± 1.7	± 1.4
8	320.8	± 21.9	± 22.0	± 1.8	± 1.5
9	351.2	± 22.9	± 22.9	± 1.8	± 1.6
10	378.9	± 23.4	± 23.5	± 1.9	± 1.6
11	403.9	± 23.5	± 23.6	± 1.9	± 1.7
12	426.3	± 23.2	± 23.3	± 2.0	± 1.7
13	446.3	± 22.6	± 22.8	± 2.0	± 1.7
14	464.2	± 21.9	± 22.0	± 2.0	± 1.7
15	480.0	± 21.0	± 21.2	± 2.0	± 1.7

* MC = Results for Monte-Carlo Simulation

Table 20. Calculated Combined Standard Uncertainties for Simulated Pool Fire Test.

Time (min)	$T_{s,\ unexposed}$ (°C)	**Full u_c (°C)**		**Reduced u_c (°C)**	
		Eq. 4	**MC***	**Eq. 4**	**MC***
0	22.0	± 1.3	± 1.1	± 1.3	± 1.1
5	58.8	± 2.6	± 2.1	± 1.8	± 1.5
10	110.5	± 5.2	± 4.9	± 3.3	± 2.9
15	154.9	± 7.3	± 7.0	± 4,6	± 4.3
20	193.3	± 8.9	± 8.7	± 5.8	± 5.4
30	254.3	± 10.7	± 10.5	± 7.3	± 6.9
40	298.2	± 11.3	± 11.1	± 8.1	± 7.7
50	328.7	± 11.2	± 11.0	± 8.4	± 7.9
60	349.5	± 10.9	± 10.6	± 8.3	± 7.8
70	363.5	± 10.6	± 10.4	± 8.2	± 7.5
80	372.8	± 10.5	± 10.2	± 7.9	± 7.3
90	378.9	± 10.4	± 10.2	± 7.7	± 7.1
100	382.9	± 10.4	± 10.2	± 7.6	± 6.8

* MC = Results for Monte-Carlo Simulation

Based on the experimental and modeling results as well as the uncertainty studies, the 15.9 mm thick steel-steel composite metal foams tested as novel insulation system met the acceptance criteria for the simulated pool fire test in 49 CFR 179 Appendix B by a large margin and is expected to pass with near certainty if the test were to be reproduced in a different laboratory. Furthermore, the successful performance of S-S CMF in the simulated pool fire test (described in 49 CFR Part 179) can be attributed to its improved thermal conductivity due to the presence of air bubbles inside along with its low surface emissivity. To complete the full test requirements of CFR Part 179 App. B, the material will need to be tested to the torch-fire exposure in duplicate.

8.5 COMSOL 3-D Thermal Analysis

Previous attempts to model the simulated pool fire test consisted of two steps. The first step involved using Fire Dynamics Simulator (FDS) to model the test furnace and determine the thermal exposure conditions from FDS simulations of a calibration test on a steel plate. In the second step, the thermal exposure conditions from the first step were used as boundary conditions in 1-D heat transfer calculations to predict the temperature at the center of the unexposed surface in a simulated pool fire test of an SS-CMF specimen. The results are reported in a previous section and published in a journal paper (61). Although in the previous work good agreement was obtained for the simulated pool fire test between the calculated and measured temperatures at the center of the unexposed surface, there was a discrepancy between the calculated and measured unexposed surface temperature distribution for the calibration test.

This part of the report describes a series of 3-D heat transfer calculations using the finite element software COMSOL Multiphysics®. The purpose of the COMSOL calculations is to determine up to what extent the aforementioned discrepancy can be explained by the fact that FDS neglects lateral heat conduction due to heat losses at the perimeter of the exposed area. To gauge the effect of the latter, the COMSOL model assumes that the heat flux at the exposed surface of the specimen is uniform. The 3-D heat transfer calculations show that lateral heat conduction indeed needs to be included in the model to improve the accuracy of the predicted temperature distribution but that the non-uniformity of the heat flux in the test also should be accounted for.

Approach

A two-step process was used to predict the performance of the S-S CMF specimens. The first step involved a numerical simulation of the final calibration test to determine the incident heat flux to the test specimen, which rises from zero at the start of the test to a relatively steady value after approximately 10 min of heating. The second step consisted of a conduction heat transfer analysis to calculate the temperature at the center of the unexposed side of the S-S CMF test specimen and to determine whether the pass/fail limit is or is not exceeded during the 100-min thermal exposure.

Step 1: Establishing Thermal Exposure Conditions in the Calibration Test

In the first step version 6.7 of FDS (62) was used to model the fire resistance of the furnace in which the simulated pool fire test was conducted. Details of the FDS model development and the results of the calculations are described elsewhere (61) and in prior section of this report. It was necessary to model the furnace environment because the test procedure defines the thermal exposure conditions in terms of the furnace gas temperature instead of incident heat flux to the specimen surface. Although the incident heat flux to the exposed side of the test specimen, which was needed for the heat conduction analysis in step two, depends on the gas temperature, there are other factors that needed to be considered such as the furnace wall temperature, direct flame radiation, etc. Hence the need to model the furnace is obvious. Because the natural gas flow to the burners during the calibration tests was not measured, the flow had to be determined indirectly, using an iterative process to find the flow rate that results in calculated calibration specimen and furnace gas temperatures that match the measured temperatures.

FDS calculates the temperature distribution in the test specimen by solving the 1-D heat conduction equation[1] with the following boundary condition at the exposed surface of the specimen:

$$-k_{exp}\frac{\partial T}{\partial x}\bigg|_{x=0} = \dot{q}''_{net,exp} = \varepsilon_{exp}\left(\dot{q}''_{inc,exp} - \sigma T^{4}_{s,exp}\right) + h_{c,exp}\left(T_g - T_{s,exp}\right) \qquad (7)$$

where

k_{exp} = thermal conductivity of the solid at the fire-exposed side (W/m·K);

T = temperature (K);

x = distance from the fire-exposed surface of the test specimen (m);

$\dot{q}''_{net,exp}$ = net heat flux into the solid at the fire-exposed surface (kW/m2);

ε_{exp} = surface emissivity/absorptivity of the fire-exposed surface (0.13 for S-S CMF);

$\dot{q}''_{inc,exp}$ = incident radiant heat flux at the fire-exposed surface of the specimen (kW/m2);

σ = Boltzmann constant (5.67·10-11 kW/K4·m2);

$T_{s,exp}$ = temperature at the fire-exposed surface of the specimen (K);

$h_{c,exp}$ = convection coefficient at the fire-exposed specimen surface (kW/m2·K); and

T_g = gas temperature at the fire-exposed surface of the specimen (K);

The thermal conductivity, k_{exp} , and emissivity, εexp, are known material characteristics (see below) and Ts is calculated by FDS. Consequently, to perform the calculations in step two it was necessary to obtain the best-fitting values for $\dot{q}''_{inc,exp}$, $h_{c,exp}$, and T_g in step one. In step two it was assumed that these values are constant after the 2-min transient. In reality they may vary as a function of time during the first 10 min because the operator initially supplies more natural gas than needed to keep the furnace at the desired temperature of 825°C and subsequently has to make flow adjustments to avoid significantly over- or undershooting the target temperature until a relatively steady state is reached.

---

[1] FDS 6.7 has a 3-D option in beta (62) that was not used but could be explored.

Twenty-four FDS simulations of the third calibration test were performed to identify a burner heat release rate (HRR) profile that optimizes agreement between the calculated and measured temperatures at the center of the unexposed surface of the steel plate. The 2-15 min average values of $\dot{q}''_{inc,exp}$, $h_{c,exp}$, and T_g for the best-fitting HRR profile are equal to 71.7 kW/m2, 10.5 W/m2·K, and 790°C, respectively.

Figure 44 compares the calculated versus measured average, highest and lowest temperatures for the nine TC locations. The highest temperature is always recorded at the center of the plate, while the lowest is in a corner closest to the burner in the West furnace wall, which was shut off in all calibration tests and subsequent SS-CMF experiments. Initially, the predicted maximum temperature somewhat under-predicts the center temperature and slightly exceeds the measured center temperature after 12 min.

Figure 44 also shows that the difference between the highest and lowest temperature is significantly smaller for the calculations. A possible explanation is that FDS performs a 1-D calculation, which neglects lateral heat conduction and heat losses at the perimeter of the exposed area of the steel plate. A 3-D thermal analysis was conducted with the finite element program COMSOL Multiphysics® to test the validity of this hypothesis. The results of this analysis are discussed later in this chapter.

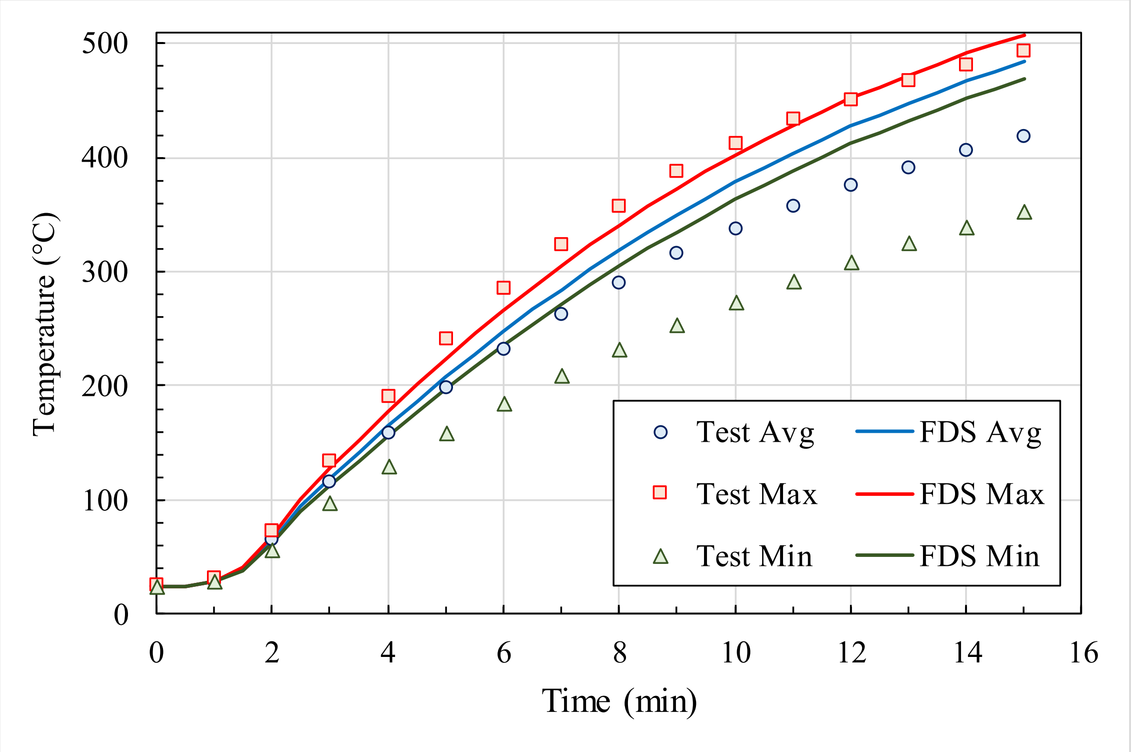

Figure 44. FDS vs. Measured Unexposed Surface Temperatures for the Third Calibration Test (61).

Step 2: Numerical Simulations of SS-CMF Simulated Pool Fire Test

The conduction heat transfer model in FDS, which is a sub-model of the pyrolysis model, was used for step two. FDS allows the user to significantly accelerate the conduction heat transfer analysis by disabling the time-consuming gas phase calculations, which are not needed when the thermal boundary conditions are known. Figure 45 compares the calculated and measured temperatures at the center of the unexposed surface of the specimen for the first simulated pool fire test. The model results indicate that the successful performance of SS-CMF can be explained by the improved thermal conductivity due to the presence of air bubbles inside and low surface emissivity of the material (0.13).

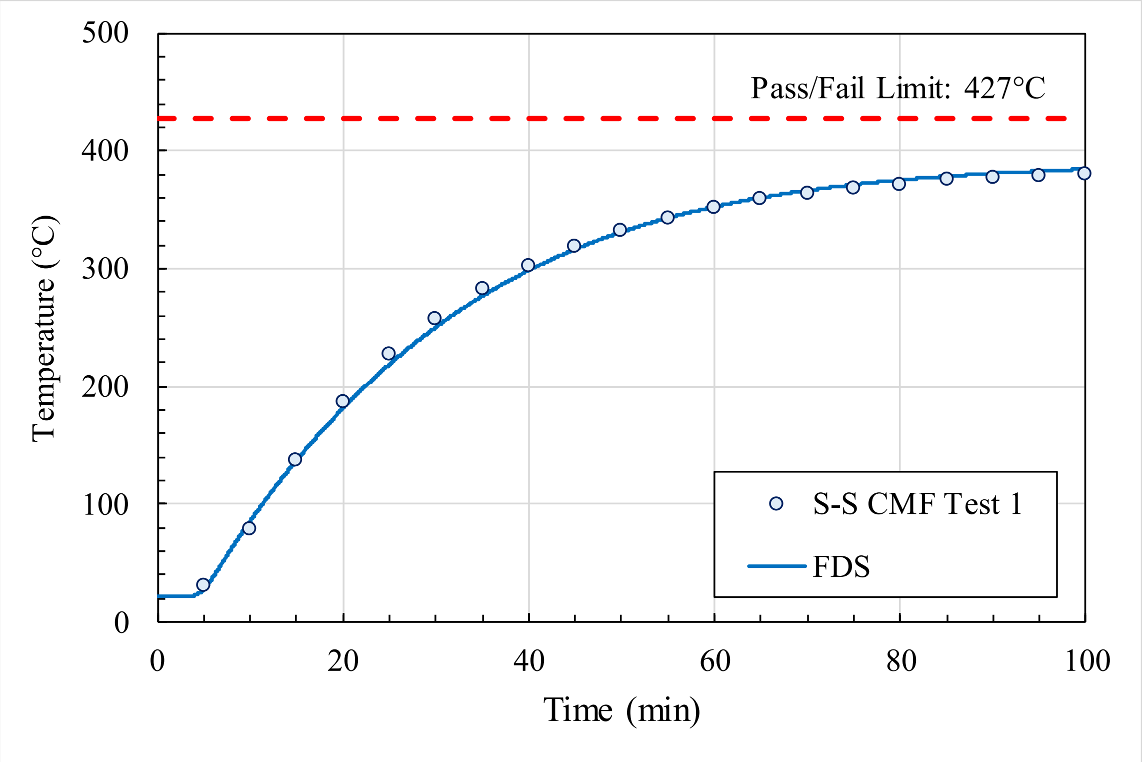

Figure 45. Calculated vs. Measured Backside Center Temperatures for the 1st Simulated Pool Fire Test (61).

Equation 7 expresses the boundary condition at the fire-exposed surface of the test specimen. When FDS is used with the gas phase turned off, only one fluid temperature can be specified. By default, this temperature is equal to the ambient temperature. Because the fluid temperatures on the exposed and unexposed sides are different (T_g and T_a, respectively), Equation 7 had to be modified as follows:

$$-k_{exp}\left.\frac{\partial T}{\partial x}\right|_{x=0} = \dot{q}''_{net,exp} = \varepsilon_{exp}\left(\dot{q}''_{inc,mod} - \sigma T^4_{s,exp}\right) + h_{c,exp}(T_a - T_s) \qquad (8)$$

with

$$\dot{q}''_{inc,mod} = \dot{q}''_{inc,exp} + h_{c,exp}\left(T_g - T_a\right)/\varepsilon_{exp} \qquad (9)$$

where

$\dot{q}''_{inc,mod}$ = modified incident radiant heat flux at the fire-exposed surface (kW/m2); and

T_a = ambient temperature (K).

The boundary condition at the unexposed (top) surface of the specimen can be expressed as follows:

$$\begin{aligned} -\mathrm{k}_{\mathrm{unexp}}\left.\frac{\partial \mathrm{T}}{\partial \mathrm{x}}\right|_{\mathrm{x=L}} &= \dot{\mathrm{q}}''_{\mathrm{net,unexp}} \\ &= \varepsilon_{\mathrm{unexp}}\sigma\left(\mathrm{T}^4_{\mathrm{s,unexp}} - \mathrm{T}^4_{\mathrm{a}}\right) + \mathrm{h}_{\mathrm{c,unexp}}\left(\mathrm{T}_{\mathrm{s,unexp}} - \mathrm{T}_{\mathrm{a}}\right) \end{aligned} \qquad 10$$

where

$\mathrm{k}_{\mathrm{unexp}}$ = thermal conductivity of the solid at the unexposed specimen side (W/m·K);

L = thickness of the test specimen (m);

$\dot{\mathrm{q}}''_{\mathrm{net,unexp}}$ = incident radiant heat flux at the unexposed specimen surface (kW/m2);

$\varepsilon_{\mathrm{unexp}}$ = surface emissivity/absorptivity of the unexposed surface (0.7 for steel);

$\mathrm{T}_{\mathrm{s,unexp}}$ = temperature at the unexposed surface of the specimen (K);

T_{a} = ambient temperature (K); and

$\mathrm{h}_{\mathrm{c,unexp}}$ = convection coefficient at the unexposed specimen surface (4 kW/m2·K).

The value for $\mathrm{h}_{\mathrm{c,unexp}}$ of 4 kW/m2·K was based on recommendations in Eurocode 1, Part 1-2 (79). The densities of the steel and SS-CMF plates were calculated from the measured weights and dimensions. The thermal properties of the steel (thermal conductivity and specific heat as a function of temperature, and the emissivity of 0.7) were taken from Eurocode 3, Part 1-2 (73). The emissivity and the thermal conductivity of the

SS-CMF(the latter as a function of temperature) were based on measurements reported in the literature (61, 40). Finally, the specific heat of the SS-CMF was assumed equal to that of stainless steel reported as a function of temperature in Eurocode 3, Part 1-2(73).

This section describes the results of a series of 3-D heat transfer calculations using the finite element software COMSOL Multiphysics®. The purpose of the COMSOL calculations is to determine up to what extent the discrepancy between the calculated and measured unexposed surface temperature distribution for the calibration test can be explained by the fact that FDS neglects lateral heat conduction due to heat losses at the perimeter of the exposed area of the specimen.

COMSOL Model Setup and Assumptions

Figure 46 shows an exploded view of the COMSOL geometries for the calibration test and simulated pool fire test, respectively. The orange plate at the bottom is a 0.61 × 0.61 × 0.00635 m section of the steel plate of the furnace lid. There is a 0.305 × 0.305 m opening at the center of the bottom plate to expose a steel plate (in a calibration test) or an SS-CMF specimen (in a simulated pool fire test) to the convective and radiative heat flux from the furnace. A 51 mm wide strip of two 25 mm layers of ceramic fiber blanket (Morgan Thermal Ceramics 96 kg/m3 Superwool®) is placed around the perimeter of the opening (green collars in Figure 46). To simulate a calibration test, a carbon steel plate measuring 0.406 × 0.406 × 0.016 m is placed on the ceramic fiber blanket (see Figure 46-a). For the simulated pool fire calculations, the 0.305 × 0.305 × 0.016 m plate is attached to the bottom of the steel plate and fits inside the ceramic fiber insulation (see Figure 46-b).

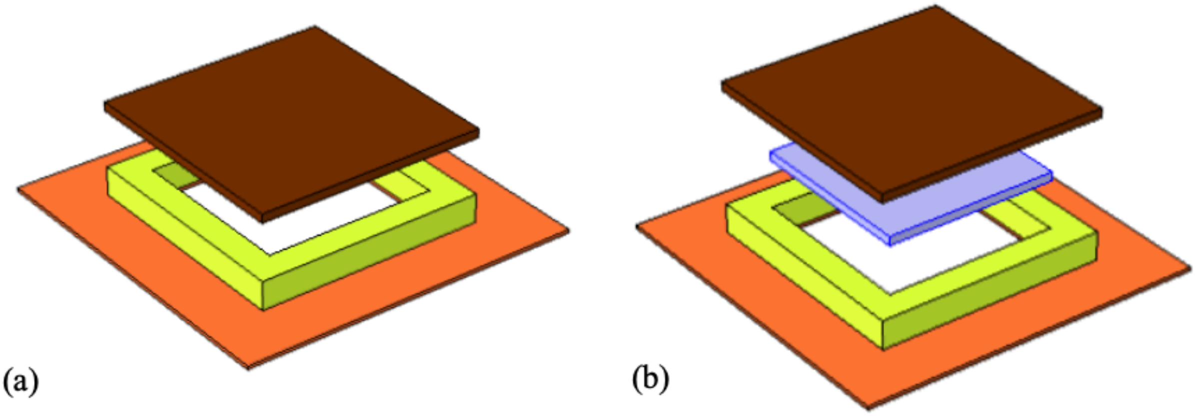

Figure 46. Exploded View of COMSOL Geometry for a) Calibration and b) Simulated Pool Fire Tests.

The thermal analysis was performed in the assumption that the incident heat flux is uniformly distributed over the entire fire-exposed surface of the specimen. In other words, Equation 7 with $\dot{q}''_{\mathrm{inc,exp}}$ = 71.7 kW/m2, $\mathrm{h_{c,exp}}$ = 10.5 W/m2·K, and $\mathrm{T_g}$ = 790°C was specified as the boundary condition for the central 0.305 × 0.305 m section of bottom surface of the steel plate (calibration test) or the entire bottom surface of the SS-CMF panel (simulated pool fire test). With this assumption, if lateral heat losses are indeed negligible, the temperature on the unexposed side of the test specimen should be the same over the entire surface.

The temperature-dependent thermal properties for the steel and SS-CMF used in the COMSOL calculations were obtained from Eurocode 3, Part 1-2 (73) and the literature (61,40), as discussed in the previous section. The thermal conductivity and specific heat of the ceramic fiber blanket as a function of temperature were based on data published by the manufacturer (80), while the emissivity was taken from a compilation of input data for fire modeling developed by Gross (81).

Results of a 3-D Thermal Analysis of the Third Calibration Test

The results of the COMSOL analysis of the third calibration test are shown in Figure 47 and Figure 48. Figure 47 is a contour temperature plot of the unexposed surface of the steel plate at 900 s. The exposed area is indicated by the dashed square, i.e., the bottom surface of the steel plate inside the dashed square is exposed to the furnace temperature, while the bottom surface area outside the dashed square is insulated with ceramic fiber blanket. Figure 48 is similar to Figure 44, except that it compares the unexposed surface temperatures measured at the nine thermocouple locations to those calculated in COMSOL

Results of 3-D Thermal Analysis of the First Simulated Pool Fire Test

The results of the COMSOL analysis of the first simulated pool fire test are shown in Figure 49-Figure 52. Figure 49 is a contour temperature plot of the unexposed surface of the steel plate at 6000 s. The exposed area is indicated by the dashed square, i.e., the entire bottom surface of the SS-CMF plate is inside the dashed square while the area of the bottom surface of the steel plate outside the dashed square is insulated with ceramic fiber blanket. Figure 50 through Figure 52 compare the unexposed surface temperatures measured at the thermocouple locations on the West side (TCs 1, 4 and 7), East side (TCs 3, 6 and 9) and in between (TCs 2, 5 and 8) to the corresponding temperatures calculated in COMSOL.

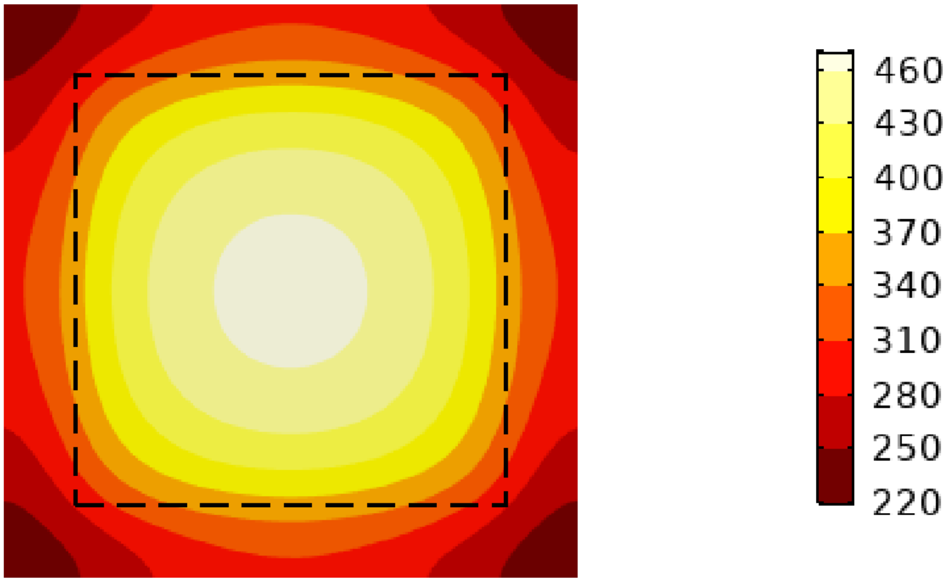

Figure 47. COMSOL Contour Temperature Plot of the Steel Plate Top Surface at 900 seconds .(Third Calibration Test)

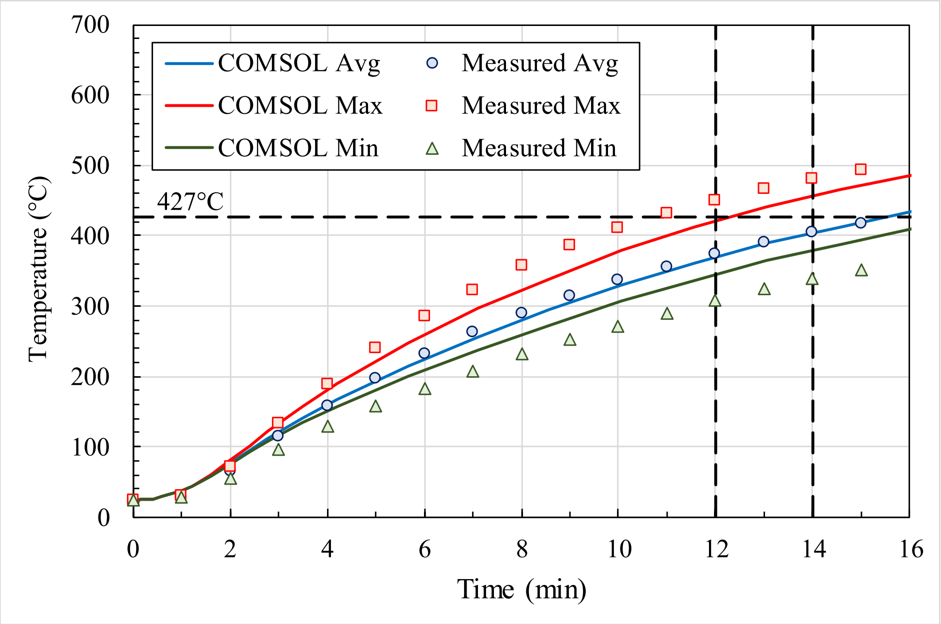

Figure 48. COMSOL vs. Measured Unexposed Surface Temperatures for the Third Calibration Test.

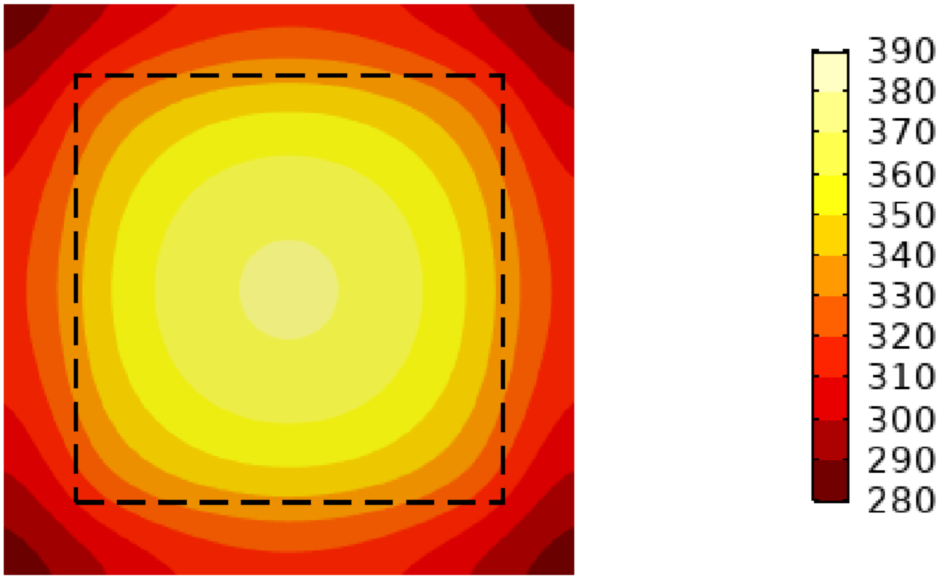

Figure 49. COMSOL Contour Temperature Plot of the Steel Plate Top Surface at 6000 s when a SS-CMF plate is placed under the steel plate. (First Simulated Pool Fire Test)

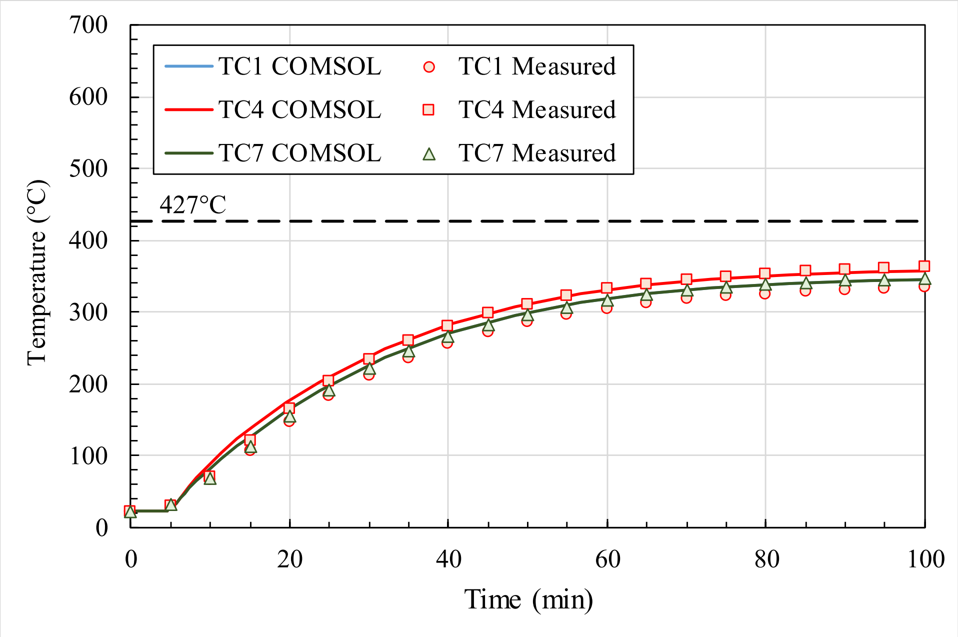

Figure 50. COMSOL vs. TC1, TC4, and TC7 Unexposed Surface Temperatures for the SS-CMF First Simulated Pool Fire Test.

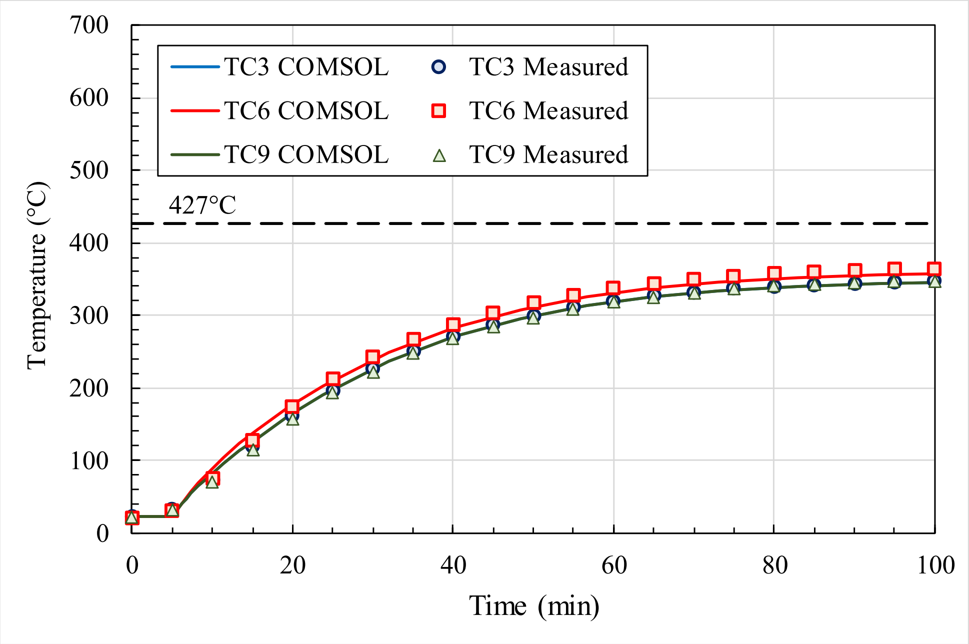

Figure 51. COMSOL vs. TC3, TC6, and TC9 Unexposed Surface Temperatures for the SS-CMF First Simulated Pool Fire Test.

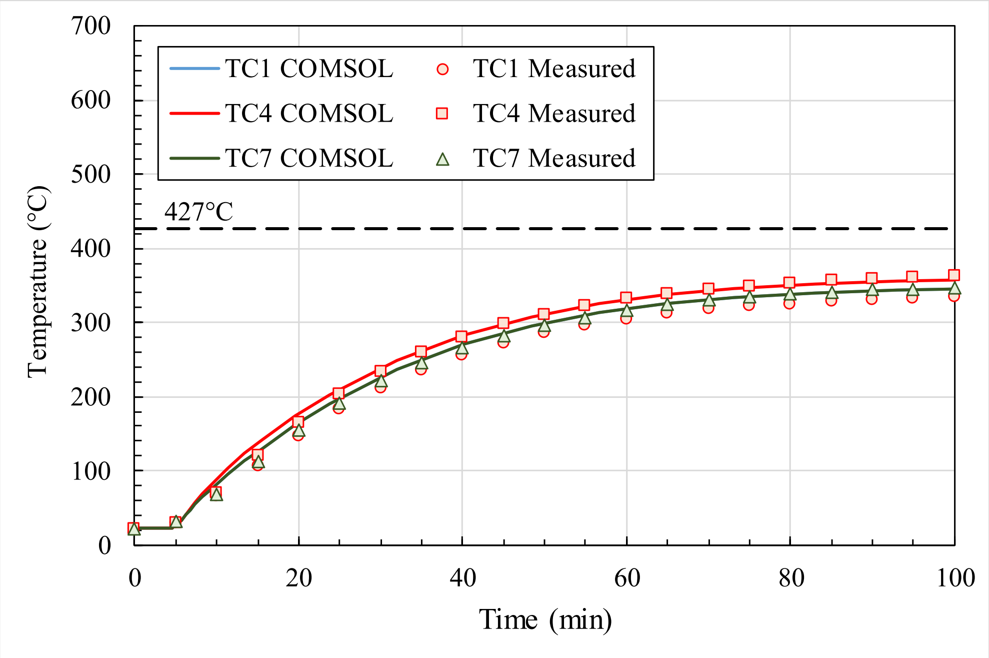

Figure 52. COMSOL vs. TC2, TC5, and TC8 Unexposed Surface Temperatures for the SS-CMF First Simulated Pool Fire Test.

Discussion

From a comparison between Figure 44 and Figure 48 it appears that accounting for lateral heat conduction and heat losses at the perimeter of the exposed area of the steel plate increases the non-uniformity of the predicted temperature distribution on the unexposed surface. However, the difference between the calculated highest and lowest unexposed surface temperatures is still significantly smaller than the difference for the measured temperatures. Figure 48 further shows that the calculated average unexposed surface temperature is very close to the measured average, which indicates that the uniform heat flux assumed in the COMSOL calculations seems to be representative of the average heat flux in the calibration test. Consequently, agreement between the calculated and measured unexposed surface temperature distributions can be improved by specifying a non-uniform heat flux distribution, i.e., by decreasing the specified heat flux on the West side (side where the burner was turned off) and by increasing the specified heat fluxes on the East side and especially in between.

Compared to Figure 47, Figure 49 shows that the effect of lateral heat conduction and heat losses at the perimeter of the exposed area of the steel plate on the uniformity of the unexposed surface temperature distribution is not nearly as pronounced in the simulated pool fire experiments as in the calibration tests, which can be due to the long exposure time (6000 s) compared to the calibration test time (900 s). Although Figure 50-Figure 52 show that agreement between the calculated and measured unexposed surface temperatures in the first simulated pool fire test is quite good, the heat flux adjustment suggested in the previous paragraph is likely to make the agreement even better. For example, Figure 50 shows that the unexposed surface temperatures on the West side are generally slightly higher than the corresponding measured temperatures. Consequently, specifying a lower heat flux, in particular in the corners, on the West side of the furnace is expected to improve the predictions.

8.6 Conclusions

Based on the experimental and modeling results, the 15.9 mm steel-steel composite metal foams tested as novel insulation system met the acceptance criteria for the simulated pool fire test in 49 CFR 179 Appendix B by a large margin and is expected to pass with near certainty if the test were to be reproduced in a different laboratory. Furthermore, the successful performance of SS-CMF in the simulated pool fire test (described in 49 CFR Part 179) can be attributed to its exceptional thermal conductivity due to the presence of air bubbles inside along with its low surface emissivity. To complete the full test requirements of CFR Part 179 App. B, the material will need to be tested to the torch-fire exposure in duplicate. Moreover, a more detailed simulation modeling effort would be needed in which the complexity of the structure of SS-CMF with multiple components of air, metal and their interfaces are considered as well as the detailed measurements of thermal properties of the material at high temperatures close to those of torch fire testing temperatures to be included in the model to have a more accurate prediction of its performance in torch fire conditions.

9 Jet Fire Testing of Composite Metal Foam (A Scale Down Version of Torch Fire Test)

9.1 Abstract

A full-scale simulated torch fire testing requires panels of 122 x 122 cm dimensions and is designed to measure the thermal effectiveness of new or untried thermal protection systems. However, due to the limitations in manufacturing composite metal foam panels in larger scale, at first an extrapolation of the simulation model from the pool fire testing was done to predict the thickness required for torch fire testing. The study was done at Southwest Research Institute. Upon completion of the extrapolated model, the resulted thickness was too far from reality mainly because many of the boundary conditions and base parameters to establish the model were based on the properties of the SS-CMF tested at much lower temperature ranges. For example, the thermal conductivity values of SS-CMF were based on the experimental values at 300–600 °C taken from our prior studies (40) and the values at the remaining temperatures were obtained from an extrapolation. Such extrapolations worked to some extent in the modeling of pool fire testing since pool fire test is conducted at 800ºC range. As such, with some manipulations of the surface emissivity, the results of modeling and experiments were matching as described in the prior section of this report. But, the torch fire test is to be conducted at 1200ºC, this seemed to be too much of an extrapolation. As such a scaled down version of the torch fire test was developed to provide initial data on the thermal protection performance of SS-CMF in torch fire set up using smaller panels.

In this study, A scaled down version of the full-scale torch fire experiment specified in 49 CFR Part 179, Appendix B was developed to provide initial data on thermal protection performance of SS-CMF panels of 30.2 x 30.2 cm dimensions. The set-up was designed to expose panels to a 30-minute torch fire condition of high velocity jet fire with a gas temperature of 1204ºC in accordance with 49 CFR Part 179. Prior to the actual test, jet burner gas temperature and velocity flow field was characterized, and a calibration fire test was conducted using a steel plate as required by the test specification. The assembly was tested in duplicate in two consecutive simulated jet-fire exposures as specified in 49 CFR Part 179, Appendix B and achieved successful results. Based on the experimental results, a 15.2 mm thick steel-steel composite metal foam met the acceptance criteria for the simulated torch fire testing by a large margin and is expected to pass when tested in a full-scale torch fire set up of 122 x 122 cm dimensions. The main factor for fire resistance and thermal protection performance of SS-CMF is attributed to the large air content in the material. This research confirms that one of the potential applications of lightweight SS-CMF can be in the structure of tank-cars carrying hazardous materials and replacing conventional structural steel with demonstrated benefits of excellent thermal insulation, fire resistance, low weight along with its established energy absorption capabilities discussed in prior sections of this report.

9.2 Experimental Procedure:

Materials and Processing:

Two of the three panels of 30.2 x 30.2 x 1.59 cm Steel-steel Composite Metal Foam (S-S CMF) that were manufactured and then used in a simulated pool fire testing set up that is reported in prior section of this report were cleaned up after the pool fire testing to remove any oxide layers and discoloration from the surface of the sample resulted from the 100 minutes exposure of the simulated pool fire testing. The cleanup of samples included a surface grinding using a 35 x 150 cm Gallmeyer & Livingston Co. “Grand Rapids” grinding machine. Since the 15.9 mm SS-CMF panels has met the acceptance criteria for the simulated pool fire test in 49 CFR 179 Appendix B by a large margin, the panels were ground down to two thicknesses of 13.6 mm (equivalent to about 6 layers of hollow spheres in the structure of SS-CMF panel) and 15.2 mm (equivalent to 7 layers of hollow spheres in SS-CMF panel) in order to pinpoint the exact thickness required to meet the acceptance criteria for the simulated torch fire testing without too much of a margin. The dimensions of tested panels after grinding and before the small scale torch fire/ jet fire testing is shown in Table 21.

Table 21. Tested SS-CMF specifications.

Test No.	Sample ID	Thickness, (cm)	Measured Width × Length (cm)	Weight, kg
1	C3	1.52	30.2 x 30.2	3.545
2	C2	1.36	30.2 x 30.2	3.022
Calibration Plate	Steel A36	1.59	40.6 × 40.6	20.443*

* Estimated based on the dimensions and the density.

Small-Scale Torch Fire Test Setup

The testing in this study was performed in general accordance with the simulated torch fire test specified in 49 CFR Part 179, Appendix B (82). The specification requires a sample to be subjected to a high velocity jet fire with a gas temperature of 1204 ± 55.6ºC (2200 ± 100ºF) and velocity of 17.9 ± 4.5 m/s (40 ± 10 mph) at the sample location. The setup (shown in *Figure 53*) is composed of a 7.6 cm (3.0 in.) diameter jet burner that is located at 8.89 cm below a 30.2 m x 30.2 cm sample that rests beneath an instrumented 40.6 m x 40.6 cm Steel A36 plate. The sample and steel plate are supported by a steel Unistrut frame with Durock cement board to redirect hot gases away from the back of the sample and steel plate. The edges of the sample rest on top of a 2.54 cm (1.0 in.) thick Thermal Ceramics Superwool 607 high temperature ceramic fiber board to thermally isolate the sample from the steel Unistrut frame. The edges of the steel plate and sample are also insulated with the 2.54 cm (1.0 in.) thick ceramic board. With this setup, heating of the instrumented steel plate only occurs through the heat transmitted through the sample due to the impinging jet flame. The propane gas flow rate into the jet burner was regulated using an Alicat MC-100 mass flow controller with a range of 120 SLPM (0.002 m3/s) and accuracy of ±0.2% full-scale.

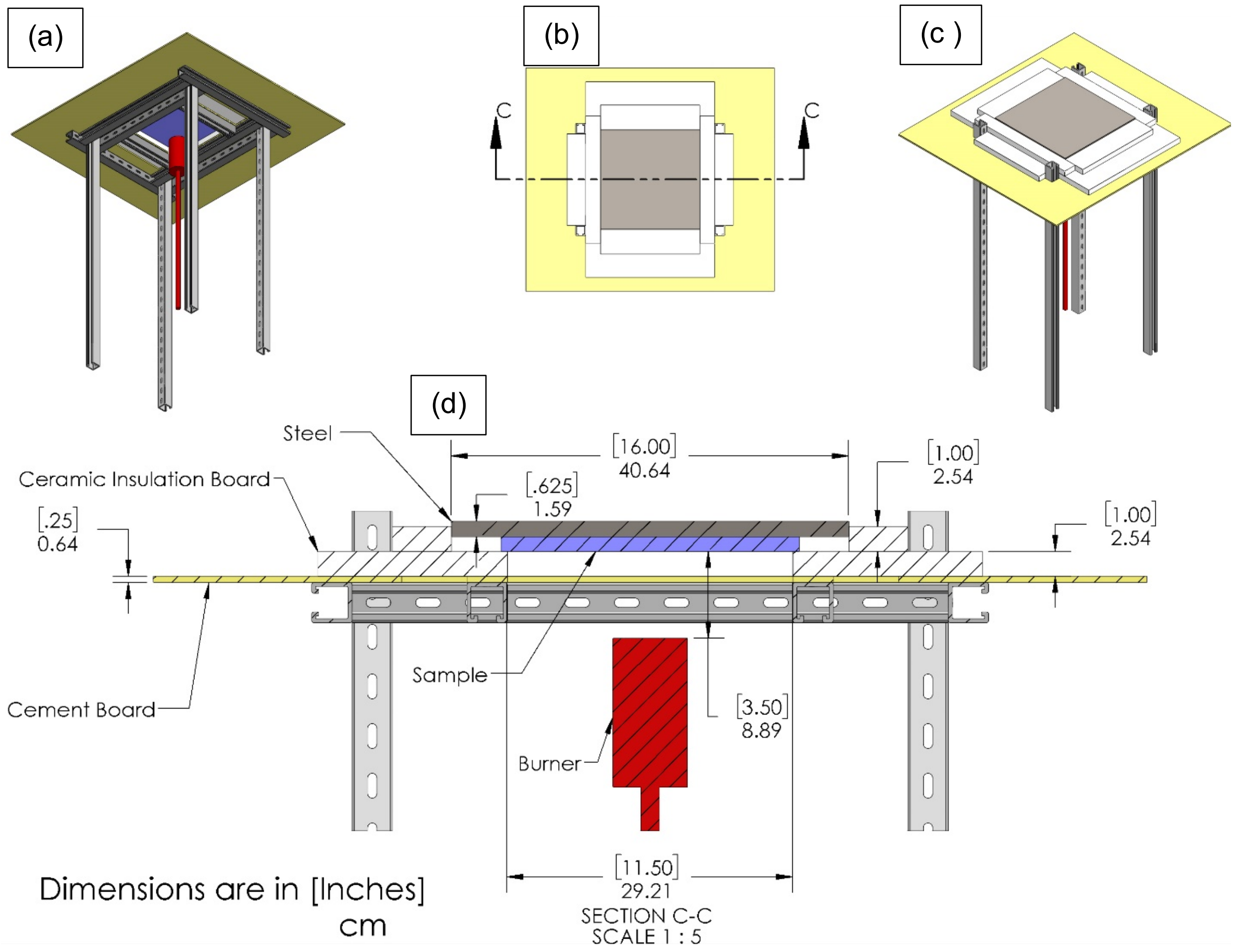

Figure 53. Reduced-scale torch fire test setup; (a) Bottom 3-D view, (b) Top view, (c) top/side 3-D view and (d) Detailed cross-sectional side view through section C-C shown in figure (b).

The unexposed surface of the steel plate was instrumented with a series of thirteen 24 gauge, Type K thermocouples welded onto the surface of the plate. The locations of the thermocouples are provided in Figure 54. Locations of Thermocouples 1 – 9 were based on dividing the steel plate into nine equal quadrants and placing thermocouples in the center of each quadrant. Thermocouples 10 – 13 were located based on dividing the sample into nine equal quadrants and having a thermocouple in four of the quadrants closest to the burner. During the test, steel temperature data was collected using a

National Instruments (NI) cDaQ-9174 with a NI 9213 16 bit card at a sampling frequency of 1 Hz.

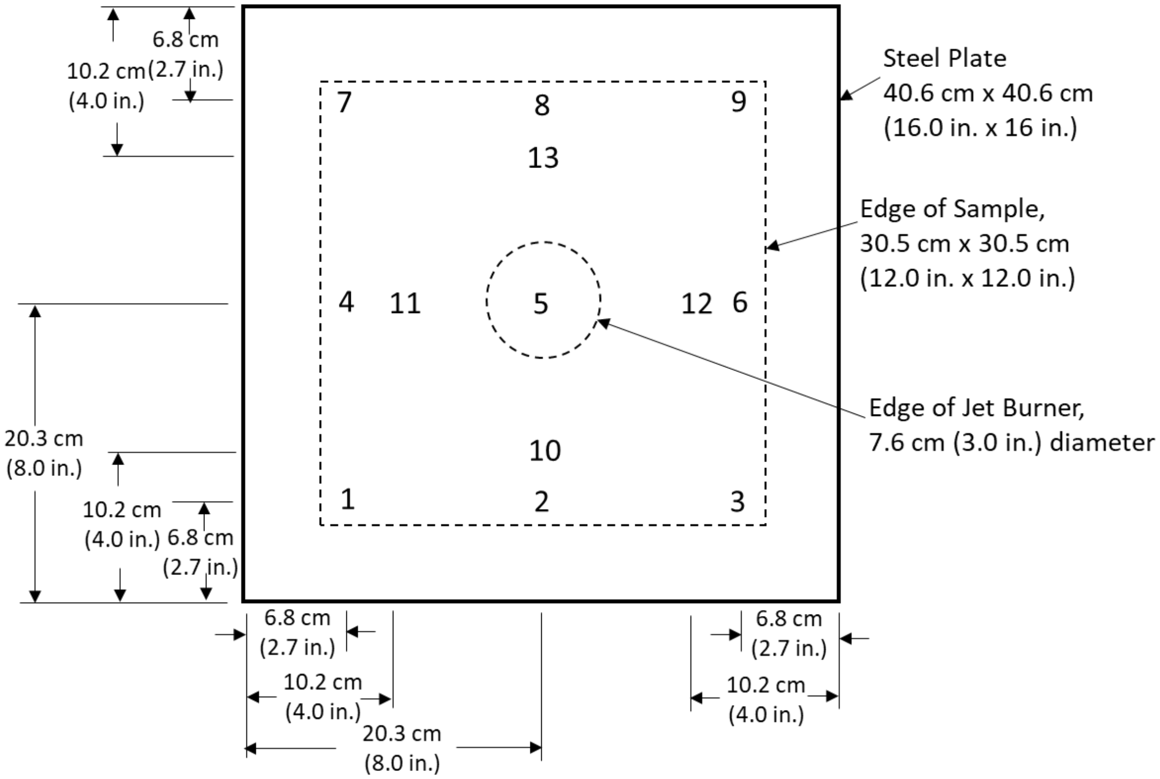

Figure 54. Thermocouple locations on the unexposed surface of the steel plate

The jet burner was characterized before being placed beneath the test setup to ensure that the required gas temperature and velocity would be achieved at the sample surface. For this, instrumentation was place 8.89 cm (3.5 in.) above the jet burner exit to measure temperature and velocity at the sample location, see Figure 55. Temperature was measured using a Type K, 0.15 cm (0.0625 in.) diameter Inconel sheathed thermocouple. Velocity was measured using a 1.9 cm (0.75 in.) stainless steel bi-directional flow probe designed for high temperature fire applications to reduce clogging of pressure port holes with soot (83).

Data for the jet fire characterization was collected using a NI cDaQ-9174 with a NI 9213 16 bit card for the gas temperature measurement and a NI 9205 16 bit voltage card to measure the pressure difference across the bi-flow probe. The pressure was measured using a Setra Model 264 differential pressure transducer with a 248.8 Pa (1.0 in. WC) range and an accuracy of 0.22% full-scale. Using the pressure difference, the velocity was calculated by

$$\mathrm{V} = \frac{(2\Delta \mathrm{p}/\rho)^{1/2}}{\mathrm{k}} \tag{1}$$

where V is the velocity (in m/s), Δp is the measured pressure difference across the bi-flow probe (in Pa), ρ is the gas density determined from the gas temperature using the ideal gas law (ρ=353.4/T), T is the gas temperature (in K) and k is a dimensionless calibration constant for the probe which was 1.22 for these flow conditions. Sampling was performed at a sampling frequency of 1 Hz. The gas burner was operated with 23 SLPM (3.833x10-4 m3/s) propane which corresponds to an ideal heat release rate of 33 kW fire. The results of the jet fire characterization testing are provided in Figure *56*. During the steady state period (40 – 100 seconds), the gas temperature was 1229±18ºC (2244±33ºF) while the velocity was 39.2±7.9 mph (17.5±3.5m/s), both of which are within the required range specified in 49 CFR 179, Appendix B.

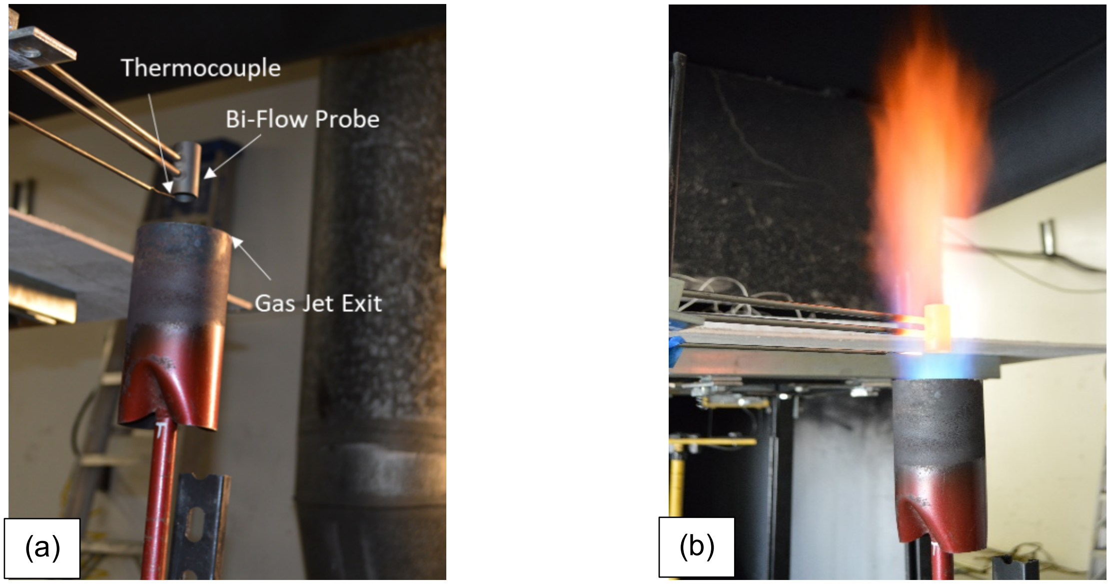

Figure 55. Instrumentation used to characterize the jet burner flow field conditions at the sample location.

Heat Flux Mapping

A series of tests were conducted to measure the heat flux from the jet fire exposure to the sample location. In these tests, a noncombustible board (Durock) was placed at the sample location with a heat flux gage mounted in the board. The gage measurement surface was flush with the exposed surface of the board. The heat flux gage was a 25.4 mm (1.0 in.) diameter, Medtherm 64-20SB-19 water-cooled Schmidt-Boelter gage, 0-200 kW/m^2 range with a 3% uncertainty and surface emissivity of 0.94. During the mapping, the gage was located at the center of the sample exposure area and then moved in 12.7 mm (0.5 in.) to 25.4 mm (1.0 in.) increments away from the center. As shown in Figure 57, measurements were made at a total of eight locations.

With the gage located in the center of the sample area (x=0), the data acquisition was started and the jet burner was ignited to the test propane flow rate of 23 SLPM (3.833x10-4 m3/s) at 15 seconds. The jet burner was allowed to reach a steady-state operating condition before the heat flux measurement sequence was started, which was approximately 60 seconds after the data acquisition was started. The gage was left at each measurement location for 20 seconds before being moved to the next location. A plot of the heat flux measured during the testing is provided in Figure 58. The average heat fluxes are included in Table 22 along with the averaging times at each location. The heat flux is relatively constant at approximately 160 kW/m^2 over twice the jet burner radius, 38.1 mm (1.5 in.), and then decreases with distance beyond this location. Near the edge of the sample location the heat flux is approximately 100 kW/m^2.

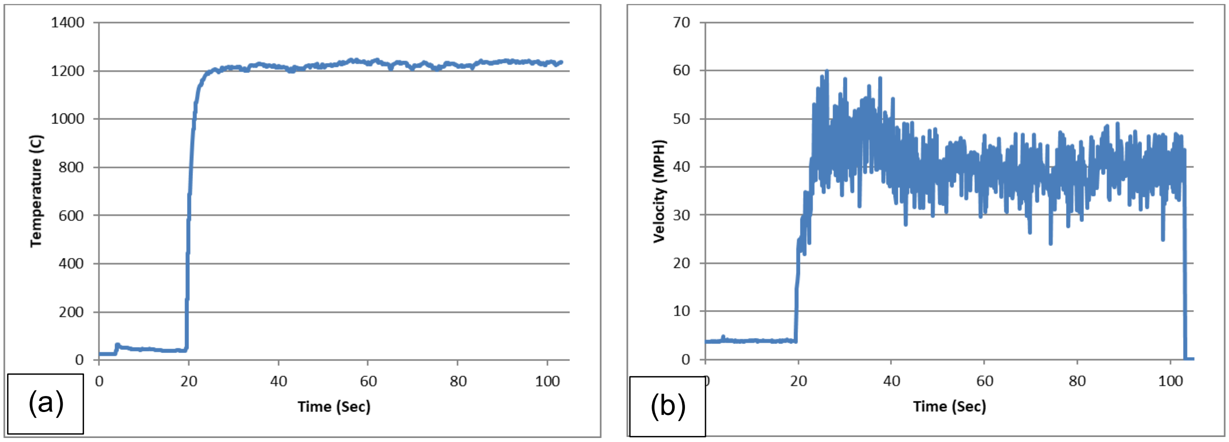

Figure 56. Results of the jet fire characterization testing showing a) jet fire temperature and b) jet fire velocity.

Table 22. Average heat flux at different locations over the sample shown in Figure 57.

Location	Distance, x, mm(in.)	Averaging Time (s)	Average Heat Flux (kW/m2)
1	0.0 (0.0)	65 - 85	166
2	12.7 (0.5)	86-105	165
3	25.4 (1.0)	106-125	162
4	38.1 (1.5)	126-145	164
5	50.8 (2.0)	146-165	160
6	76.2 (3.0)	166-185	148
7	101.6 (4.0)	186-205	135
8	127.0 (5.0)	206-225	106

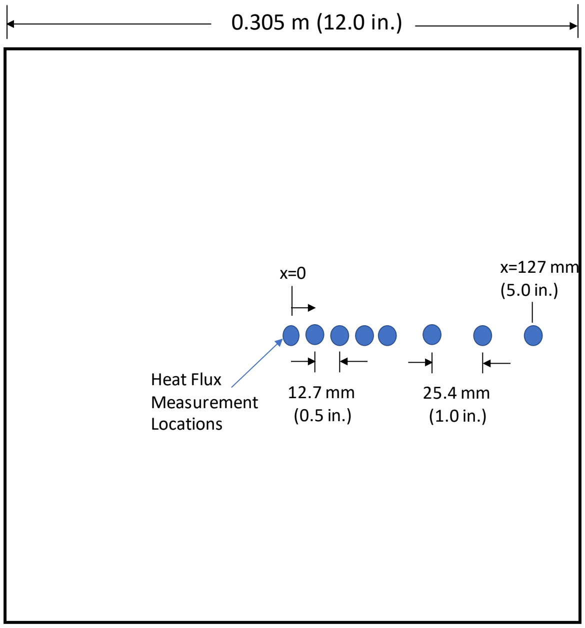

Figure 57. Heat flux measurement locations in sample exposure area.

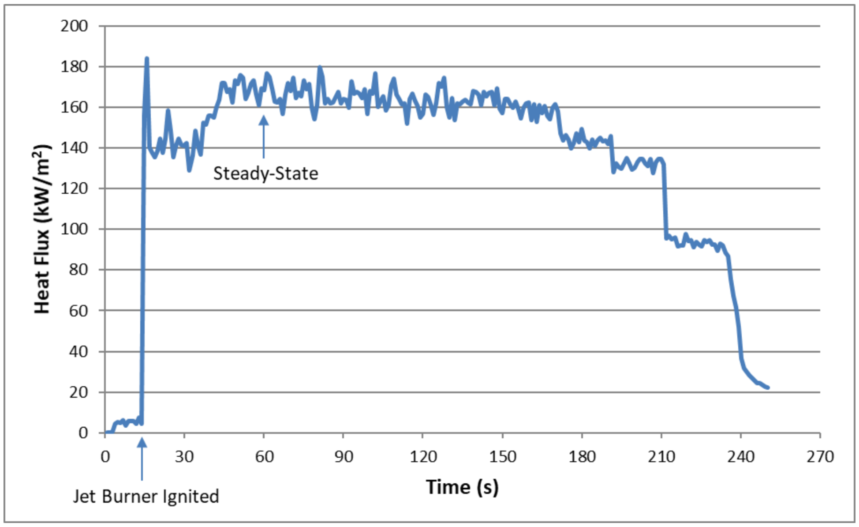

Figure 58. Heat flux with time during the jet exposure.

Calibration Test

A test was performed with the instrumented steel plate only (no SS-CMF sample) to demonstrate the setup meets the torch fire exposure requirements in 49 CFR 179, Appendix B. In this calibration test, the steel plate was placed on top of the ceramic board at the sample location, 8.89 cm (3.5 in.) above the jet burner exit. The plate was exposed to the burner conditions for 30 minutes. The test specification requires that two of the thermocouples on the unexposed side of the steel plate reach 427ºC (800ºF) within 4.0±0.5 min. Since this is a reduced scale test on smaller panels, the requirement for the temperature rise was taken for only the center thermocouple to reach the specified temperature rise in the allotted time.

The temperature rise of the plate is provided in Figure 59 for thermocouples at the center of the plate (Thermocouple 5) and the four locations closest to the jet. The highest temperature is related to the thermocouple at the center of the plate where the jet burner impinges on the plate. As can be seen in this figure, the temperature reaches 427ºC (800ºF) at 4.42 min., which is within the time specified in the test requirements specified in 49 CFR 179, Appendix B (4 min. ± 0.5 min.). After a 30 min. exposure, the center temperature is 725ºC (1337ºF) while the other thermocouples were ranging from 600 to 639ºC (1112-1182ºF).

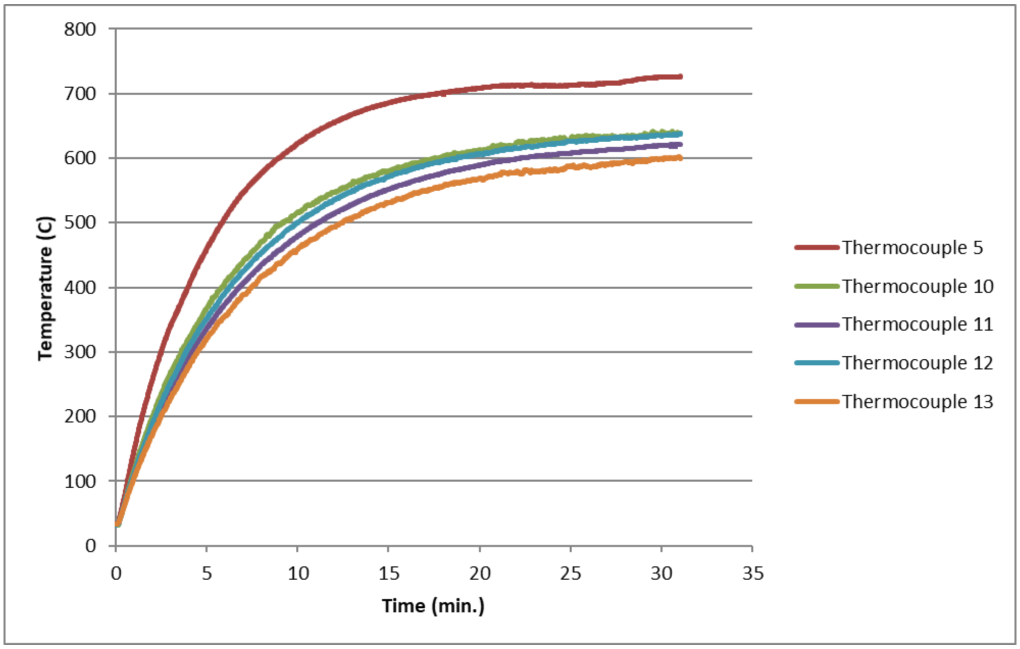

Figure 59. Temperature rise of steel plate during calibration test (no sample).

9.3 Torch Fire Tests

Torch fire tests were performed on two 30.2 cm x 30.2 cm SS-CMF panels. Each torch fire test was conducted with the panel at an initial temperature between 0–37.8 ºC

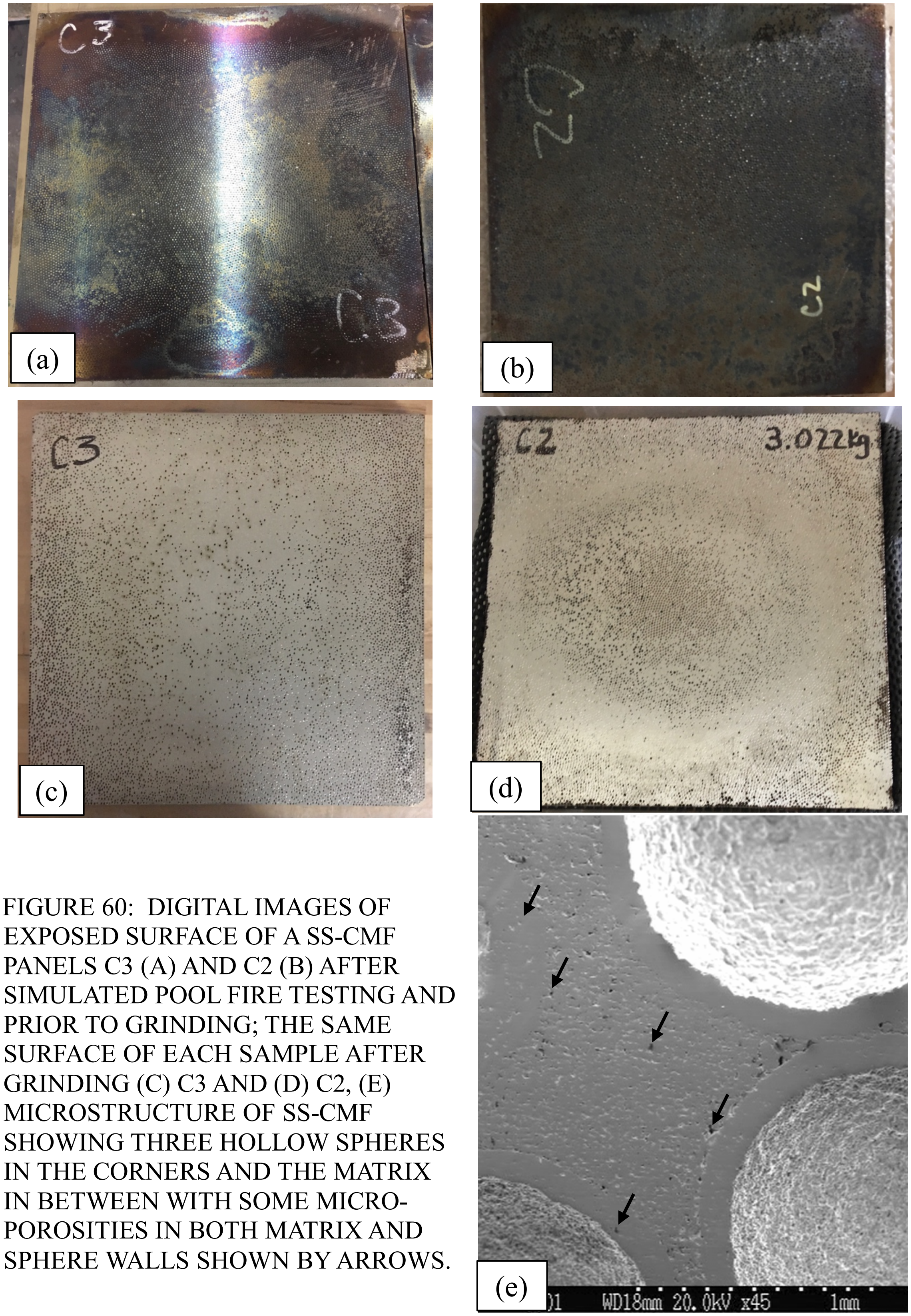

FIGURE 60: DIGITAL IMAGES OF EXPOSED SURFACE OF A SS-CMF PANELS C3 (A) AND C2 (B) AFTER SIMULATED POOL FIRE TESTING AND PRIOR TO GRINDING; THE SAME SURFACE OF EACH SAMPLE AFTER GRINDING (C) C3 AND (D) C2, (E) MICROSTRUCTURE OF SS-CMF SHOWING THREE HOLLOW SPHERES IN THE CORNERS AND THE MATRIX IN BETWEEN WITH SOME MICRO-POROSITIES IN BOTH MATRIX AND SPHERE WALLS SHOWN BY ARROWS.

(32 – 100ºF) as required by the test specification in 49 CFR 179, Appendix B. Prior to each test, the accurate operation of each thermocouple was verified by heating it briefly with a torch. Each test was video recorded with a view of the exposed sample surface to document any changes in the sample during the test. A 30 second baseline of data was taken prior to igniting the jet burner. The burner gas flow rate was maintained at 23 SLPM of propane for 30 min. At 30 min., the gas flow was shut down and the data acquisition was turned off.

FIGURE 60 shows the surface of the samples before and after grinding as well as its microstructure. As can be seen the structure of the SS-CMF panel is made up of large macro-porosities of spheres along with fine micro-porosities within the matrix and sphere walls.

Test 1

This test was conducted using a 1.52 cm (0.60 in.) thick sample with a weight of 3.545 kg and about 7 layers of hollow spheres within the thickness of the panel. The initial temperature for the test was 16ºC. The temperature for the center thermocouple (Thermocouple 5) and the four closest thermocouples to the center are provided in Figure 61. As can be seen in the figure, upon reaching the 30 minute time of exposure, the maximum temperature on the unexposed surface of the panel was 400ºC (752ºF) at the center of the plate directly above the jet burner. This temperature is well below the required temperature limit of 427ºC; therefore, this sample met the torch fire test requirements specified in 49 CFR 179, Appendix B.

Images of the sample before, during and after the testing are included in Figure 62. As seen in the images, the sample surface before testing was clean stainless steel with open cavities. During testing, the surface did not show any deformation, crack or degradation. Following the test, the sample was discolored but was not physically damaged or deformed.

Test 2

The second test was performed using a thinner, lighter sample with a 1.36 cm (0.54 in.) thickness and 3.022 kg weight including about 6 layers of hollow spheres within the thickness of panel. The initial temperature for the test was 30ºC (about 14ºC higher than the first test).

The temperature for the center thermocouple (Thermocouple 5) and the four closest thermocouples to the center are provided in Figure 63 . As can be seen in the figure, upon reaching the 30 minutes time of exposure, the maximum temperature on the unexposed surface of the composite metal foam panel was 435ºC (815ºF) at the center of the plate directly above the jet burner. This temperature is 8ºC higher than the required temperature rise limit of 427ºC; therefore, this sample did not meet the torch fire test

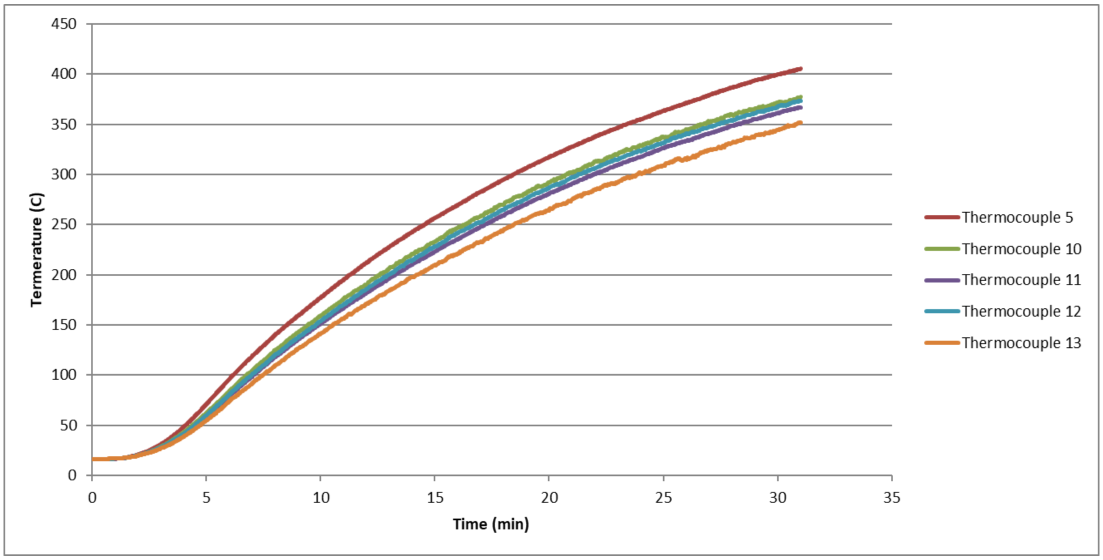

Figure 61. Test 1 measured temperature rise behind the 15.2 mm thick SS-CMF panel.

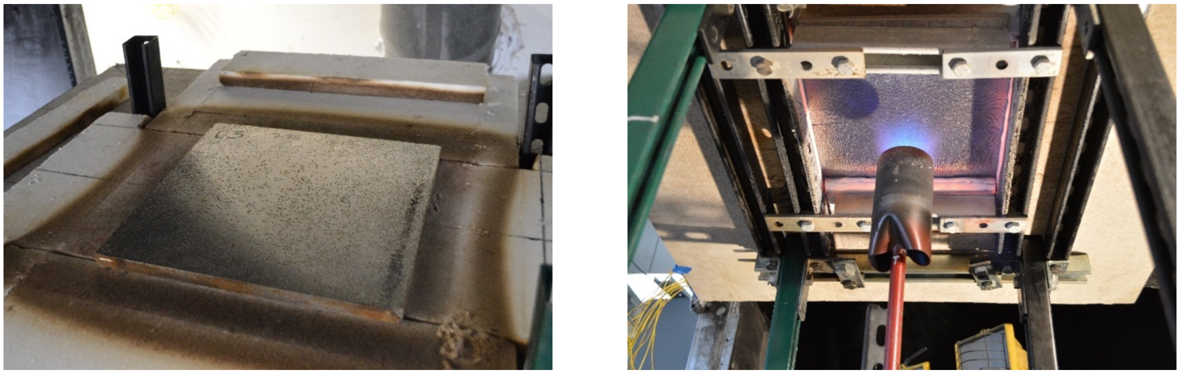

Before Test First 10 min. of Test

Last 10 min. of Test After test

Figure 62. Test 1 sample (Panel C3) images before, during and after testing.

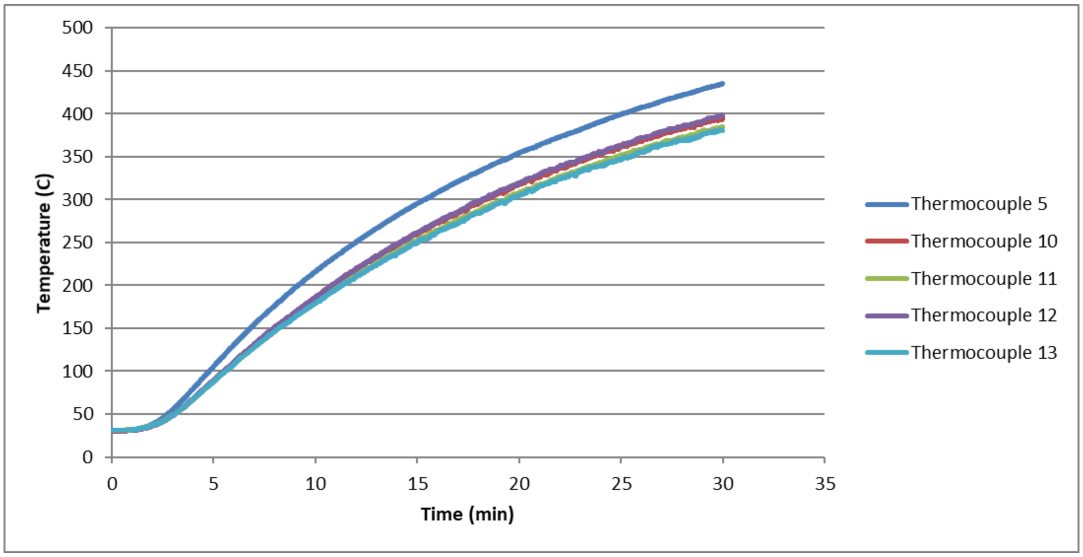

Figure 63. Test 2 measured temperature rise behind the 13.6 mm thick SS-CMF panel.

Before Test

First 10 min. of Test

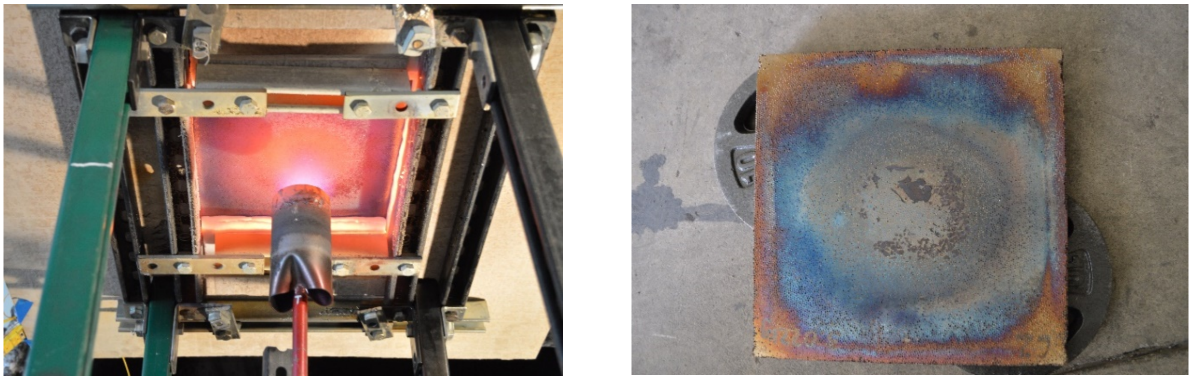

Last 10 min. of Test

After Test

Figure 64. Test 2 SS-CMF sample (C2 Panel) images before, during and after testing.

requirements. However, it is notable that the initial temperature of the plate in Test 2 was 14ºC higher than Test 1 and as such its temperature rise above the initial temperature (T_{final}-$T_{initial}$) was only 405ºC. If the initial temperature in Test 2 was less than 22ºC, it is possible that the sample in Test 2 would have met the 427ºC temperature requirement.

Images of the sample before, during and after the testing are included in Figure 64. As seen in the images, the sample surface before testing was clean stainless steel with open cavities. similar to the sample in Test 1, the sample did not experience any deformation, cracking or be degradation due to the exposure. Following the test, the sample was discolored but was not physically damaged or deformed.

Discussions

The exceptional thermal properties and fire protection of SS-CMF is related to the surface properties, the unique microstructure that includes large macro-porosities of hollow metal spheres, and the fine micro-porosities within the matrix and sphere walls resulting from their processing through powder metallurgy technique. The impact of some of these parameters on the material heat transfer performance were already discussed in the pool fire study section.

The SS-CMF has been measured to have a thermal conductivity 5-10 times less than that for solid stainless steel and the carbon steel (40). This is due to the 60-70% air content within the structure of S-S CMF, which makes it an effective insulator and slow down the through thickness heating of the material. The presence of air within SS-CMF porosities acts as insulator, which is similar to other insulating foams such as Styrofoam, insulating foam boards and spray foams. However, SS-CMF is made of steel and can withstand heat and fire up to over 1200ºC without any damage as demonstrated in this study.

The results of the current two tests along with the prior simulated pool fire testing indicate the potential of light-weight SS-CMF panels to be used in the structure of next generation tank-cars with more protection against fire. To complete the full-scale test requirements of CFR Part 179 App. B, panels of 122 x 122 cm dimensions will need to be tested against the torch-fire exposure in duplicate.

9.4 Conclusion

A reduced-scale torch fire test was developed in general accordance with 49 CFR 179, Appendix B to screen the thermal protection performance of small, 30.2 cm x 30.2 cm SS-CMF panels. The jet fire used in the test setup was demonstrated to meet the gas temperature and velocity requirements stated in the test specification. In addition, a calibration test was performed with the instrumented steel plate only (no sample), and the exposure was sufficient to result in the required temperature rise of the steel plate.

Two tests were successfully performed on the SS-CMF panels of two different thicknesses. It was determined that a 1.52 cm (0.60 in) thick panel with 7 layers of hollow spheres within its thickness provides adequate thermal protection to meet the torch fire test requirements in 49 CFR 179, Appendix B in a small scale arrangement. However, reducing the thickness to 1.36 cm (0.54 in.) or 6 layers of hollow spheres within the thickness of the panel resulted in slightly more heat transmission through the panel causing the panel to not meet the temperature rise requirement by only 8 degrees. It is notable that in Test 2, the temperature rise during the test indicates that if the initial temperature was less than 22ºC (similar to the initial temperature of Test 1), the sample might have met the temperature requirement. As a result, the required thickness of SS-CMF panel for full-scale torch fire testing to address all requirements of 49 CFR 179, Appendix B must be in the range of 14-15 mm. This research indicates that one of the potential applications of lightweight SS-CMF can be in tank-cars carrying hazardous materials and in combination with the conventional structural steel with demonstrated benefits of excellent thermal insulation, fire resistance, low weight along with its established energy absorption capabilities. To complete the full-scale test requirements of CFR Part 179 App. B, panels of 122 x 122 cm dimensions will need to be tested against the torch-fire exposure in duplicate.

10 Publication List

The results of this study have been published or is pending publication in a number of journal and proceeding papers as follows:

1. J. Marx, and A. Rabiei, "Study on microstructure and compressive properties of composite metal foam sandwich panels", Journal of Sandwich Structures & Materials, in review
2. J. Marx, and A. Rabiei, "Tensile properties of Composite Metal Foam and composite metal foam sandwich panels" Material Characterization, Metallurgical and Materials Transaction, in review
3. A. Rabiei, M. Portanova, J. Marx, C. Scott, and J. Schwant, "A study on performance of composite metal foam core sandwich panels under high speed puncture test" International Journal of Impact Engineering, in review
4. A. Rabiei, K. Karimpour, D. Basu and M. Janssens, "Steel-Steel Composite Metal Foam in Simulated Pool Fire Testing" International Journal of Thermal Sciences, 153 (2020) 106336
5. Jacob Marx, Afsaneh Rabiei, "Study on the Mechanical Properties of Composite Metal Foam Core Sandwich Panels" Proceedings of the 11th International Conference on Porous Metals and Metallic Foams (MetFoam 2019), PP 83-91.
6. Afsaneh Rabiei, Kamellia Karimpour, Marc Janssens and Debashis Basu **"**Simulated Pool Fire Testing And Modeling Of A Composite Metal Foam"**,** 15 International conference and exhibition on fire science and engineering, Interflam 2019, PP 985-996.

11 Future Work

- To complete the full test requirements of CFR Part 179 App. B, in measuring the thermal effects of new or untried thermal protection systems, such as SS-CMF, a full scale torch-fire exposure testing in duplicate is necessary. This set of testing is more expensive. However, the small scale jet fire testing provided a starting proof of concept with some encouraging results. A complete set of full-scale torch fire testing according to the CFR Part 179 App. B, requirements would complete the loop for approval of the material for application in tank-cars.
- A full-scale puncture testing of SS-CMF and SS-CMF core sandwich panels would also help validate and confirm the benefits of SS-CMF in the structure of next generation of more efficient tank-car structures.
- Also, more detailed studies on welding and assembly of composite metal foams would be needed.

12 Acknowledgements

This study was possible through the Department of Transportation (DOT) Pipeline and Hazardous Materials Safety Administration (PHMSA) funding, project number DTPH5616C00001. We would like to acknowledge the efforts from the following team of collaborators and students who contributed to this research:

- Professor Brian Y. Lattimer, Mechanical Engineering (ME), Virginia Tech (VT),
- Dr. Marc Portanova, U.S. Army Research, Development & Engineering Center, Fort Eustis,
- Dr. Marc Janssens, Southwest Research Institute,
- Dr. Debashis Basu, Southwest Research Institute,
- Jeremy McDonald, Southwest Research Institute,
- Ms. Alexandra Joyce, Southwest Research Institute,
- Jacob Marx, PhD Candidate, MAE, NCSU
- Christopher Scott, MS student, MAE, NCSU
- Jerod Schwandt, UG student, MAE, NCSU
- Kamellia Karimpour, Highschool volunteer, MAE, NCSU
- Ms. Michelle Gasbarro, MDG solutions Inc.

13 References

---

1. Association of American Railroads, "Freight Rail Hazmat & Tank-car Regulations," https://www.aar.org/article/freight-rail-hazmat-regulations.

2. J. Murphy, "Lac-Mégantic: The runaway train that destroyed a town", BBC News, Toronto, January 19, 2018, https://www.bbc.com/news/world-us-canada-42548824.

3. Jane Lindholm and Ric Cengeri, "2 Years After Lac-Mégantic Disaster, A Focus On Settlement Funds And Rebuilding" JUL 15, 2015**,** http://digital.vpr.net/post/2-years-after-lac-m-gantic-disaster-focus-settlement-funds-and-rebuilding#stream/0

4. D. Thomas, "DOT-117 tank-car rule debuts with controversy," *Railway Age,* May 1, 2015, https://www.railwayage.com/regulatory/dot-117-tank-car-rule-debuts-with-some-controversy/.

5 . https://www.law.cornell.edu/cfr/text/49/179.202-13, Cornel Law School, Legal Information Institute, Open Access to Law since 1992

6. https://www.law.cornell.edu/cfr/text/49/179.18, Cornel Law School, Legal Information Institute, Open Access to Law since 1992

7. Adams, G., Mintz, T., Necsoiu, M., & Mancillas, J. (2010). Analysis of Severe Railway Accidents Involving Long Duration Fires. United States Nuclear Regulatory Commission.

8. Tyrell, David & Jeong, David & Jacobsen, Karina & Martinez, Eloy. (2007). Improved Tank-car Safety Research. 10.1115/RTDF2007-46013.

9. 2019-2020 MWL-Associated Open Safety Recommendations. (2020).

10 . Tank-car Specifications & Terms. (n.d.). Retrieved from https://www.bts.gov/surveys/annual-tank-car-facility-survey/tank-car-specifications-terms

11. L.J. Gibson, M. Ashby, Cellular Solids, Structures and Properties, second ed., Cambridge University Press, Cambridge, England, 1997 https://doi.org/10.1017/CBO9781139878326.

12. A.G. Evans, J.W. Hutchinson, M. Ashby, Multifunctionality of cellular metal systems, Prog. Mater. Sci. 43 (1998) 171–221, https://doi.org/10.1016/S0079- 6425(98)00004-8.

---

13. J. Marx, A. Rabiei, Overview of composite metal foams and their properties and performance, Adv. Eng. Mater. 19 (2017), https://doi.org/10.1002/ adem.201600776.

14. B. Neville, A. Rabiei, Composite metal foams processed through powder metallurgy, Mater. Des. 29 (2008) 388–396, https://doi.org/10.1016/j. matdes.2007.01.026.

15. A. Rabiei, L. Vendra, A comparison of composite metal foam's properties and other comparable metal foams, Mater. Lett. 63 (2009) 533–536, https://doi.org/ 10.1016/j.matlet.2008.11.002.

16 . A. Rabiei, Composite Metal Foam and Methods of Preparation Thereof. US20100158741 A1 2009, issued 2010.

17. A. Rabiei, Composite Metal Foam and Methods of Preparation Thereof. US9208912 B2, 2012, issued 2015.

18. A. Rabiei, L. Vendra, N. Reese, N. Young, B. Neville, Processing and characterization of a new composite metal foam, Mater. Trans. 47 (2006) 2148–2153, https://doi.org/10.2320/matertrans.47.2148.

19. L. Vendra, A. Rabiei, Evaluation of modulus of elasticity of composite metal foams by experimental and numerical techniques, Mater. Sci. Eng.: A 527 (2010) 1784–1790, https://doi.org/10.1016/j.msea.2009.11.004.

20. Lakshmi Vendra, Brian Neville, Afsaneh Rabiei, Fatigue in aluminum-steel and steel-steel composite foams, J. Mater. Sci. Eng. 517 (iss. 1–2) (2009) 146–153.

21. M. Garcia-Avila, A. Rabiei, Effect of sphere properties on microstructure and mechanical performance of cast composite metal foams, Metals 5 (2) (2015) 822–835.

22. A. Rabiei, M. Garcia-Avila, Effect of various parameters on properties of composite steel foams under variety of loading rates, Mater. Sci. Eng.: A 564 (2013) 539–547, https://doi.org/10.1016/j.msea.2012.11.108.

23. Y. Alvandi-Tabrizi, D.A. Whisler, H. Kim, A. Rabiei, High strain rate behavior of composite metal foams, Mater. Sci. Eng.: A 631 (2015) 248–257.

24. M. Garcia-Avila, M. Portanova, A. Rabiei, Ballistic performance of composite metal foams, Compos. Struct. 125 (2015) 202–211.

25. J. Marx, M. Portanova, A. Rabiei, A Study on Blast and Fragment Resistance of Composite Metal Foams through Experimental and Modeling Approaches, Composite Structures, 2018, https://doi.org/10.1002/adem.201600776.

26. S. Chen, M. Bourham, A. Rabiei, Attenuation efficiency of X-ray and comparison to gamma ray and neutrons in composite metal foams, Radiat. Phys. Chem. 117 (2015) 12–22.

27. S. Chen, M. Bourham, A. Rabiei, Neutrons attenuation on composite metal foams and hybrid open-cell Al foam, Radiat. Phys. Chem. 109 (2015) 27–39.

28. S. Chen, M. Bourham, A. Rabiei, Novel light-weight materials for shielding gamma ray, Radiat. Phys. Chem. 96 (2014) 27–37.

29. K. Kitazono, A. Kitajima, E. Sato, J. Matsushita, and K. Kuribayashi: *Mater. Sci. Eng. A*, 2002, vol. 327, pp. 128–32.

30. H.N.G. Wadley, N.A. Fleck, and A.G. Evans: *Compos. Sci. Technol.*, 2003, vol. 63, pp. 2331–43.

31. K.P. Jackson, J.M. Allwood, and M. Landert: *J. Mater. Process. Technol.*, 2007, vol. 204, pp. 290–303.

32. A. Nabavi and J.V. Khaki: *J. Sandw. Struct. Mater.*, 2010, vol. 13, pp. 177–87.

33. M.A. Yahaya, D. Ruan, G. Lu, and M.S. Dargusch: *Int. J. Impact Eng.*, 2015, vol. 75, pp. 100–9.

34. H. Lin, H. Luo, W. Huang, X. Zhang, and G. Yao: *J. Mater. Process. Technol.*, 2016, vol. 230, pp. 35–41.

35. Andrews E, Sanders W, Gibson LJ. Compressive and tensile behaviour of aluminum foams. *Mater Sci Eng A*. Epub ahead of print 1999. DOI: 10.1016/S0921-5093(99)00170-7.

36. Motz C, Pippan R. Deformation behaviour of closed-cell aluminium foams in tension. *Acta Mater* 2001; 49: 2463–2470.

37. Olurin OB, Fleck NA, Ashby MF. Deformation and fracture of aluminium foams. *Mater Sci Eng A* 2000; 291: 136–146.

38. Smith BH, Szyniszewski S, Hajjar JF, et al. Characterization of steel foams for structural components. *Metals (Basel)* 2012; 2: 399–410.

39. Szyniszewski ST, Smith BH, Hajjar JF, et al. The mechanical properties and modeling of a sintered hollow sphere steel foam. *Mater Des* 2014; 54: 1083–1094.

40. S. Chen, J. Marx, A. Rabiei, Experimental and computational studies on the thermal behavior and fire retardant properties of composite metal foams, Int. J. Therm. Sci. 106 (2016) 70–79.

41. W. Hsieh, J. Wu, W. Shih, W. Chiu, Experimental investigation of heat-transfer characteristics of aluminum-foam heat sinks, Int. J. Heat Mass Tran. 47 (2004) 5149–5157, https://doi.org/10.1016/j.ijheatmasstransfer.2004.04.037.

42. A. Rabiei, “Materials with Improved Absorption of Collision Forces for Railroad Cars,” 2014.

43. J. K. L. Lai, “A review of precipitation behaviour in AISI type 316 stainless steel,” *Mater. Sci. Eng.*, vol. 61, no. 2, pp. 101–109, Nov. 1983.

44. S. L. Lopatnikov, B. A. Gama, and J. W. Gillespie, “Modeling the progressive collapse behavior of metal foams,” *Int. J. Impact Eng.*, vol. 34, no. 3, pp. 587–595, 2007.

45. L. Li, P. Xue, and G. Luo, “A numerical study on deformation mode and strength enhancement of metal foam under dynamic loading,” *Mater. Des.*, vol. 110, pp. 72–79, 2016.

46. J. Marx, M. Portanova, and A. Rabiei, “Ballistic performance of composite metal foam against large caliber threats,” *Compos. Struct.*, vol. 225, p. 111032, Oct. 2019.

47. Jacob C. Marx, Samuel J. Robbins, Zane A. Grady, Frank L. Palmieri, Christopher J. Wohl, Afsaneh Rabiei, “Polymer Infused Composite Metal Foam and its Performance as an Aircraft Leading Edge”, Applied Surface Science 505 (2020) 144114

48. ASTM E8. ASTM E8/E8M standard test methods for tension testing of metallic materials 1. *Annu B ASTM Stand 4*. Epub ahead of print 2010. DOI: 10.1520/E0008.

49. Motz C, Pippan R. Deformation behaviour of closed-cell aluminium foams in tension. *Acta Mater* 2001; 49: 2463–2470.

50. Andrews E, Sanders W, Gibson LJ. Compressive and tensile behaviour of aluminum foams. *Mater Sci Eng A* 1999; 270: 113–124.

51. Von Hagen H, Bleck W. Compressive, tensile and shear testing of melt-foamed aluminium. In: *Materials Research Society Symposium - Proceedings*. 1998. Epub ahead of print 1998. DOI: 10.1557/proc-521-59.

52. Brown JA, Vendra LJ, Rabiei A. Bending properties of Al-steel and steel-steel composite metal foams. *Metall Mater Trans A Phys Metall Mater Sci* 2010; 41: 2784–2793.

---

53. Rabiei A, O'Neill AT, Neville BP. Processing and development of a new high strength metal foam. In: *Materials Research Society Symposium Proceedings*. 2005. Epub ahead of print 2005. DOI: 10.1557/proc-851-nn11.4.

54. Vendra L, Rabiei A. Evaluation of modulus of elasticity of composite metal foams by experimental and numerical techniques. *Mater Sci Eng A* 2010; 527: 1784–1790.

55. Andersen O, Waag U, Schneider L, et al. Novel metallic hollow sphere structures. *Adv Eng Mater* 2000; 2: 192–195.

56. Falkowska A, Seweryn A. Fatigue of sintered porous materials based on 316l stainless steel under Uniaxial loading. *Mater Sci* 2015; 51: 200–207.

57. Amdt. 179-50, 60 FR 49078, Sept. 21, 1995, as amended by Amdt. 179-50, 61 FR 33256, June 26, 1996; 66 FR 45390-45391, Aug. 28, 2001.

58. T. L. Anderson, B. Rose, P. C. McKeighan, S. W. Kirkpatrick, "Quantifying and Enhancing Puncture Resistance in Railroad Tank-cars Carrying Hazardous Materials", 2007.

59. Jacob Marx, Afsaneh Rabiei, Tensile Properties of Composite Metal Foam and Composite Metal Foam Core Sandwich Panels, Journal of Sandwich Structures and Materials, in review

60. http://asm.matweb.com/search/SpecificMaterial.asp?bassnum=MQ316A

61. A. Rabiei, K. Karimpour, D, Basu and M. Janssens, "Steel-Steel Composite Metal Foam in Simulated Pool Fire Testing," *International Journal of Thermal Sciences*, 2019, under review.

62. K. McGrattan, S. Hostikka, R. McDermott, J. Floyd, M. Vanella, Fire dynamics simulator user's guide, in: sixth ed.National Institute of Standards and Technology, vol. 1019, NIST Special Publication, Gaithersburg, MD, 2018 https://doi.org/10.6028/NIST.SP.1019.

63. G. Forney, Smokeview, A tool for visualizing fire dynamics simulation data, in: sixth ed.National Institute of Standards and Technology, vol. I, NIST Special Publication 1017-1, Gaithersburg, MD, 2018. User's Guide.

64. Combustion Handbook, Volume vol. I (third ed.*)*. Cleveland, OH: North American Manufacturing Co., 2001.

---

65. Heats of combustion and related properties of pure substances, in: *fifth ed.*The SFPE Handbook of Fire Protection Engineering, vol. 30, Springer, New York, NY, 2016, pp. 3440–3447, https://doi.org/10.1007/978-1-4939-2565-0. Table A.

66. K. McGrattan, S. Hostikka, R. McDermott, J. Floyd, M. Vanella, Fire dynamics simulator technical reference guide, in: sixth ed.Validation," National Institute of Standards and Technology, vol. 3, NIST Special Publication, Gaithersburg, MD, 2018 https://doi.org/10.6028/NIST.SP.1018, 1018-3.

67. Yields of fire products and chemical, convective, and radiative heats of combustion for well-ventilated fires, in: *fifth ed.*The SFPE Handbook of Fire Protection Engineering, vol. 39, Springer, New York, NY, 2016, pp. 3466–3471, https://doi.org/10.1007/978-1-4939-2565-0. Table A.

68. C. Beyler, Fire hazard calculations for large, open hydrocarbon fires, in: *fifth ed.*The SFPE Handbook of Fire Protection Engineering, Chapter 66, Springer, New York, NY, 2016, pp. 2591–2663, https://doi.org/10.1007/978-1-4939-2565-0.

69. S. Hostikka, K. McGrattan, A. Hamins, Numerical modeling of pool fires using LES and finite volume method for radiation, in: Seventh International Symposium on Fire Safety Science, Worcester, MA, 2003, pp. 383–394, https://doi.org/10.3801/IAFSS.FSS.7-383.

70. Combustion properties of fuels, in: *fifth ed.*The SFPE Handbook of Fire Protection Engineering, vol. 40, Springer, New York, NY, 2016, pp. 3472–3475, https://doi.org/10.1007/978-1-4939-2565-0. Table A.

71. D. Gross, Data Sources for Parameters Used in Predictive of Fire Growth and Smoke Spread, National Bureau of Standards, Gaithersburg, MD, 1985. NBSIR 85-3223.

72. Thermal Ceramics Products from Morgan Advanced Materials: Product Data Book, Morgan Advanced Material Thermal Ceramics Inc., Augusta, GA, 2016.

73. Eurocode 3, Design of Steel Structures - Part 1-2: General Rules - Structural Fire Design, European Committee for Standardization, Brussels, Belgium, EN, 2005, 1993-1-2.

74. L. Blevins, Behavior of base and aspirated thermocouples in compartment fires, in: 33rd National Heat Transfer Conference, Albuquerque, NM, 1999. Paper HTD99- 280.

75. M. Luo, Effects of radiation on temperature measurement in a fire environment, J. Fire Sci. 15 (1997) 443–461, https://doi.org/10.1177/073490419701500602.

76. K. McGrattan, S. Hostikka, R. McDermott, J. Floyd, M. Vanella, Fire dynamics simulator technical reference guide, in: sixth ed.Mathematical Model, vol. 1, National

Institute of Standards and Technology, Gaithersburg, MD, 2018 https://doi.org/10.6028/NIST.SP.1018. NIST Special Publication 1018-1.

77. Thermophysical property values for gases at standard atmospheric pressure, in: *fifth ed.*The SFPE Handbook of Fire Protection Engineering, vol. 23, Springer, New York, NY, 2016, p. 3426, https://doi.org/10.1007/978-1-4939-2565-0. Table A.

78. T. Paloposki, L. Liedquist, Steel emissivity at high temperatures, in: VTT Technical Research Centre of Finland, Espoo, Finland, Reserach Note 2299, 2005.

79. “Eurocode 1: Actions on Structures - Part 1-2: General Actions – Actions on Structures Exposed to Fire," European Committee for Standardization, Brussels, Belgium, EN 1991-1-2, 2005.

80. “Thermal Ceramics Products from Morgan Advanced Materials: Product Data Book”. Augusta, GA: Morgan Advanced Material Thermal Ceramics Inc., 2016.

81. D. Gross, "Data Sources for Parameters Used in Predictive Modeling of Fire Growth and Smoke Spread," National Bureau of Standards, Gaithersburg, MD, NBSIR 85-3223, 1985.

82. FRA, “49 CFR Part 179 - Specifications for Tank-cars,” *Code Fed. Regul.*, 2020.

83. B. J. McCaffrey and G. Heskestad, “A robust bidirectional low-velocity probe for flame and fire application,” *Combust. Flame*, vol. 26, pp. 125–127, 1976.